Engineering of NV color centers in diamond for their applications in quantum information and magnetometry

Margarita Lesik

N° ENSC -

THESE DE DOCTORAT
DE L'ECOLE NORMALE SUPERIEURE DE CACHAN

Présentée et soutenue publiquement le 3 Mars 2015 par
Margarita LESIK

pour obtenir le grade de
DOCTEUR DE L'ECOLE NORMALE SUPERIEURE DE CACHAN

Domaine :
Science Physique

Sujet de la thèse :

Engineering of NV color centers in diamond for their applications in quantum information and magnetometry

devant le jury composé de :	M. Brahim LOUNIS	Président
	M. Dmitry BUDKER	Rapporteur
	M. Etienne GHEERAERT	Rapporteur
	M. Jan MEIJER	Examinateur
	Mme. Anne DELOBBE	Examinatrice
	M. Vincent JACQUES	Encadrant de thèse
	M. Jean-François ROCH	Directeur de thèse

Laboratoire LAC ENS CACHAN / CNRS / UMR 9188
Bâtiment 505, Université Paris-Sud, campus d'Orsay, ORSAY Cedex (France)

Contents

Introduction

The Nitrogen-Vacancy (NV) color center in diamond is a fascinating system. Once isolated by optical confocal microscopy at the individual level, its photoluminescence is perfectly stable, even at room temperature. It has an electron spin structure which can be detected as an individual quantum system, prepared in a defined quantum state by optical pumping, and then coherently manipulated using the tools of magnetic resonance. This almost unique set of properties have led to a wide panel of applications: realization of efficient and practical single-photon sources [1, 2, 3], quantum optics [4] and quantum cryptography [5], luminescent nanodiamonds for drug delivery in cells [6] and monitoring neuronal activity [7, 8], spin-based qubit for quantum information [9], efficient sensor for the detection of magnetic fields at nanoscale [10, 11, 12]... All these applications put stringent conditions on the basic material, and there is a need to develop techniques which would allow us to engineer NV centers with tailored properties such as their position, their orientation in the crystal, their density... This sets the frame of the thesis.

Summary of the thesis:

The thesis consists of six chapters.

In chapter 1 we describe the main properties of the NV center, and we explain how it can be used as a quantum bit for the quantum information processing and as well as an atom-like device for performing measurements of the magnetic field through the shift of the energy levels due to the Zeeman effect. We will introduce the main schemes for magnetic resonance experiments enabling the coherent manipulation of the NV center electron spin.

Quantum information devices based on NV centers could be realized from an array of magnetically-coupled spins associated to individual NV centers. In order to couple two centers through a direct magnetic dipole interaction the distance between them should be of the order of 10-20 nm, then requiring high-precision positioning technique. This first task led to the collaboration with Orsay Physics (Fuveau, France). In chapter 2 we will describe the possibility to create NV centers using nitrogen implantation realized with Focused Ion Beam (FIB) technology. For this experiment the standard optical confocal setup used to detect single NV centers was improved in order to reach sub-diffraction resolution and then estimate the ion-beam focus.

The following experiments, described in chapter 3, were done in collaboration with the group of Jan Meijer and Sébastien Pezzagna (Ruhr-Universität Bochum, Germany, and now at Universität Leipzig, Germany). A proven technology for engineering NV centers at the nanoscale is to implant nitrogen atoms using a low-energy ion-beam which limits the straggling of the ions when they penetrate inside the diamond. Since the beam has a poor focus, an additional collimating mask is raster scanned on top of the diamond sample. Unfortunately the proximity of the surface has detrimental consequences on the properties of shallow NV centers generated by this technique. In order to recover the properties observed for "deep" NV centers in single-crystal bulk samples, we collaborated with the Diamond group at LSPM laboratory (Villetaneuse, France) of Alix Gicquel, Jocelyn Achard and Alexandre Tallaire. We investigated the improvement brought by the overgrowth of a thin diamond layer on top of the patterns consisting of the implanted NV centers.

A magnetic field sensor based on an ensemble of NV centers provides an enhancement of the sensitivity to the magnetic field due to the added contribution of all individual responses. In chapter 4 we investigated how layers with a high doping of NV centers can be fabricated using plasma-assisted growth of diamond. We will first describe the efficiency of direct nitrogen insertion, where the flow of nitrogen gas in the plasma chamber is modulated while growing the diamond layer. We will then show that the control of the temperature during the deposition of the diamond layer is a more efficient technique for tailoring the profile of nitrogen doping.

In chapter 5 we will describe the creation of grown-in defects with an almost ideal control of their orientation inside the crystal. The orientation analysis will be performed using the orientation-dependent B-field axis projection to the NV center axis, the dependence of the photoluminescence intensity on the laser polarization angle of the excitation laser, and using the signal collection efficiency.

The coherence property of the NV center electron spin is a key parameter which sets a limit to the sensitivity of all applications relying on this quantum system. Since the coherence is limited by the magnetic noise induced by all other spins existing in the diamond, a standard technique is to implement dynamical decoupling protocols which have been developed in the context of nuclear magnetic resonance. In chapter 6 we will describe an alternative approach where the strain in the lattice sets the NV spin in eigenstates which are intrinsically protected from fluctuations of the magnetic field. While being a magnetic sensor, this scheme turns the NV center in a quantum device which becomes sensitive to the fluctuations of the electrical field, with tentative applications in condensed matter, biology, and microelectronics.

CHAPTER 1

The Nitrogen Vacancy defect

In this chapter, we start by introducing the main optical and spin properties of the nitrogen-vacancy (NV) defects in diamond (§1.1). We then discuss potential applications of the NV center in quantum information science (§1.2) and high sensitivity magnetometry (§1.3). We will analyze the main challenges in material science regarding NV defect engineering for further development of these applications.

1.1 The NV center in diamond

The crystalline structure of the diamond consists of spatially organized carbon atoms bonded with strong covalent bonds. Due to these bonds diamond has specific properties as hardness, electrical non-conductivity and large refractive index [13], leading to a wide range of applications in industry, medicine, and science. Apart from carbon, the diamond lattice can host atomic impurities such as nitrogen, boron, silicon, hydrogen and many others, which change the properties of diamond [13, 14]. For instance while a pure diamond is a perfect insulator [15], boron integration in the diamond lattice modifies the electronic band structure, and makes it a solid semiconductor of p-type [16].

Nitrogen is the most abundant gas in the atmosphere, and it is the most common impurity found in diamond [17]. It can be embedded in the diamond lattice in substitutional position by replacing one carbon atom [18], denoted as Ns and usually called the P1 center. This defect, which is not optically active, acts as an electron donor in the crystal, since N possesses 5 electrons, i.e. one supplementary electron compared to carbon [19]. If a N impurity is associated to a vacancy in a neighboring lattice site, the defect becomes optically active, and is called the nitrogen-vacancy (NV) color center (see Figure 1.1). As soon as a vacancy gets close to Ns [20], three electrons of the nitrogen atom connect with the neighboring carbon atoms through covalent bounds and the remaining electrons form a lone pair.

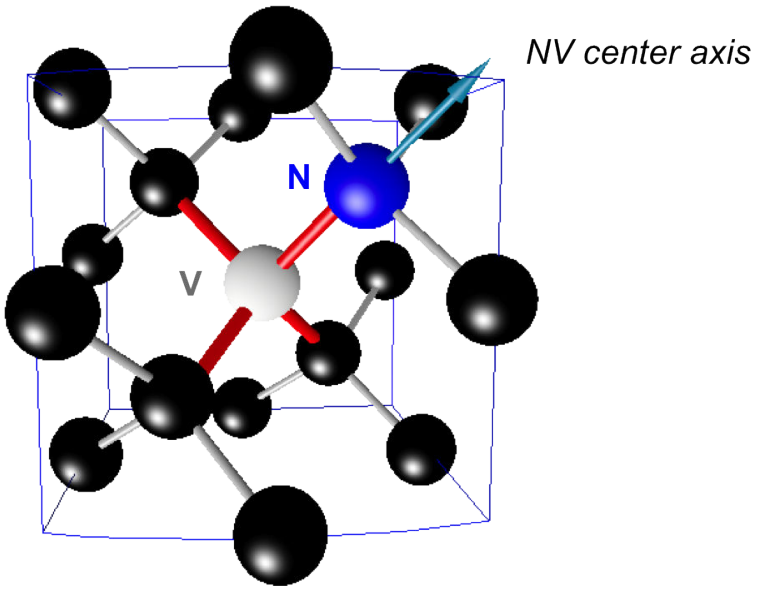

Figure 1.1: NV center atomic structure in diamond (red bonds). Black, blue and white color represent carbon, nitrogen atoms and vacancy respectively.

NV center possesses the C_{3v} symmetry, which implies 120° symmetrical rotation along the N-to-V axis (Figure 1.1), *i.e.* the bond connecting the nitrogen atom and the vacancy. Five unpaired electrons form the neutrally charged NV defect denoted as NV^0. The defect can also trap an additional electron, then becoming the negatively charged center denoted as NV^- [21, 22]. Due to this sixth trapped electron, the NV^- center has an electron spin equal to unity $S = 1$. In the following we briefly introduce the main properties of NV defect in diamond.

1.1.1 Optical properties

In both charge states, the NV defect has an atom-like structure with ground and excited levels (Figure 1.2(a)). It absorbs green light and emits a broadband photoluminescence signal with a zero-phonon-line (ZPL) at 2.156 eV (λ_{ZPL} = 575 nm) for the neutral charged state NV^0 and at 1.945 eV (λ_{ZPL} = 637 nm) for negatively charged NV^- defect [23]. As shown in the Figure 1.2(b), NV^0 and NV^- defects can therefore be discriminated through their PL spectrum [13]. Owing to the high efficiency of the optical transition, NV defect can be easily detected at the single level using optical confocal microscopy under ambient conditions [24]. The experimental setup enabling the detection of NV defect is discussed in appendix A.

It should be noted that PL emission of NV centers is known to be perfectly photostable even at room temperature [24], whereas effects like blinking, or photobleaching are often observed for solid-state emitters like dye molecules [25] or quantum dots [26] under ambient conditions. This perfect photostability enabled the development of highly robust single photon sources operating at room temperature and is currently

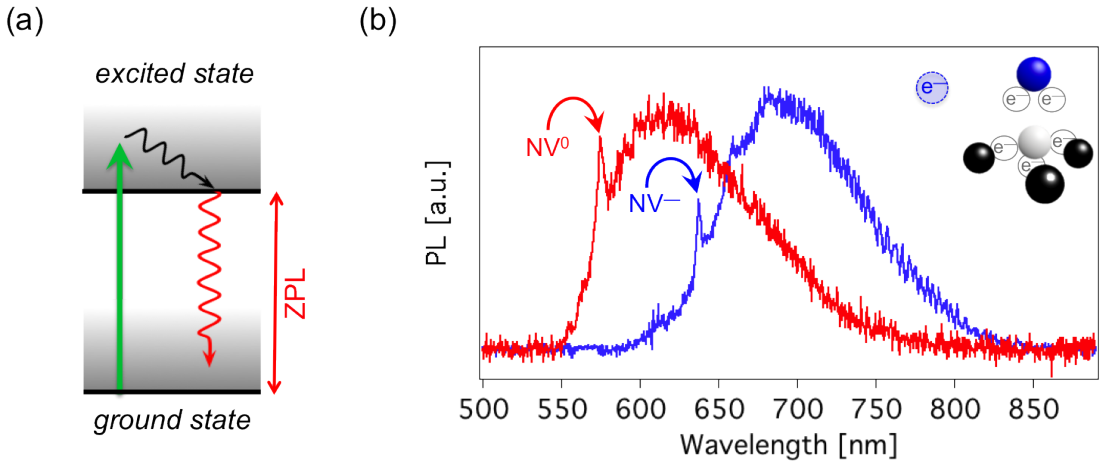

Figure 1.2: (a) NV center's 'atom-like' structure. (b) PL spectra of individual NV defects. The red curve corresponds to the detected PL from NV^0 with only five available electrons denoted with grey solid circles on the inset. The blue curve is the recorded PL of NV^- centers, with an additional trapped electron noted with the dashed blue circle. Both spectra are normalized to their maximum value and the two peaks correspond to the zero-phonon line at 575 nm and 637 nm wavelengths for respectively NV^0 and NV^- charge states.

exploited in biology where NV defects hosted in diamond nanocrystals are used as fluorescent labels [23, 27, 28].

Other applications involving spin properties of NV defect are only based on the use of the negatively-charged form of NV defects, whose spin-properties are discussed in the next §1.2.2. Note that a special attention of researchers is focused on the studies devoted to NV center charge state conversion, which will be partially described in §1.2.3.2 of the present Chapter and experimental results presented in chapter 3. In the following discussion, we will focus mostly on the negatively charged NV centers.

1.1.2 Spin properties

The negatively charged NV center has a $S = 1$ electron spin [29]. Its electronic energy level structure, due to the spin-spin interaction between the unpaired electrons [30, 31], consists of a ground spin triplet with a zero-field splitting D = 2.87 GHz between the singlet state of spin projection $m_s = 0$ of lowest energy and the degenerate doublet states $m_s = \pm 1$ (see Figure 1.3(a)). It should be noted that m_s is denoting the spin projection along the NV center quantization axis, which corresponds to the connecting bond of the nitrogen atom and a vacancy. The fine structure of the ground state can vary depending on the matrix, for instance, the temperature of the crystal [32] or intrinsic parameters like the strain in the lattice [33]. The influence of these parameters on the spin properties will be discussed in more details in chapter 6.

In thermal equilibrium the spin states of the ground level are almost equally pop-

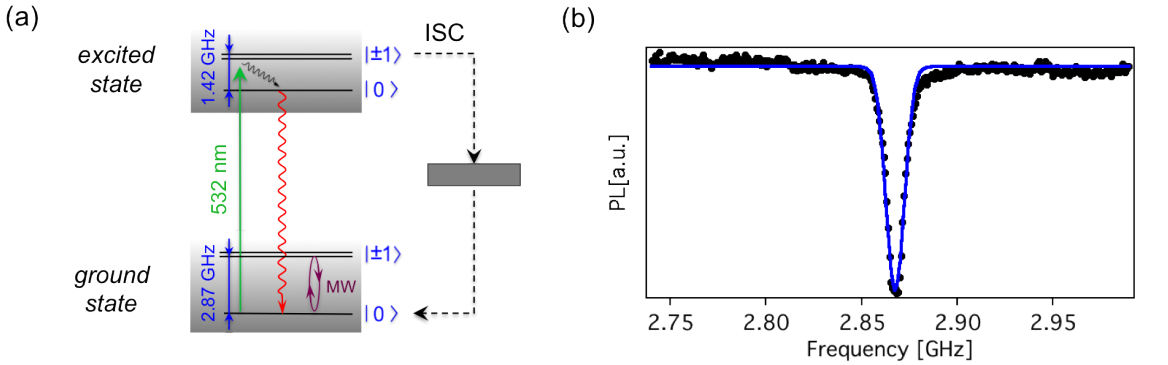

Figure 1.3: (a) Energy level scheme of the fine structure of the NV^- center. It can be excited by a green laser, activating the spin conserving transitions from the ground to excited states (solid lines) and spin-selective inter-system crossing (ISC) transitions leading to spin-rotation (dashed line). (b) Optically detected magnetic resonance of the single NV center in the absence of external magnetic field. The spectra is recorded by detecting the PL intensity level of a single NV center, while sweeping the microwave frequency field.

ulated according to Boltzmann distribution. The NV defect can be optically excited through a spin conserving transitions $\triangle m_s = 0$ to an excited level, which is also a spin triplet with a zero-field splitting $D_{es} = 1.42$ GHz and the same quantization axis and gyromagnetic ratio as in the ground level [34, 35]. Once optically excited, the NV defect can relax either through the same radiative transition producing a broadband red PL, or through a secondary path involving non radiative intersystem crossing (ISC) to a singlet state. This singlet state plays a crucial role in the NV defect spin dynamics. Indeed, while optical transitions are mainly spin conserving ($\triangle m_s = 0$), non-radiative ISCs to the singlet state are strongly spin selective as the shelving rate from the $m_s = 0$ sublevel is much smaller than those from $m_s = \pm 1$ [36] (Figure 1.3(a)). Conversely, the NV defect decays preferentially from the singlet state towards the ground state $m_s = 0$ sublevel. These spin-selective processes provide a high degree of electron spin polarization into $m_s = 0$ through optical pumping [36].

Furthermore, since ISCs are non radiative, the NV defect PL intensity is significantly higher when the $m_s = 0$ state is populated. Such a spin-dependent PL response enables the detection of electron spin resonance (ESR) on a single defect by optical means [24]. Indeed, when a single NV defect, initially prepared in the $m_s = 0$ state through optical pumping, is driven to the $m_s = \pm 1$ spin state by applying a resonant microwave field, a drop in the PL signal is observed, as depicted in Figure 1.3(b) (more details can be found in appendix A). Due to the very high sensitivity of the optical detection, this detection scheme of the electron spin magnetic resonance can be applied in ensembles of NV centers [37, 38] but at the level of an individual quantum system [12, 39].

1.1.3 Coherent manipulation of the NV defect spin state

The possibility to polarize the electron spin of the NV^- center in the $m_s = 0$ state and to discriminate between the $m_s = 0$ and the $m_s = \pm 1$ states by recording the PL intensity allows us to implement, at the level of an individual quantum system, all the techniques which have been developed for spin-state coherent manipulation, in the context of magnetic resonance spectroscopy [40]. In this Section we will describe the scheme used to implement a key measurements of magnetic resonance for a single NV defect : the Rabi oscillation.

By applying a static magnetic field along the NV axis, the degeneracy between $m_S = +1$ and $m_s = -1$ will be removed by the Zeeman effect. Then the corresponding transitions $m_s = 0 \Leftrightarrow m_s = -1$ and $m_s = 0 \Leftrightarrow m_s = +1$ can be addressed independently by tuning the frequency of the driving micro-wave field (see Figure 1.4 (a)). The system then become equivalent to a two-level system, *i.e.* a qubit [41], where the electron spin can be considered either in the 'up-state' $|0\rangle$ or in the 'down-state' $|1\rangle$. A microwave pulse of appropriate duration will then prepare the two-level system in any coherent superposition of $|0\rangle$ and $|1\rangle$.

The pulse sequence used to observe the Rabi oscillation of a single NV defect is shown on Figure 1.4 (b). A first laser pulse is applied in order to prepare the spin in the $m_s = 0$ state ($|0\rangle$) by optical pumping and then followed by a micro-wave pulse. A read-out laser pulse is finally applied in order to measure the relative population in the two states $|0\rangle$ and $|1\rangle$.

Thus the sequence presented on Figure 1.4 (b) is repeated many times while increasing the duration of the MW pulse. Finally the Rabi oscillation measured on a single NV center is shown in Figure 1.4 (c), where the detected PL is oscillating between states $|0\rangle$ and $|1\rangle$ depending on the duration of the MW pulse. From this Rabi measurement, the usual π and $\pi/2$ pulse's durations can be inferred, as represented with the corresponding evolution of the Bloch vector depicting any combination of states $|0\rangle$ and $|1\rangle$ (Figure 1.4 (d)).

1.1.4 Coherent properties of the NV defect electron spin

The dephasing time T_2^* of the NV defect electron spin can be easily measured by adapting the MW pulse sequence which was invented by N.F. Ramsey for the monitoring of spin nutations. This Ramsey technique is presented in Figure 1.5. It consists of two optical pulses used for the initialization in $m_s = 0$ state through optical pumping and read-out of the final state, either $m_s = 0$ or $m_s = \pm 1$, separated by two resonant $\pi/2$ pulses splitted with a free evolution duration time τ. Bloch spheres are used to demonstrate the NV system evolution while the sequence application.

Repeated many times sequence and recorded PL response give the NV center free induction decay signal. The frequency of the oscillations corresponds to the detuning

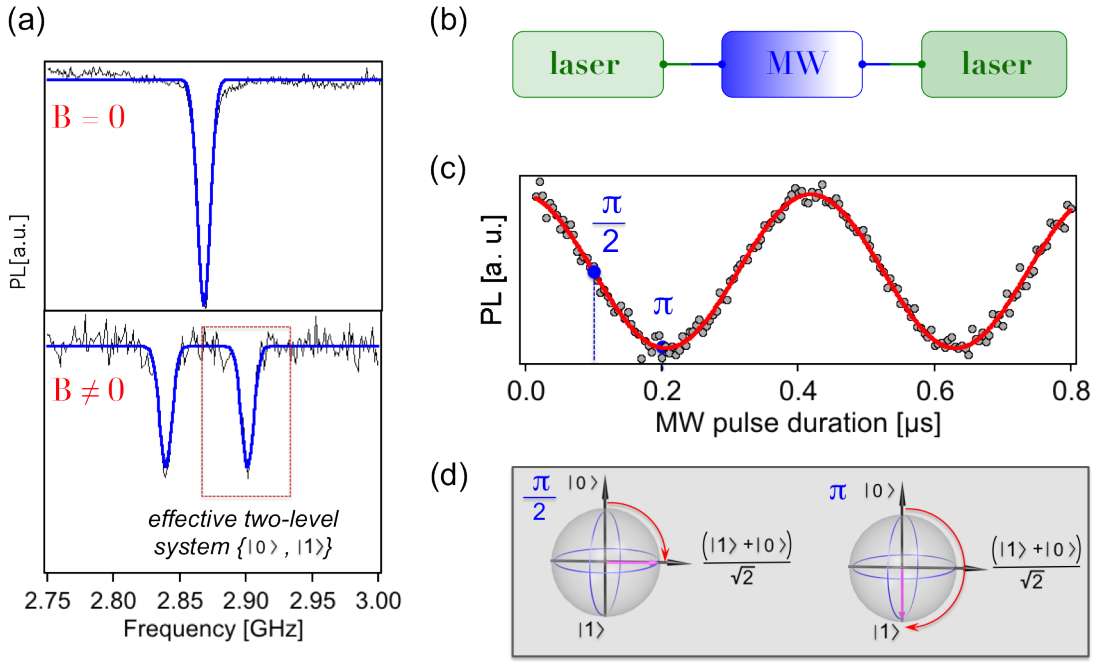

Figure 1.4: (a) ESR spectra of a single NV center electron spin. PL signal of the color defect was recorded as a function of applied MW frequency at magnetic field $B = 0$ and $B \neq 0$. (b) Pulse sequence associated to the (c) measurement of Rabi oscillation observed through the PL intensity emitted by the NV center. (d) A MW π pulse will lead to the spin polarization in the state $|1\rangle$, and a $\pi/2$ pulse can be used in order to polarize the spin in the superposition state $1/\sqrt{2}\,(|1\rangle + |0\rangle)$.

between the MW frequency and the ESR frequency. The envelope of the detected signal decays according to the $1/e^{-(\tau/T_2^*)}$.

The NV defect coherence time is mainly limited by magnetic interactions with a bath of paramagnetic impurities inside the diamond matrix, and on its surface [42]. Paramagnetic impurities in diamond are essentially related to electronic spins bound to nitrogen impurities $S = 1/2$ and ^{13}C nuclei ($I = 1/2$) [43]. Reaching long coherence times therefore requires to engineer diamond samples with an extremely low content of impurities, as close as possible to a perfectly spin-free lattice.

For many years, the only diamond crystals available with a low number of impurities were natural ones, found in the Earth's mantle. In the 1950s, the first synthetic diamond crystals were grown using the high-pressure-high-temperature method (HPHT) [44]. However, for such crystals the typical content of paramagnetic impurities, mainly nitrogen atoms, is still on the order of hundreds of ppm (part per million carbon atoms). Placed in such an electron spin bath, the NV defect coherence time is as short as $T_2^* \sim 100$ ns. During the past few decades, the development of diamond growth using chemical vapor deposition (CVD) processes has allowed a much better control of impurities, thus opening new opportunities for diamond engineering [9]. In particular it has become possible to reduce the nitrogen content in single-crystal CVD-grown diamond from a few ppm down to below one ppb (part per billion carbon atoms) [45]. In such samples, the electron spin bath can be safely neglected and the decoherence of the

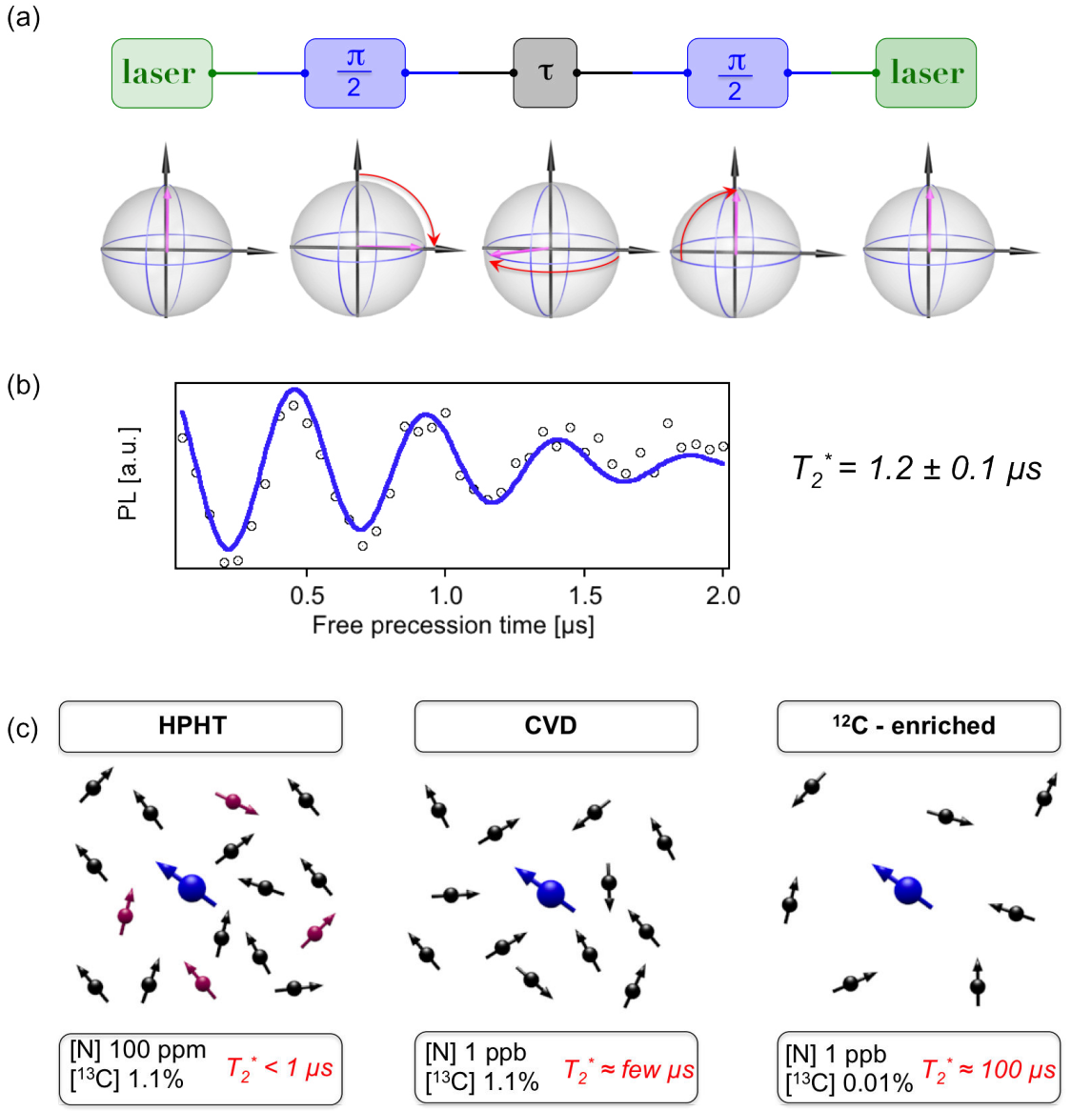

Figure 1.5: (a) The pulse sequence for the Ramsey signal measurements and schematic representation of the NV center system evolution while applying it. (b) A typical Ramsey sequence measurement performed on a single NV defect hosted in CVD ultrapure diamond sample. (c) Schematic representation of the grown diamond samples and their major characteristics related to the NV center spin decoherence.

NV defect electron spin is dominated by the coupling with a bath of ^{13}C nuclear spins (1.1% natural abundance), leading to $T_2^* \sim$ few μs. A typical free induction decay for a single NV defect in this type of sample is shown in Figure 1.5 (b). In addition, it was recently shown that diamond crystals can be isotopically purified with ^{12}C atoms (spinless) during sample growth, thus reducing the content of ^{13}C below 0.01%. Being nestled in such a spin free lattice, the NV defect electron spin coherence time are typically on the order of $T_2^* \sim 100\ \mu$s [46, 47], which is the longest values ever observed for a solid-state system at room temperature. The sample-dependent coherence times of single NV defects under ambient conditions are summarized in Figure 1.5 (c).

In order to improve coherence properties of NV centers, several approaches based

on dynamical decoupling method allowing to protect NV center spin and enhance spin coherence characteristics can be used [48, 49]. Thus the coherence time of NV defects can be further extended using spin-echo sequences which eliminate the slowly fluctuating components of the spin bath (Figure 1.6 (a)). The coherence time achieved using this spin echo technique is commonly denoted T_2. In high purity single-crystal CVD-grown diamond, the T_2 time is on the order of 300 µs (see Figure 1.6 (b)) and reach few ms in isotopically purified diamond sample [46].

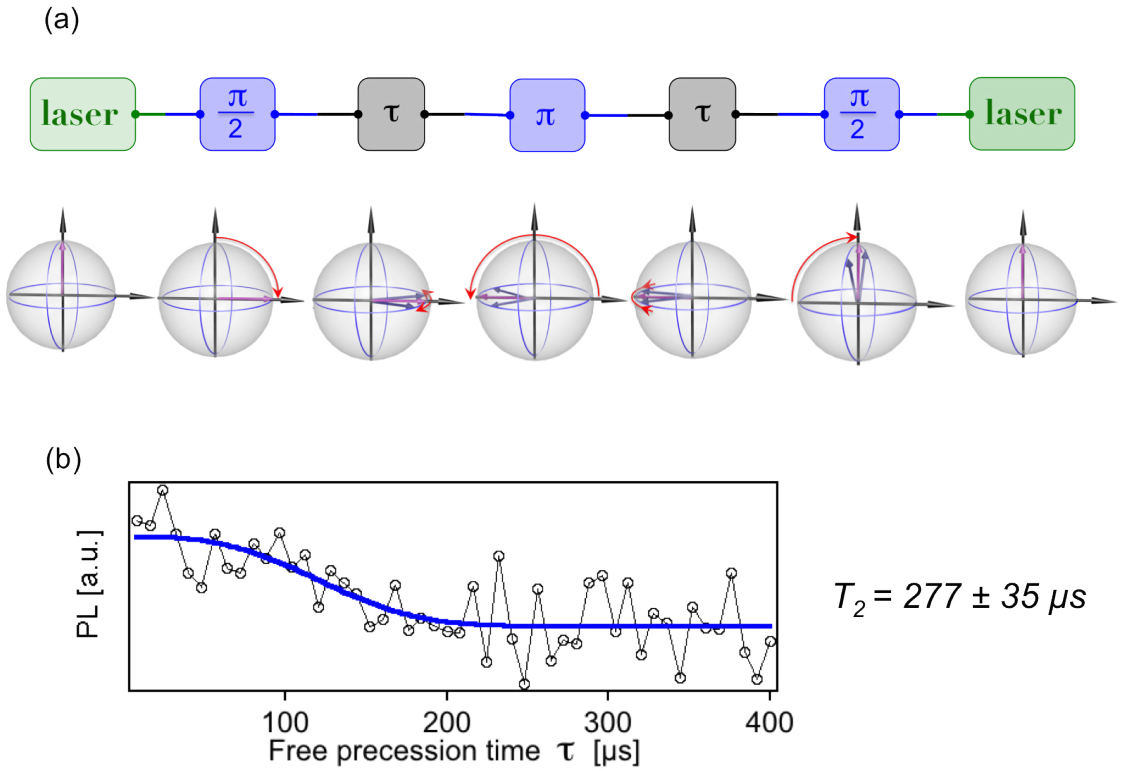

Figure 1.6: (a) Hahn echo pulse sequence representation. Upper scheme is demonstrating the real sequence used for the NV center excitation and lower graphs showing the system evolution under the Hahn echo sequence excitation using the Bloch spheres. (b) Typical Hahn-echo measured signal from a single NV center nestled in the lattice site of a diamond.

1.2 Application of the NV defect in the field of quantum information science

In the previous section, we have shown that the NV defect in diamond has a spin triplet ground state, that can be optically initialized, coherently manipulated with microwave fields and read-out by optical means with long coherence time, even under ambient conditions. The results make the NV defect an outstanding candidate for the development of digital processing of quantum information.

1.2.1 Quantum registers with single spin in diamond

In order to realize a basic quantum information protocol, one needs to create multipartite entangled states. Such experiment implies the use of several coupled qubits, which can be coherently manipulated individually. These conditions can be achieved by using the hyperfine interaction between the NV center electron spin and neighboring nuclear spins in the diamond lattice (Figure 1.7(a)). When hyperfine interaction is observed in the electron spin resonance spectrum recorded on a given NV defect, the associated nuclear spin states can be coherently manipulated through pulsed radiofrequency excitation and read-out by mapping their states onto the electron spin of the NV defect [50]. This method was used in the last years for the realization of a nuclear-spin-based quantum registers [51], multipartite entanglement among single spins at room temperature [52][42], and single-shot readout measurements of individual nuclear spin [**?**].

Although promising, the realization of quantum registers described previously is still conditioned by the presence of nearby ^{13}C, which are randomly distributed in the diamond matrix. This prevents the potential scalability of this technique. In addition, we have indicated previously in the § 1.4 that it is important to reduce as much as possible the content of ^{13}C in order to reach long coherence time of the NV defect electron spin.

In order to develop a scalable diamond-based quantum information architecture, one of the key challenge is thus to achieve coherent coupling between distant NV defects. One strategy consists in positioning the NV defects at a distance such that they are directly coupled by magnetic dipolar interaction [**?**].

The spin Hamiltonian describing the magnetic dipole-dipole interaction between two coupled spins S_1 and S_2 is given by the following expression:

$$H_{dip} = \hbar\Omega_{dip} = \frac{\mu_0 g^2 \mu_B^2}{2hr^3}\left[\hat{S}_1 \cdot \hat{S}_2 - 3(\hat{S}_1 \cdot \overrightarrow{e_r})(\hat{S}_2 \cdot \overrightarrow{e_r})\right], \tag{1.1}$$

where μ_0 is the magnetic permeability, μ_B is the Bohr magneton, r is the distance separating two spins and $\overrightarrow{e_r}$ is their connecting unit vector. Such coupling can be detected if it dominates decoherence, i.e. when $\Omega_{dip} > 1/T_2$ [**?**]. For instance, for two NV defects embedded in high purity CVD diamond samples, this condition is fulfilled if the mutual distance is less than 20 nm (Figure 1.7(c)).

New generation of experiments using NV defects in diamond as solid-state qubit will then require to engineer arrays of NV defects with a spatial resolution at the nanoscale. Ion implantation techniques are promising tools to reach this highly challenging goal.

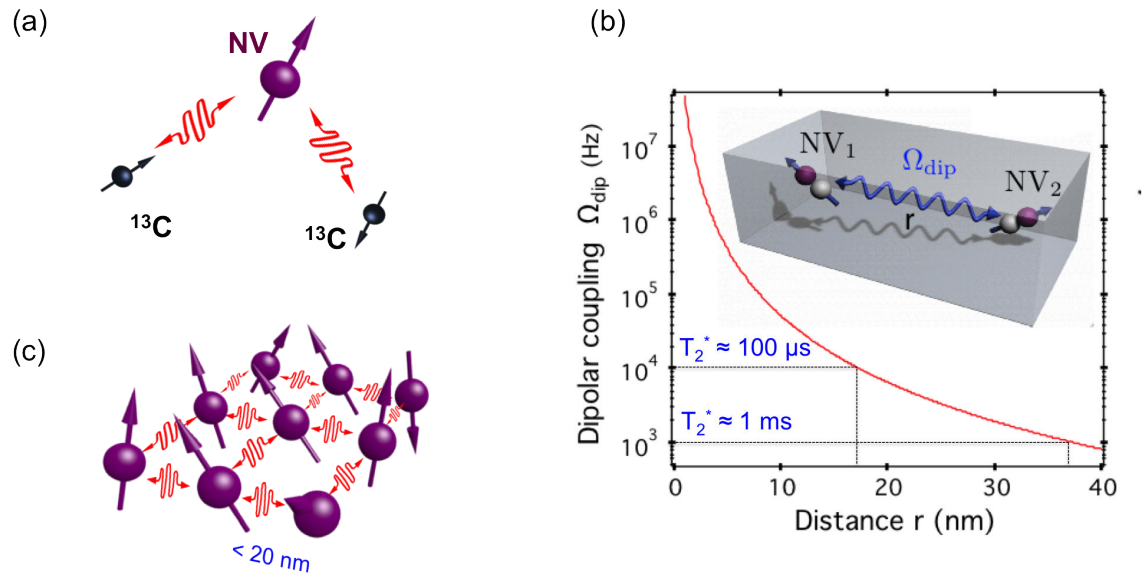

Figure 1.7: (a) Schematic representation of the NV center's interaction with two ^{13}C nuclear spins. (b) Magnetic dipolar interaction between two electronic spin states associated to two NV centers as a function of their separating distance. (c) Network of implanted NV centers, which are separated with less than 20 nm distance in order to realize effective coupling between the neighbouring ones. The distance is associated to the coherence time of the spin.

1.2.2 Engineering NV centers in diamond with ion-implantation technique

Implantation is a process of ions' introduction into a solid state matter lattice by ion-beam exposure at relatively high energies. Usually ion implantation is used to modify properties of a semiconductor material, for instance, formation of p-i-n junction, which is based on donor and acceptor zones creation.

Pioneering implantation with a focused nitrogen beam (Figure 1.8 (a)) of 2 MeV N^+ was realized using a dynamitron tandem accelerator (DTL) in group of J.Meijer at the University of Bochum [53]. Implantation resolution defined by the focal spot of the ion beam, which was tightened with high energy ion-projector, was estimated to be 300 nm. However apart from the ion-beam size, the zone of effective NV centers formation is also defined by the ions distribution in the crystal lattice, due to interactions with the carbon atoms.

Indeed while ion is penetrating in the target material, it experiences a lot of collisions and repulsions (Figure 1.8 (b)), which will lead to the deviation from the initial trajectory and, as a consequence, spread the distribution in the diamond lattice. Such parameter is called *straggling* and it is defined as a square root of the variance of the ion distribution. It depends on several parameters, such as kinetic energy of implanted ions, type of the target material and its orientation respectively to the ion-beam, temperature and so on. Whatever the focusing capabilities of an implantation setup, the spatial resolution is always limited by the intrinsic ion straggling.

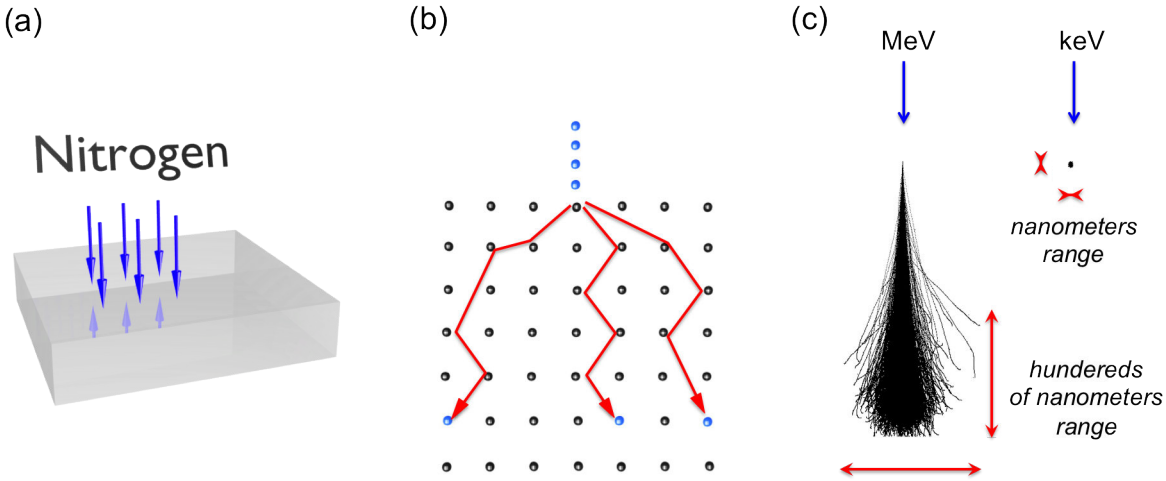

Figure 1.8: (a) Schematic representation of the nitrogen implantation experiment. (b) Ions straggling due to collisions and repulsions. (b) Example of the nitrogen ions penetrating tracks in the diamond sample using SRIM simulation.

For instance, according to Stopping Range of Ions in Matter (SRIM) simulation, implantation of N^+ ions with kinetic energy at 2 MeV is characterized by a penetration depth of 1 mm and a lateral uncertainty of the final stop of $\pm$ 70 nm. However at implantation energies in the keV range, the simulation of ion distribution in the diamond sample gives an evidence of better ion positioning. Due to decreased ion straggling parameter the ion placement precision reaches the range of a several nm instead of hundreds of nm in the case of MeV energies, as can be seen in Figure 1.8 (c).

Another parameter that may influence the final ion stop position is the presence of *channeling* effect (Figure 1.9 (a)). It appears if the ion velocity vector and atomic columns of the target crystals are parallel. After an implanted ion entered in the crystal lattice, it experiences some glancing collisions with very little energy losses, in this case the stopping power is mostly defined by electronic collisions. Usually the ions penetrating along the atomic crystal column are characterized with the higher depth of implantation. There are different methods how to avoid channeling effect. First, by preliminary irradiation a layer of amorphous material can be created on the surface of the sample or another possibility is an introduced tilt of the sample with the respect to the ion beam (Figure 1.9(b)-(c)).

To summarize, ***an improvement of the ion-positioning resolution requires low ion-energy implantation*** to minimize the straggling parameter. Moreover all the samples should be implanted ***with the incident angle of the sample*** in order to avoid ion channeling. The necessity to use low energy implantation forces one to face its inevitable consequences, which will be discussed in the following *Section*s.

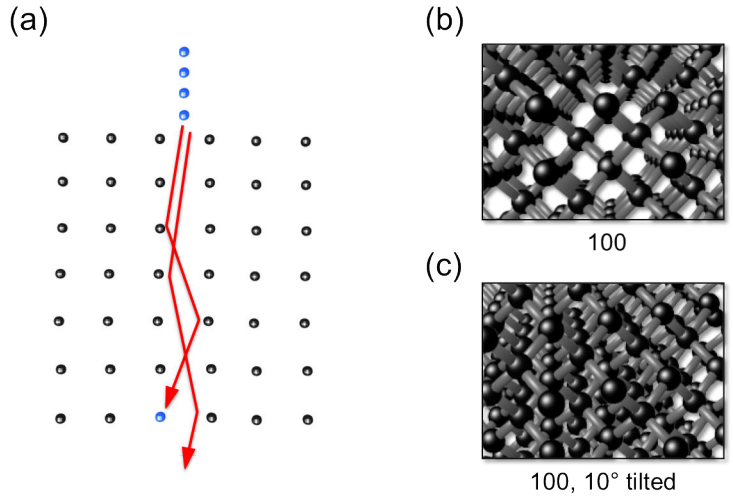

Figure 1.9: (a) Schematic representation of the channeled ions traveling through the column of the carbon atoms of the diamond lattice. (b) Schematic representation of the (100) crystal orientation (top view), where can be seen atomic columns. Each black ball can represent such atoms as carbon, silicon or germanine

1.2.3 Challenges for low energy NV center implantation

Precise positioning control requires the use of low-energy implantation in order to reduce ion straggling to a few nanometers. However implantation at low energy produces NV defect close to the diamond surface, which can dramatically affect the NV defect spin properties [25, 54, 55].

1.2.3.1 Implantation yield

First of all, surface may influence the number of fabricated NV centers respectively to the number of implanted nitrogen-ions (called creation yield). In general, it is $< 1\%$ for the energies of implantation below 10 keV (it might reach nearly 50% in the case of MeV implantation). This fact is mainly related to the number of created vacancies, since implanted ions experience less collisions until their final stop. Indeed estimated using SRIM simulation number of the vacancies created per each implanted ion correlates with the conversion yield of the nitrogen ions to NV centers, what makes it a limiting factor for the yield.

However it should be noted that at the energies lower than 10 keV, yield drops much faster than number of the created vacancies [56]. What may be explained by surface trapping of the vacancies while, for instance, annealing process. In order to improve the yield after the implantation the sample might be irradiated with the electrons or protons in order to produce more vacancies and then annealed to form optically active centers.

1.2.3.2 Charge state

As it was already pointed out the formation of negatively charged NV defects fabrication requires not only a nitrogen bonded with the vacancy, but as well the association of an addition electron to it [57]. One method to increase the concentration of negatively charged NV centers may be an auxiliary implantation of electron donors in the close proximity of nitrogen-implantation (for instance phosphorous atoms) [16]. Another possibility to create dominating number of negatively charged center is to use as a donor of electron, a second atom of nitrogen:

$$2N + V \rightarrow NV^- + N^+. \tag{1.2}$$

However, proximity of the surface may affect the NV center charge state [25]. Indeed, it was already demonstrated that surface proximity provides higher concentration of neutrally charged NV, than negatively charged [58]. As it was explained by Santori et al. this may happen due to presence of electronic acceptor layer nearby the surface, which is trapping the additional 6th electrons of nitrogen-vacancy centers needed to form NV^-. Indeed, bulk NV centers, which are far from the surface effects are stable and presented mostly in negative charge state. For this reason the charge state of NV centers created at low dose of implantation may be stronger affected by the proximity of the surface, due to limited number of acceptors placed on it than at high dose of implantation.

A thin graphite layer, which may have been produced as a result of diamond surface destruction while implantation or thermal annealing may act as an acceptor layer. In order to get rid of graphite layer and switch created centers to their negative charge state several techniques can be used, for instance, oxidation of the surface - oxygen exposure of the sample at 465 °C [59]. Another possibility of the charge control is acid treatment using, for instance, mixture of acids called 'pirahna' solution (sulfuric acid H_2SO_4 and hydrogen peroxide H_2O_2, 3:1) [57]. Switching of negatively charged NV centers to neutral ones can be realized as well by applying external bias voltages, reverse bias potential application leads to reversible change of NV centre charge state [60].

In the chapter 3 will be described an alternative method of the NV center charge control using the overgrowth of the shallow-implanted samples. The experiments were performed on big ensembles and patterned small arrays of NV centers at different conditions of the CVD growth. The main aim of this experiments was the protection and environment restoration of implanted NV centers.

1.2.3.3 Spatial resolution

One of the crucial parameters of ion implantation technique is its spatial resolution defined by the focal spot of the ion beam 1.10(a). As it was already pointed out the

resolution of the NV center positioning for the efficient coupling should stay below 20 nm, what oblige to minimize the ion-beam spot, as much as possible. It can be reached by several techniques: by implantation through the nanoapertures prepared in PMMA layer (see Figure 1.10(b)) [61], drilled AFM tips (see Figure 1.10(c)) [62], or collimating channels in mica (muscovite) foil (see Figure 1.10(d)) [63].

A large-scale array creation of implanted NV centers can be realized using the method based on implantation of the CN molecules through nano-apertures patterned on a polymer layer deposited on the top of an ultrapure diamond sample [61]. This method enables periodic implantation of nitrogen, however it requires quite complex preparation procedure: a clean diamond surface is covered first with a PMMA layer which is further patterned with electron-beam lithography [64]. In order to get predefined mask with apertures it should be developed and only then the ion-implantation can be done. The authors of [61] have reported 2 μm separated apertures with 80 nm diameter. Reported result is similar to another experiment of limitation of the low-energy beam with aperture, where obtained resolution was about 80 nm at 20 keV energy of implantation [65].

Another technique to improve the precision of the ion placement could be an implementation of additional apertures such as pierced AFM tip or mica foil. It was shown that 5 keV implantation combined with a pierced AFM tip used to collimate and address a nitrogen beam provide high-resolution NV centers placement technique with a precision better than 20 nm [62]. Mica foil is a good candidate as well to be used for the mask implantation, since it can have open channels with the size of few tens of nm and it can be thick enough to collimate passing ions through it.

In the chapter 2 will be demonstrated an alternative method of the large-scale arrays creation of implanted NV defects using a Focused-Ion Beam technique at the low energy of implantation. This technique allows creation of small ensembles of NV centers as a result of bombardment with tightly focused nitrogen-ion beam of diamond surface. The size of the focal spot will be estimated by several means. It will be demonstrated that the FIB column combined with the scanning-electron microscope offers new possibilities for the targeted and maskless creation of NV defects in diamond.

1.2.3.4 Coherence properties

In addition surface proximity worsen spin properties of created NV defects, what is definitely undesirable for such application as QIP. It may happen due to presence of the source of electric field fluctuations. In the article [54] the authors have reported systematical ESR lines broadening for the implanted structures at the depth of less than 2 nm, what is the evidence of the worsening of NVs' coherence time. Although recent publication of Yamamoto at al. devoted to the spin coherence time extension of the implanted NV centers in ^{12}C-enriched diamond layers by high-temperature annealing to reach 2 ms value at room temperature [68].

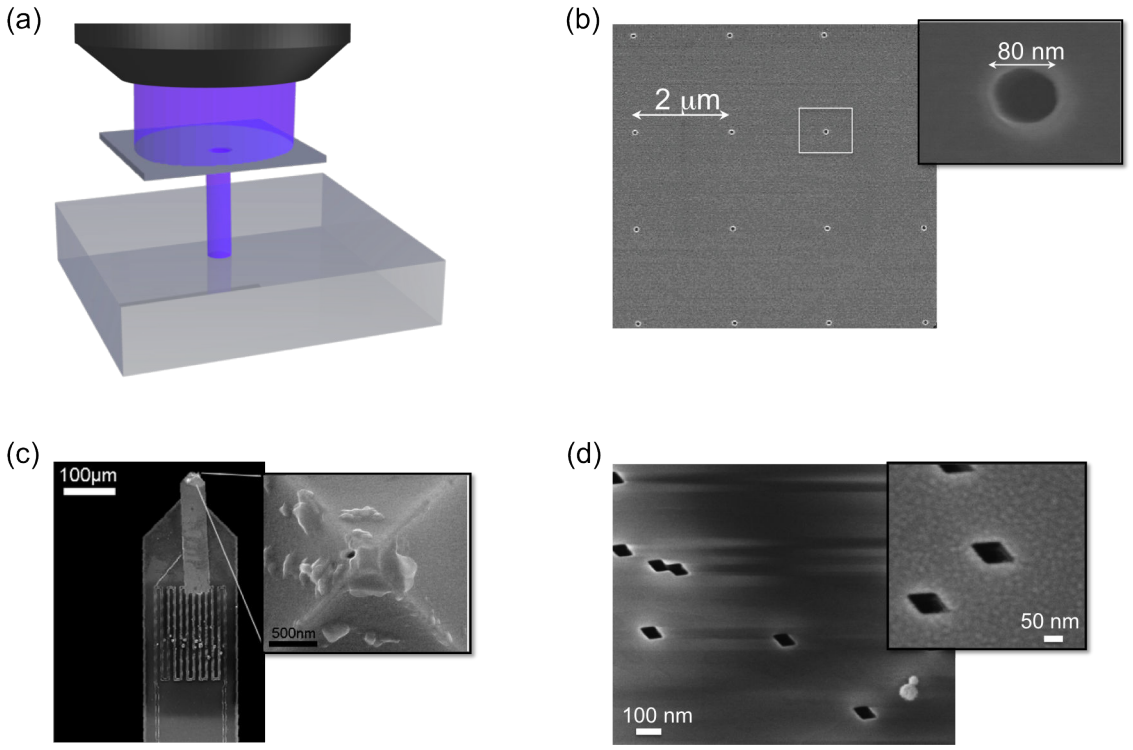

Figure 1.10: (a) Schematic representation of the nitrogen implantation experiments using a mask. (b) Implantation through the drilled holes in PMMA layer covering the diamond surface [61]. (c) Implantation through the collimating AFM tip [66] (b) and channels in mica foil [63, 67](d).

An alternative method of NV defects spin properties protection could be done with an overgrowth experiment. It is based on the principle of burying NV defects placed close to the surface of the sample with another ultrapure CVD layer.

The improvement of the spin-coherence properties using the overgrowth process has been already demonstrated. Indeed the deposition of new CVD diamond layer on top of the shallow implanted NV centers leads to better crystalline environment and consequently to better coherence properties [69], with an improvement by an order of magnitude for the T_2 time and twice longer for T_1 time. Performed implantation was done using an ion beam at relatively low doses of implantation (10^{10} and 10^{13} ions/cm^2) in order to generate ensembles and single NV centers with well-defined position. In our work we are mainly focused on arrays of patterned NV centers in order to record the properties of the same defects before and after the overgrowth (chapter 3).

Recently it was demonstrated that measurements of the coherence time of the NV center at zero magnetic field provide longer T_2^* [70]. In the chapter 5 will be discussed the impact of decoherence processes due to magnetic field and electric field fluctuations and the coherence properties' enhancement.

1.3 NV center application in high sensitivity magnetometry

1.3.1 Magnetometry with NV defect in diamond

The spin properties of NV defects can also be used for magnetic field measurements [37, 71, 72]. In the presence of a static magnetic field, the degeneracy of the NV defect $m_s = \pm 1$ states is lifted by the Zeeman effect. It leads to the appearance of two resonance lines in the electron spin resonance spectrum (Figure 1.11). The frequency of the splitting $\Delta\omega$ between the two resonances is then directly related to the amplitude of the applied magnetic field B_{NV} along the NV defect axis.

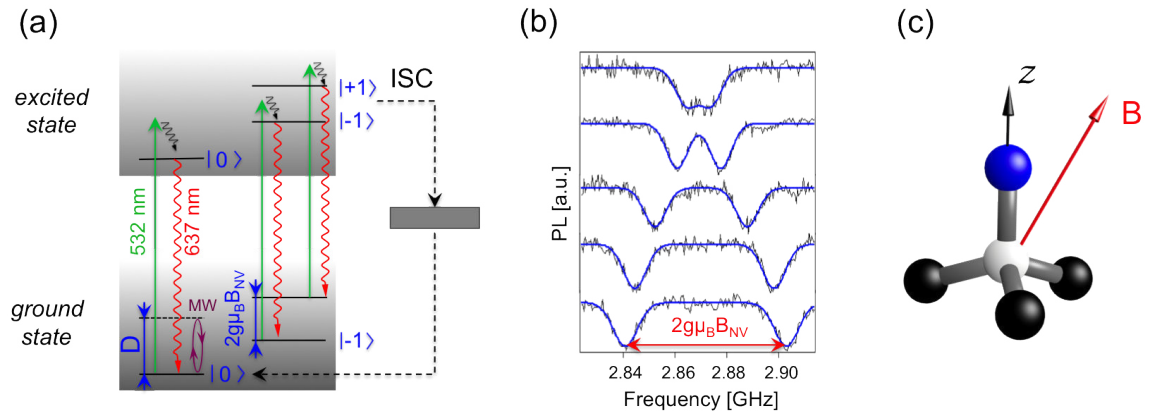

Figure 1.11: (a) Fine structure of the negatively charged NV center in the presence of external static magnetic field. (b) ESR spectra measured at different values of magnetic field. (c) Schematic representation of the NV center. Magnetic field B (red arrow) is applied with a certain angle with respect to the NV defect axis z (black arrow).

The magnetic field sensitivity of a single NV defect is given by

$$\eta = \frac{1}{g\mu_B C\sqrt{T_2^*}}, \tag{1.3}$$

where g is Landé g-factor; μ_B is the Bohr's magneton, C takes into account experimental parameters as the photon collection efficiency and the limited electron spin resonance contrast, T_2^* is the electron spin coherence time [11].

The use of NV centers for magnetometry applications has been discussed in essentially two contexts, either using a single NV center as scanning probe unit [12, 39] or a large ensemble of NV centers [37, 38] for magnetic field sensing and imaging. Both approaches are distinct in spatial resolution and magnetic field sensitivity and find applications in different fields of research ranging from material science, to biology and quantum technologies [73].

The spatial resolution of a single NV scanning probe magnetometer is fundamentally limited by the electron spin wave function, which is in the Angstrom range. In practice,

a single NV defect is integrated onto the tip of an atomic force microscope and used as an atomic-sized magnetic field sensor under ambient conditions.

Extending magnetic field measurements to ensembles of NV centers improves the magnetic field sensitivity by a factor of $1/\sqrt{N}$, where N is the number of NV centers within the optical detection volume. Although this approach provides the highest sensitivity to date, the spatial resolution of magnetic field imaging is then linked to the optical addressing of the ensemble of NV defects and is therefore limited by diffraction (~ 500 nm).

A factor of paramount importance for practical applications in NV magnetometry is the closeness of the sensing NV defects to the diamond surface. It is thus very important to be able to fabricate highly coherent NV defects within few nanometers of a diamond surface to maximally approach the magnetic sensor to the sample under study - a challenging task in material science.

1.3.2 Engineering diamond sample for magnetometry application

1.3.2.1 Creation of thin layers of NV defects by δ-doping

A practical sample for ensemble magnetometry applications would consist of a thin diamond layer containing a large content of NV centers and placed very close to the surface. The nitrogen incorporation can be realized using ion-implantation technique, as described in the previous §1.2.2. Avoiding channeling effect and minimizing straggling parameter could allow to create NV centers with good spatial control [63]. However low-energy implantation is characterized with low conversion yield and large content of NV defects can not be easily achieved. Moreover since it is limited mainly with the number of created vacancies such implantation provides certain number of paramagnetic impurities embedded in the diamond lattice [62]. This fact will decrease the coherence properties of created color centers. Such effect is not desirable, since it has a direct link with magnetic field sensitivity.

Chemical vapor deposition method (CVD) is a flexible technique which can allow producing engineered material. Therefore an alternative method for the NV centers incorporation can be the creation of direct grown-in defects. Diamond material is deposited layer by layer in the growth reactor (see Figure 1.12 (a)) from the gas mixture of methane and hydrogen (Figure 1.12 (b)). Operating at high plasma power density it provides formation of high crystalline quality material (Figure 1.12 (c)). Remarkable that during this process impurities can be selectively and controllably added to the growing diamond chamber by using gases that contain elements such as boron or phosphorous. Moreover formation of NV centers can be realized while diamond growth by straightforward N_2 gas insertion. However such method is limited in the depth control,

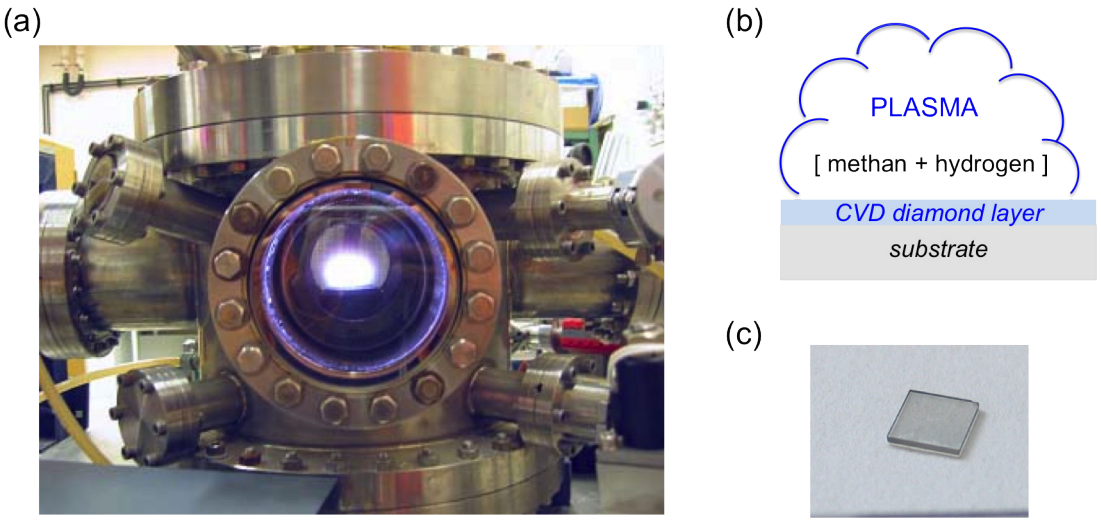

Figure 1.12: (a) Image of a CVD growth reactor used for the deposition of high purity diamond crystal. (b) Schematic representation of the CVD layer deposition process. (c) Image of a standard ultrapure diamond sample.

since even after the full stop of gas insertion in the chamber, already entered ions will continue impacting to the CVD deposition leading to edge smearing between doped and undoped layers.

Recent articles in this field have already shown quite promising results of the experiments, as, for instance, Ishikawa et al., who have reported the possibility of NV centers' doping within 100-nm layer of isotopically purified diamond [47]. Remarkably that coherence properties of such centers is around 1.7 ms, which is much higher in comparison to the coherence times of implanted centers. Kenichi Ohno [74] has realized diamond doping with nitrogen of the 2 nm-thick layer sandwiched in the ^{12}C enriched surroundings. His experiment was realized at very low diamond growth rate 8 nm/h and with a parallel N_2 gas insertion. Such method required additional electron irradiation in order to increase the NV centers' yield. Later on in 2013 Ohashi et al. [75] has published the result of studies of fabricated nitrogen-doped layer in the 5 nm isotopically enriched diamond. Created color centers placed less than 5 nm below the surface are affected by its effects and this can be seen from the reported coherence time values, which could not be dramatically improved by changing the surface termination (best reported $T_2 = 80\ \mu s$).

All the presented above works were based on the low-power microwave densities for diamond deposition (typical parameters are 750 W and 30 mbar) and low methane additions (< 0.5 %). Such parameters provide extremely low growth rate of the diamond substrates. Main drawback of such method is limited nitrogen molecules dissociation and as a consequence of it poor nitrogen incorporation, even at a high flow of N_2 insertion to the growth chamber. Since it was already underlined the sensitivity of the magnetometer device on the base of NV centers defines inversely of square root of number of the used emitters [11]. In the presented above articles NV^- concentration

is in the range of 10^8 - 10^{12} cm^{-3}. In addition low power densities grown substrates may exhibit worse diamond quality especially if the thickness of the grown substrate exceeds 10 µm [76, 77].

The recent progress in diamond growth technique using Plasma Assisted Chemical Vapor Deposition (PACVD) operating at high power providing extremely high purity diamond substrates. Therefore in our experiments devoted to δ - doping experiments demonstrated in chapter 4 this growth technique will be used. The main attention in this chapter will be paid to possibility of the lateral positioning control and efficiency of nitrogen-incorporation. Therefore we will demonstrate an alternative way for the nitrogen incorporation method based on temperature variation.

1.3.2.2 Orientation control

The possibility to use an ensemble of NV centers for the magnetic field sensing device indeed is quite attractive due to enhanced sensitivity. However it should be pointed out that diamond samples have C_{3v} - symmetry, therefore N-V centers' axis can have four possible orientations in the face-centered cubic Bravis lattice of the crystal (Figure 1.13 (a)). Thus it may lead to four possible projections of measured magnetic field on their axis. In order to improve the sensitivity ones will have to select on of four orientations for the magnetic field sensing. In this case the signal will be measured with 25% of centers and all the rest will impact to the detected noise signal affecting the contrast of ESR lines. Therefore the possibility to control NV center' orientation may dramatically improve the magnetic field sensing capacities of NV centers.

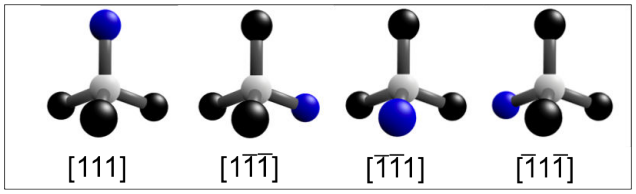

Figure 1.13: Schematic representation of four possible NV centers' orientation.

Despite that ion-implantation can be used as a precise tool for the nitrogen placement, the orientation of the generated NV centers will remain random. Recently it was demonstrated the growth conditions may alternate the ratio of the fabricated NV defects, in particular that while [110]-oriented diamond growth there is a probability of the NV defect formation along two crystal orientations rather than four possible [78],[79].

Indeed, as presented on the Figure 1.14 (100)-oriented plane exhibits all four kinds of orientation and all of them are looking out of the plane parallel to the sample surface, but in the case of [110]-oriented crystal within four orientations two are lying perfectly in the plane. Therefore in case of a [111]-oriented diamond we could then expect to get

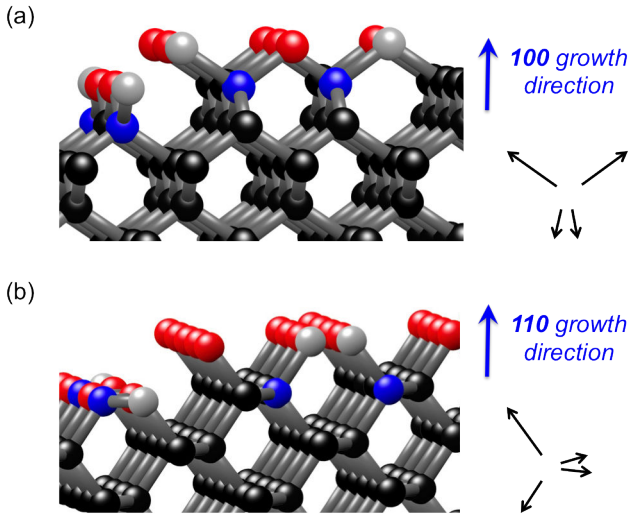

Figure 1.14: Crystal model showing a clean hydrogen saturated (100)-oriented surface (a) and a clean (110)-oriented surface (b). Red, blue, black and white balls are representing hydrogen, nitrogen, carbon atoms and vacancies respectively.

an absolute preferential orientation, since there is just one type of the bond pointing towards the [111] direction of the lattice.

However high-quality (111) - diamond crystals production is a hard to reach aim, mainly it is complicated by its constitutional bias towards the growth in the twinning configuration. It happens if the diamond growth along certain direction will be interrupted or modified due to, for instance, the incorporation of the atom of the different size than carbon. That may cause the roughening of the surface morphology of the sample and affect the electronic properties of the grown diamond substrates. In addition growth in (111) direction is known to be characterized with the higher incorporation efficiency for the impurities. For instance the diamond samples produced using HPHT technique contain such impurities as nitrogen atoms or even some metals. However it still stays an attractive field of studies regarding the possible applications it may be useful for.

In the chapter 5 will be demonstrated the possibility to control the NV centers' orientation depending on the growth conditions of diamond samples deposited on the substrates with different crystal orientations. In order to discriminate the NV centers orientation will be used several techniques: ESR resonance lines shift, PL dependent luminescence of NV centers and the collection efficiency of the emitted light. The possibility to control NV center orientation indeed is an important achievement, since it might be useful not only for the magnetometry but as well for the photonic structures couplings.

Conclusion

In this chapter the main properties of NV center were described. We have demonstrated that NV center possesses unique optical and spin properties allowing to use it in quantum information science and magnetometry. On the base of the state-of-the-art of the diamond-based technology we could define the most challenging developments in material science for NV defect engineering, which became the main objectives of the present work:

1. Formation of big arrays with NV centers implantation with nanoscale spatial resolution (see chapter 2) ;
2. Charge state control of shallow NV centers (see chapter 3);
3. Formation of grown-in NV defects (see chapter 4);
4. NV center orientation control (see chapter 5);
5. Coherence properties improvement (see chapter 6).

In the next chapters will be presented different methods of NV centers engineering in diamond and spin coherence manipulation technique.

CHAPTER 2

Focused Ion Beam implantation

2.1 Introduction

Formation of multiple coupled NV centers requires precise ion-positioning method, which can be realized using additional collimating masks, discussed in §1.2.3.3. An alternative solution could be the a direct implantation of NV centers with highly focused nitrogen-beam. In this chapter we will demonstrate a mask-less creation method of a big network of low energy implanted NV centers using Focused Ion Beam (FIB) technique. We start with a brief introduction to FIB technique (§2.2). We then demonstrate experimental results analyzing the main parameters of ion-implantation as the conversion yield, ion-beam resolution and NV centers distribution within one implantation spot (§2.2).

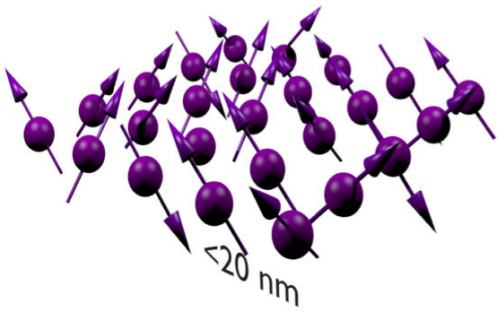

Figure 2.1: Network of implanted NV centers, which are separated with less than 20 nm distance in order to realize effective coupling between the neighboring ones. The distance is associated to the coherence time of the spin.

2.2 FIB technique

FIB technique based on the Liquid Metal Ion Source (LMIS) is known for a long time. The high interest to such systems is caused by wide range of applications, as

for instance, Ga metal source at small energies provide the imaging of the sample and higher energies could be used for the sample milling. However todays demands require the increase of the sputtering rate. Therefore FIB column developed by Orsay Physics S.A. laboratory (see Figure 2.2 (a)) is equipped with a newly developed plasma source based on Electron-Cyclotron Resonance (ESR) type, which allows to reach high beam current also combined with the exchange of the ion species from Ga to Xe providing higher milling velocities. The ESR plasma source is mounted on a customized FIB column to focus and scan the ion-beam on the sample. FIB is installed on a Scanning electron microscope chamber (FERA, Tescan).

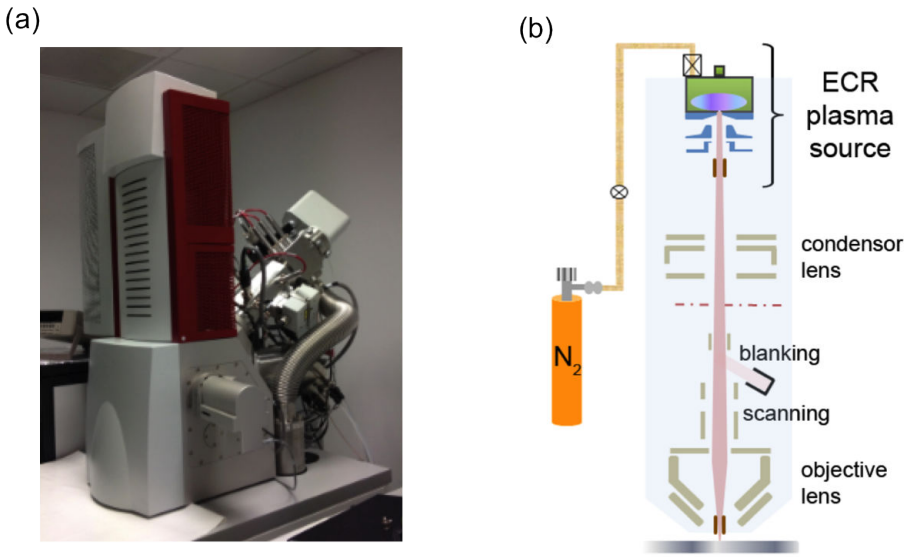

Figure 2.2: (a) Photo of the nitrogen ion focused beam column developed by Orsay Physics S.A. and its (b) scheme based on the an ECR plasma-source, which can produce the beams of the wide range of ions: nitrogen, xenon.

Another advantage of such system is its flexibility to work with the different gas sources. In order to perform Nitrogen-implantation, the gas containing N_2 molecules was injected in the reservoir to get relatively low pressure of the gas in it. The application of static and uniform magnetic field combined with the resonance alternating electric field leads to ionization, the extracted ions are than focused on the sample.

Due to dual-beam configuration (Figure Figure 2.3(a)), where N-beam is combined with the scanning electron beam, a precise control of ion-implantation positioning can be realized. Moreover using the nitrogen ions positioning marks (Figure Figure 2.3(b)) on the surface of the diamond could be created at high ion fluences due to induced amorphization. An example if the SEM microscope image of the sample surface after such high-dose implantation is presented on the Figure 2.3(c). In addition by gas source change from N to Xe, for instance, diamond milling can be done and than followed by N-ion placement.

For these test experiment the FIB was not yet equipped with a Wien mass-separating filter. Therefore the main ion specie was $^{14}N_2^+$, however the beam contains a few per-

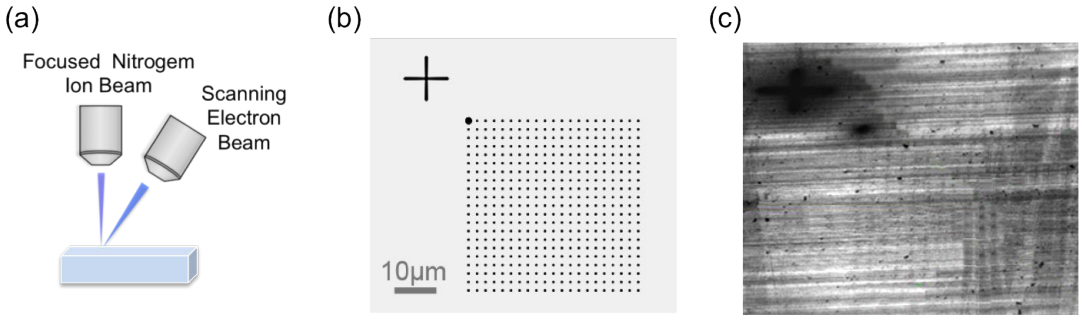

Figure 2.3: (a) Dual beam configuration of the used FIB column; (b) pattern for the Nitrogen implantation, where the cross mark and the point at the upper left-angle will be implanted at the high dose; (c) Scanning electron microscope image of the recorded pattern with the visible cross and first point of the grid.

cent of any other types of the ions. Note that mass separation can be achieved using perpendicular electric and magnetic field sources, which will deflect the ion species depending on their mass.

2.3 Experimental results

The diamond sample used in the experiments was grown on High Pressure High Temperature (HPHT) substrate with (100) orientation. It consists of CVD layer with 200 μm thickness and before implantation the surface of the sample was polished. We used an ultrapure diamond sample in which the initial concentration of N atoms was less than 1 ppb. The fixed parameters were the beam current equals to 0.3 pA and energy 30 keV for N_2^+, what corresponds to 15 keV per atom and according to SRIM leads to a 15 nm implantation depth.

Implantation was realized using the same pattern (presented on the Figure 2.3) with several ion fluxes. For the implantation pattern was chosen a grid consisting of 21×21 points, where each of spots was separated by 2 μm distance from the neighbors. It should be noted that the value of spots spacing in the pattern was chosen in order ensure consequent well-resolved photoluminescence detection of each of them with the confocal microscope system, and further can be minimized. The commencement of the each grid-pattern for the given fluxes was pointed with the cross mark 10×10 μm and a first point at a very high fluence to make them observable with the scanning electron microscope. For all experiments described in this chapter the only tunable parameter was the dwell time per each implanted spot (30 μs, 300 μs and 1 μs) in order to vary the number of implanted ions per unit of the pattern. The anticipated yield of the created NV centers from the number of implanted ions in each spot based on the earlier studies is around 1-5 % [56].

After implantation the sample was annealed during 2 hours at 800 $^\circ$C in the vacuum at 10^{-7} mbar. In order to remove any surface contamination or graphitization, which

will induce the quenching of luminescence, the sample was cleaned in a mixture of boiling acids (1:1:1 sulfuric, percloric and nitric) for 4 hours. Moreover such acid treatment stabilizes the charge state of the NV center created in the surface proximity and restore the diamond structure.

Photoluminescence was performed with the standard confocal set-up described in appendix A. The cross-marks created at high ion fluence is an advantage of the the present experiment, since it can be easily observed with both scanning electron microscope system and confocal one. Despite the slight amorphitization it still exhibit a lot of NV centers to be easily detected at green laser excitation. First sample analysis was done with the confocal set-up, it showed that implanted ions formed a well-detected patterns of created NV centers using 1 ms and 300 μs dwell times and no fabricated color centers was detected for 30 μs dwell time apart of the bright cross mark and first spot. However none of chosen dwell times induced in average a single NV center formation per spot result in the created pattern. For instance a presented pattern on the Figure 2.4, which was created during the highest from used dwell times - 1 ms of the focused ion beam exposure contains a tens of NV defects per spot. As it was pointed out the used ion kinetic energy used in the experiment leads to NV center creation with approximately 20 nm depth below the surface, however performed spectral measurements proved that created luminescent spots are mainly in negatively charge state.

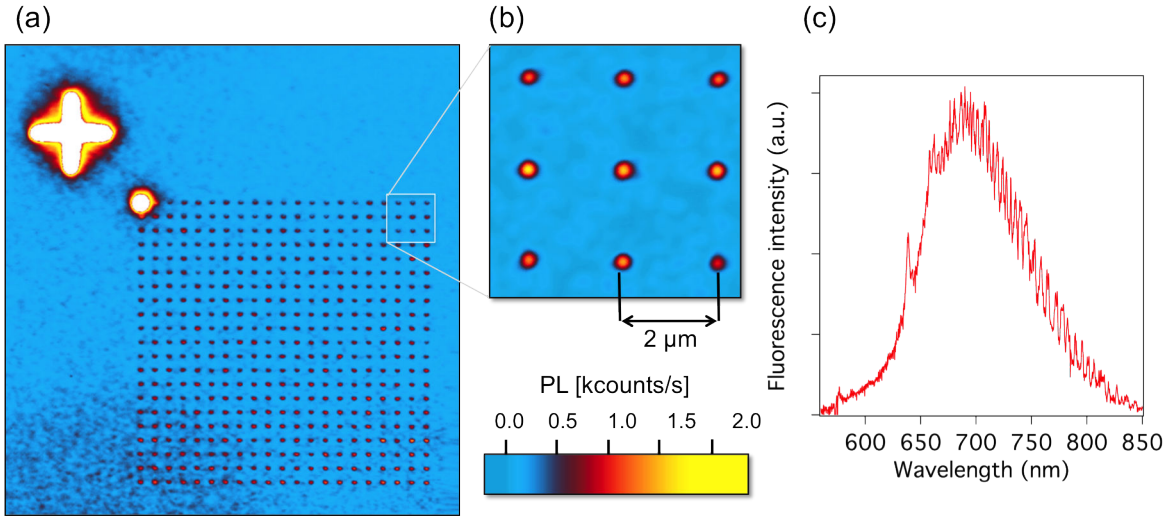

Figure 2.4: (a) and (b) PL image of the one of the fabricated patterns and an inset with 9 of implanted spots respectively, which was implanted with the focused beam of $^{14}N_2^+$ ions and during 1 ms of the dwell time. (c) Represents a typical spectrum of the implanted spots, demonstrating the creation of negatively-charged NV centers.

It can be seen that in the pattern surroundings appeared unwished NV centers with the approximate density of around 1-5 μm^{-2}. This parasitic effect was attributed to the absence of mass-separator mounted on the FIB column. It can be improved by implementing $E \times B$ Wien filter in the later experiments, however the effect of a such

filter on the resolution of the FIB still needs to be studied.

2.3.1 Implantation yield estimation

One of the characteristics of the low-energy implantation is the conversion yield of the implanted number of Nitrogen ions to the number of created NV centers. As it was already pointed out it was anticipated to have around 1-5 % conversion yield. The yield in the case of FIB implantation was estimated through two independent diagnostics.

2.3.1.1 Based on antibunching dip

To ensure that detected luminescence signal is caused by only one photon emission per unit of time [80] we used Hanbury Brown and Twiss interferometer system [81], which is used to get second order correlation function. The principle consists in implementation of the beam splitter $^{50}/_{50}$ to divide the signal in two possible paths and two detectors, which are operated in the photon counting regime, to make the emitted photon to pass either to one or to another detector. It can be described with the equation:

$$g^{(2)}(\tau) = \frac{\langle I(t)I(t+\tau)\rangle}{\langle I(t)\rangle^2} \tag{2.1}$$

This autocorrelation function is used to obtain the histogram of the delay times between two successful events recorded on one detector and followed by the the second one. The measured signal of autocorrelation function corresponds to the probability to detect a photon at a time $(t+\tau)$ with knowledge of its detection at a time (t). Since a NV center is a single-photon source [3] the number of coincidences at zero-delay time is expected to be zero. After the normalization to exclude any background sources [82], the amplitude of the dip in the recorded $g^{(2)}(\tau)$ function indicates the quantity of the emitters. Its value is equal to $^1/_N$, where N is number of luminescent optical centers [1]. On the Figure 2.5 are demonstrated typical antibunching measurements and PL images of single NV center and one of the implanted spots in the pattern produced with 300 μs dwell time.

The shown antibunching dip on Figure 2.5(a) and (b) give an evidence if the implanted spot contains one or more NV centers (if the amplitude of the autocorralation curve is exceeding 0.5 or not, respectively [2]). Similar studies on the 1 ms pattern was impossible to perform due to the too high number of emitters in the spot.

2.3.1.2 Based on the PL intensity

The estimation of the number of NV centers in each implanted spot can be also referred from the measurements of the PL signal intensity. It is known that a NV center

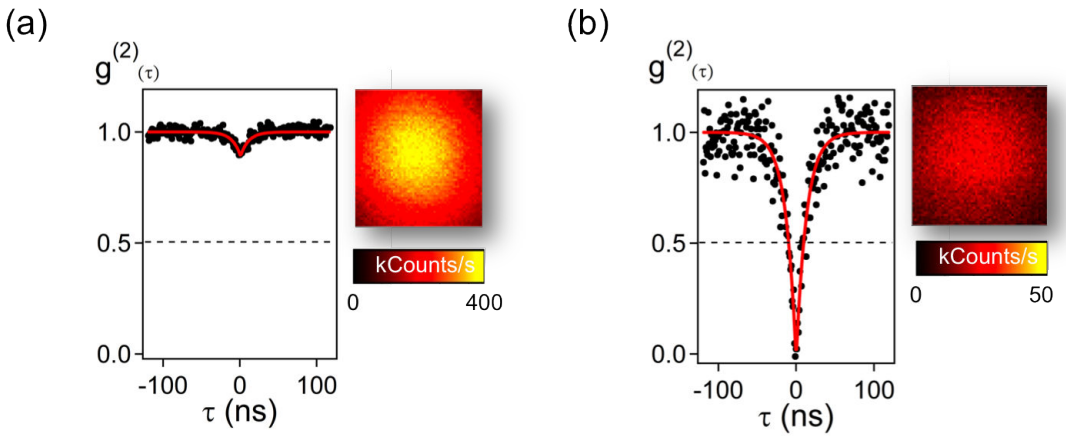

Figure 2.5: Confocal detected PL signal and associated $g^{(2)}(\tau)$ measurement from (a) one of the implanted spots and (b) a single NV.

possesses optical dipole moments, which are lying in the plane perpendicular to the axis of the NV defect [23]. Consequently photoluminescence response depends on the projection of these dipoles on the chosen linearly-polarized laser field [83]. Since diamond possesses C_{3v} symmetry NV centers exhibit 4 possible orientations (see Figure 2.6 (a)), consequently their effective excitation rate depends on their orientation. For all presented orientations, plane containing optical dipoles is placed with the certain angle to the surface, what leads to unequal dipoles excitation and oscillation of emitted PL as a function of polarization angle of excitation light. 100-grown sample contains 2 types of bonds looking out of the diamond surface plane and 2 types, which are looking inside.

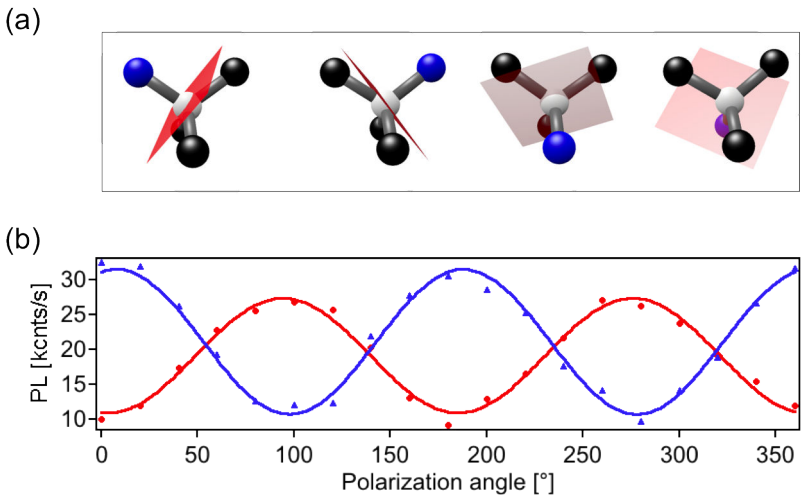

Figure 2.6: Polarization-dependent photoluminescence intensity for single NV defects formed along 4 different crystal orientations. PL signal was recorded well below the saturation, at optical excitation power 15 μW.

Measured PL response as a function of laser polarization angle for the four possible

NV centers' orientation gave presented on Figure 2.6 (b) curves. Note that the power of excitation was taken well below saturation power of NV centers. From this graph it can be seen that it is enough to measure maximal and the minimal signal for one of 4 possibly oriented NV centers, whose mean PL value can be used to estimate the number of emitters in the ensemble for any chosen polarization angle (for more details see appendix B).

Advantage of this technique compared to the previous one is capacity to give an average number of the created NV centers per spot even for the big ensembles. Therefore it was possible to estimate the NV centers yield creation even for the fabricated pattern at 1 ms dwell time. Finally, it was found for 1 ms pattern units of grid contain around 35 centers in each spot and around 8-9 emitters per implanted spot at 300 μs dwell time. Thus the efficiency of the defects formation corresponds to 1% creation yield.

2.3.2 Estimation of the ion-beam resolution

Ion-implantation provide local Nitrogen doping of the diamond samples, however due to the presence of the straggling parameter implantation induces certain distribution of the created centers. The variation of NV defects' location in the diamond lattice causes inhomogenious broadening effect, which results in linewidth raise. Therefore next step is to estimate the focus size of the FIB column. This can be done using again two complementary techniques: firstly by deconvolution of confocal images of several implanted spots and a single NV, and secondly by implementing a sub-diffraction imaging technique, since the confocal sample analysis is diffraction limited technique and it does not allow direct focus measurement.

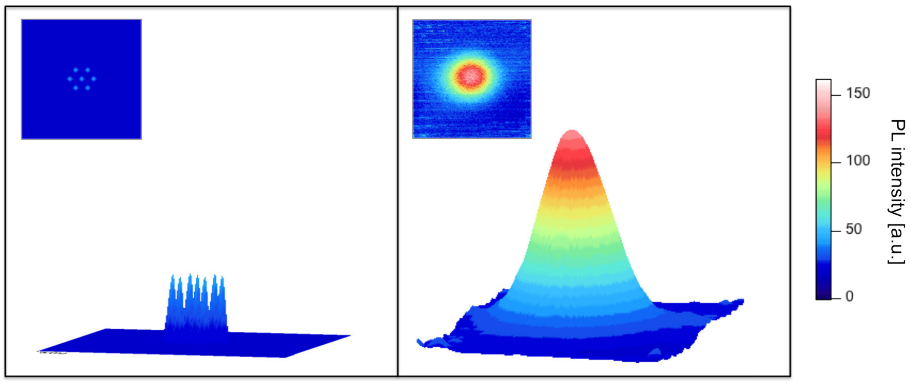

Figure 2.7: Simulated distribution of seven NV centers in the sample surface 100×100 nm and it convolution with the image of the single NV center at the optical excitation power of 70 μW.

As an example can be seen on the Figure 2.7, where on the left inset is presented an simulated image of seven NV centers and on the right their confocal image. The confocal image was simulated using the convolution of the recorded single NV center

and seven randomly distributed point-defects within 100×100 nm zone. It should be noted that used confocal image of single NV center was recorded at optical power excitation below excitation - 70 μW. Considering that the final product of detected defects with the confocal set-up contain the contribution of all them created individually could allow to estimate the size of affected zone with NV defects by performing the inverse procedure.

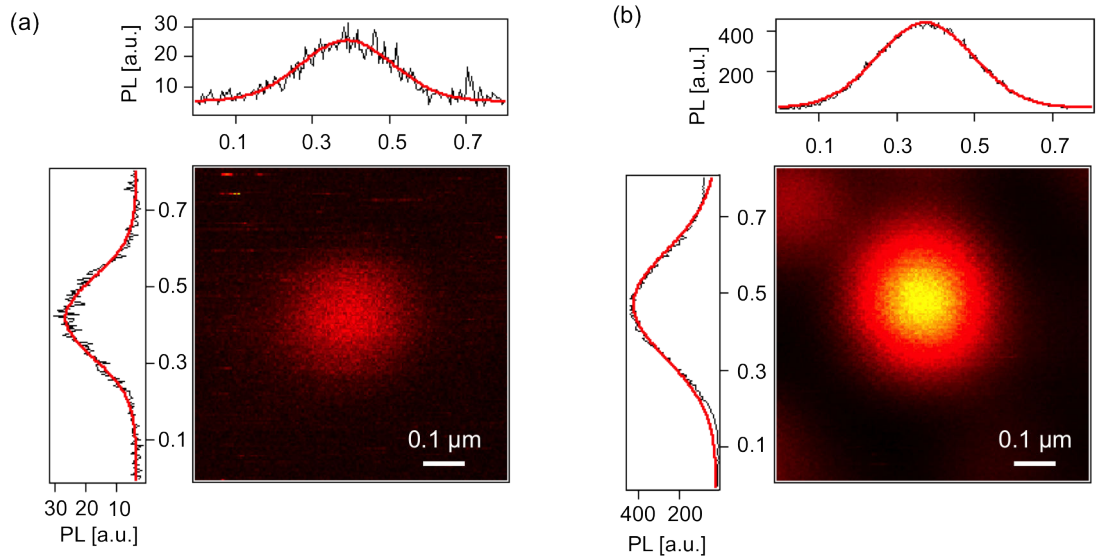

Figure 2.8: Confocal detected PL signal measurement from a single NV defect (a) and one of the implanted spots (b).

The confocal images of the single NV center and one of the implanted spot in the pattern (dwell time 300 μs) are presented on the Figure 2.8. The vertical and horizontal images' profiles were fitted with the gaussian function. The linewidth of the single NV center was found to be around 250 nm, while for the implanted spot it exceeds 300 nm. However PL signal recorded from both structures showed the big difference in the intensity.

The ion-beam resolution determined by the size of the focus of the ion beam was done using deconvolution method. It can be realized by using the confocal images of the single NV center as a point-spread function (PSF) and implanted spots. The analysis of several created structures, which were implanted during 1000 μs per each spot gave an estimation of 100-nm range of implantation. This technique allows to make only a rough estimation of the size of the ion-beam.

2.3.3 Resolving the NV centers within an implanted spot

2.3.3.1 Principle of the GSD technique

One of the most common sub-diffraction imaging technique used for NV center detection is STimulated Emissiom Depletion (STED) Microscopy. It is based on the

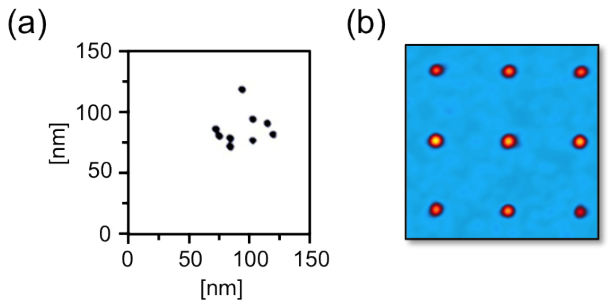

Figure 2.9: (a) Ion beam focus estimation based on the deconvolution method. (b) Used confocal images of implanted ensembles of NV centers and a single NV center.

superposition of two beams, one doughnut shaped for the fluorescence inhibition and green gaussian-shaped for the localized excitation. Whereas the NV centers affected by the ring of red laser they are forced to be in ground state, "switching them off " and excitation is performed only in the unaffected zone - in the center of the doughnut. In order to reach the best achievable resolution should be taken into account the key point: to 'switch off' emitters in as bigger zone as possible. And this requires the necessity to use high power red laser. Another drawback is requirement of fine alignment of the 2 beams superposition. A simpler sub-diffraction imaging technique which can be used as STED is Ground State Depletion (GSD) [84].

The main principle of work is analogous to STED. The function of the red laser in the STED imaging technique is to excite the population of the ground state of the fluorescent molecules to the metastable state and while it is trapped there to perform selective green-laser excitation for the local imaging measurement. The same effect can be realized using green laser as for the consequent excitation [85]. While the population is trapped due to optical shelving, our system find itself in the dark condition, since there is no population in the ground state. If than to apply probe gaussian-shaped laser beam, it can excite only an unaffected zone of pump laser. As a result a sub-diffraction imaging can be realized.

Moreover GSD technique can be realized even simpler just by using a doughnut excitation beam. In this case GSD technique gives kind of negative image, since as a PSF will be used a hole in the center of doughnut. In order to realize it in our experiments, a Gaussian-shaped beam was passed through the vortex plate to convert it to ring shaped profile as demonstrated on the Figure 2.10 and a usual telescope system to magnify the size of the laser spot in order to expose all surface of the plate. Such geometry allows without any significant changes to 'upgrade' a usual confocal setup to a sub-diffraction imaging system.

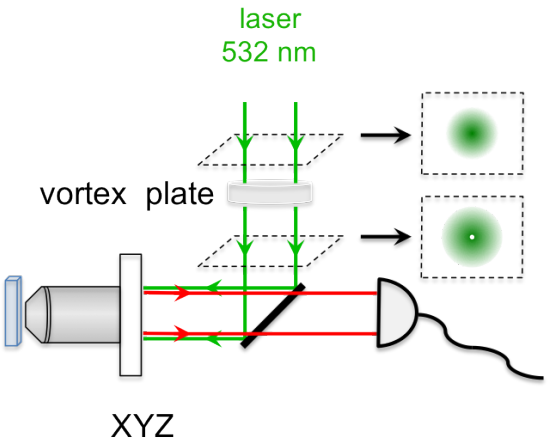

Figure 2.10: Optical scheme for the GSD microscope based on the excitation of the NV center with a doughnut-shaped beam at 532 nm wavelength.

2.3.3.2 Application to a single NV center

The scan of the shallow implanted single NV centers at 135 μW excitation power can demonstrate the example of images (Figure 2.11(a)), which can be obtained using confocal and a doughnut-beam excitation. Than by applying laser intensity much higher than the saturation of the excited level of the emitter, the size of the hole recorded in the centre of the doughnut-shaped image (see Figure 2.11(b)) can be decreased far below the diffraction limit (Figure 2.11(c) and (d)).

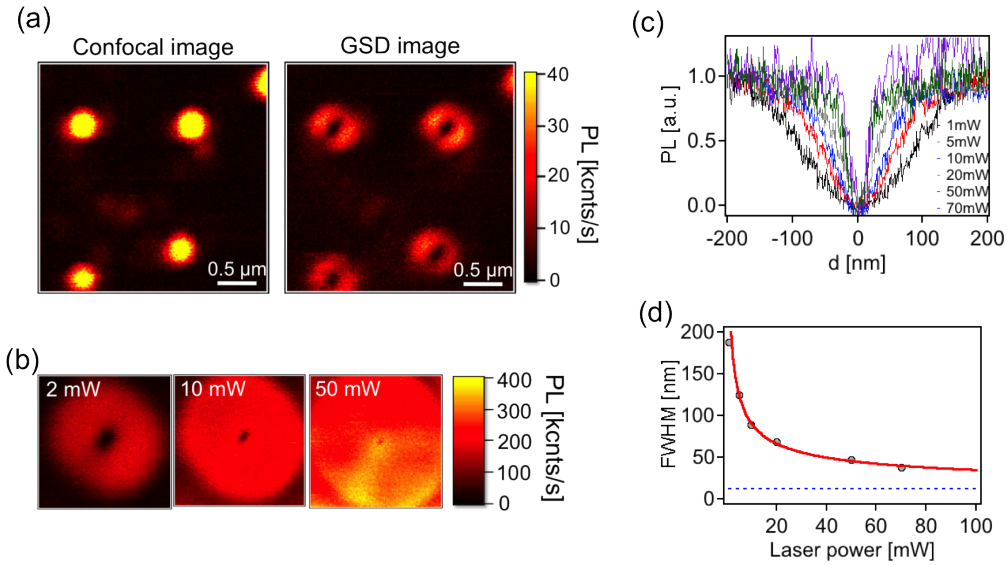

Figure 2.11: (a) Confocal and GSD images of the shallow implanted zone in diamond; (b) single NV center under the doughnut-shaped excitation at different laser power. (c) GSD resolution as a function of optical power for a single NV center. (d) Points are representing measured data and solid line is a theoretical fit, which is proportional to the square root from ratio of radiative decay rate to the excitation rate.

As in the case with STED the imaging resolution defines as the size of the hole inside the doughnut. Keeping the center of the doughnut always unaffected and increasing the

laser pumping intensity improves the resolution according to the following expression [84, 67]:

$$d = \frac{C}{\sqrt{P_{opt}}} + d_{\infty}, \tag{2.2}$$

where d is the resolution (size of the spot), C proportionality coefficient, P is the optical excitation power and d_{∞} is achieved resolution at infinitely high excitation. From the fitting function the best resolution at the infinitely high optical excitation power was found to be 15 nm.

Repeated measurements on the single NV center by varying the laser excitation power gave a curve of GSD resolution improvement. Such negative image can be used to reconstruct the image of the emitters hosted in a given implantation spot, with each of them being associated to a single NV center. The best resolution obtained in this experiment is 37 nm (see Figure 2.11 (c), (d)), but this result still could be improved by applying even higher optical power for the photoluminescence excitation.

2.3.3.3 Application to estimate the FIB focus

The optical power of excitation was set to 50 mW, the image of single NV center gave the resolution around 45 nm. Initially the GSD imaging should have been performed on the pattern created with the dwell time 1ms per spot, in order to compare with the previous focus' estimation technique, but due to too high NVs' density, the GSD analysis was performed on the 300 μs pattern. The GSD image of one of the implanted spots is presented on the Figure 2.12.

The number of NV centers and their relative positions was then estimated, as shown on Figure 2.12. The size of the region in which distributed nine NV centers illustrates the ion beam focus, which was found to be in the range of 100-150 nm. However it should be noted that it is a rough estimation due to the fact that the high surface density of NV centers worsens the obtained result. The two methods used to estimate the resolution of the focused nitrogen ion beam are nevertheless in good agreement. They give an evidence for a beam resolution in the order of 100 nm.

Since the implanted ion specie in the described experiment was ^{14}N isotope, it was important to ensure that created NV centers were formed due to introduced N ions and not as a result of recombination of created vacancy with the native N atom. The sample used in our experiment is an ultrapure diamond with initial concentration of nitrogen $2{\cdot}10^{14}$ cm^{-3}. The lateral size of the ion-beam focus was measured using GSD technique to be in the range of 100 nm and ions' penetration depth was estimated using SRIM simulations to be 20 nm. It allows to calculate the the effective volume of ions distribution and consequently the zone of vacancies formation. Thus the vacancies are efficiently created in the volume $2{\cdot}10^{-16}$ cm^{-3}, therefore we can conclude that per implantation spot there were less than 0.1 native nitrogen. However for the future experiments the FIB column will be equipped with ^{15}N source in order to ensure that

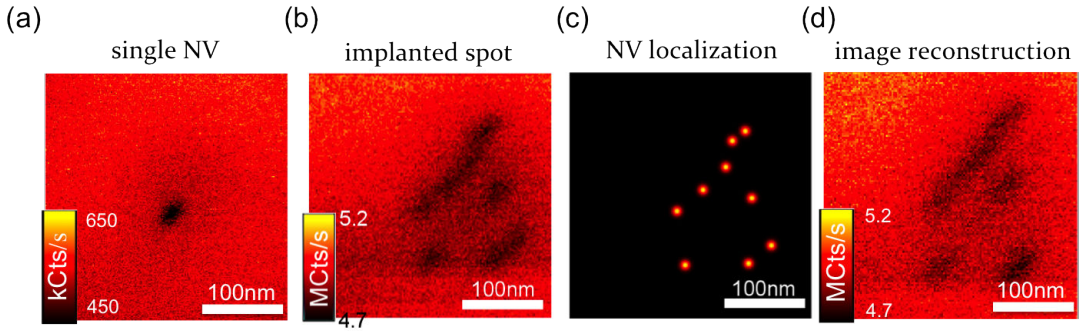

Figure 2.12: Ground State Depletion microscope images of the single NV center (a) and one of the implanted spots (implanted at the fluence of 300 μs dwell time) (b). The laser excitation was set to 50 mW. (c) Deduced positions of created NV centers from the recorded image. (d) Performed image reconstruction, which was obtained by the convolution of the PSF - single NV GSD image and deduced positions of NV centers.

the nature of created NV is inserted, but not a native N. Since ^{15}N natural abundance is 0.37%, it enables easy discrimination if NV center contains native or implanted N [86] by applying electron spin resonance spectroscopy.

Finally, the performed reconstruction of the image let ones to conclude that measurement using the two methods described above showed a good agreement for the size of the FIB focus estimation, which is in the 100-nm range (Figure 2.12). The average number of created NV defects per spot was found to be 9, this can help in further experiments for the implantation procedure optimization in order to get a single centre per spot by using for instance an additional mask such as a mica foil with hollow channels.

2.4 Conclusion and perspectives

A direct maskless formation of large scale arrays of NV centers with focused ion beam technique was demonstrated. The newly developed ECR plasma source combined with scanning electron microscope enables targeted creation of NV centers avoiding complex sample preparation. The size of the focus of the ion beam was estimated by different means to be in the range of 100 nm, both techniques stayed in good agreement.

It should be noted that it is already a good result since that the final size of the focused ion-beam spot is defined by the sum of following parameters:

1. Inhomogenuity of electrostatic field to focus ion beam introduces such effects as spherical aberrations,

2. Certain dispersion in the ion energies may lead to differing focusing distances as a consequence chromatic aberrations can be introduced,

3. Presence of the imperfections of electrodes, or any introduced contaminations may lead to astigmatism, this parameter becoming even more crucial at smaller

incident energies of the ions.

Higher resolution can be achieved by decreasing the number of collisions and repulsions. This can be done by minimizing the energy of implantation. However it should be noted, that the use of lower energies could affect the final focus size. In order to verify it an additional experiments have to be performed.

Future resolution improvement may be reached with collimating mask implementation as a mica foil [63]. Though already obtained rather tight focus opens a new applications for the Focused-ion beam technique - implantation in the predefined structures as diamond tips or in photonics crystals as demonstrated on the Figure 2.13. However it should be noted that even obtained result can be improved by the implementation of a mass filter in the column.

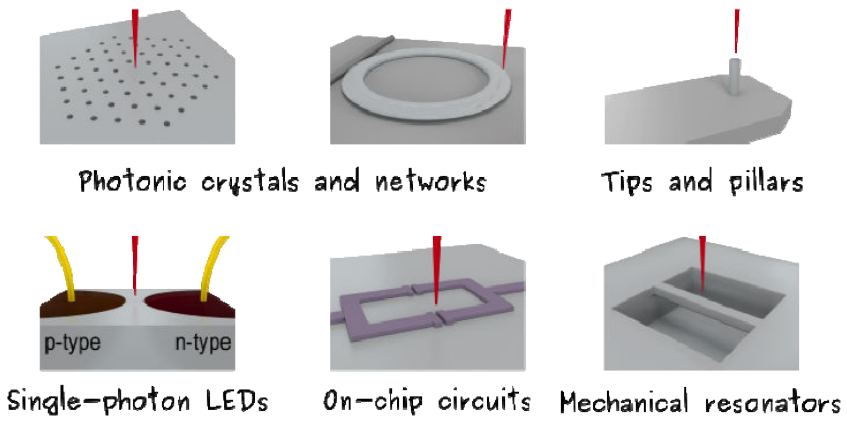

Figure 2.13: Possible applications of FIB technique due to its tight focus beam of ions and capacity to perform targeted placement of the ion species.

Another advantage of the used FIB column is its easiness to work with different gases, which is basically come to the change of the gas bottle and chamber cleaning from the any residuals of previous ions. Indeed the ECR plasma source is moreover able to generate other kinds of ions. The gas source can for example be changed from nitrogen to xenon in order to use the FIB as a milling and micro-structuration tool. Xe ions possess a sputter yield twice higher as gallium ions typically used for milling with FIB columns using liquid metal ion sources. For example, micro-lenses or pillars can be created at the same time as the nitrogen implantation. Such a micro-pillar (10 μm diameter, 5 μm height and surrounded by a 5 μm channel) was fabricated on the same diamond sample using 30 keV Xe^+ ions (Figure 2.14). This milling process may avoid the sample contamination with heavy ions, which occurs with standard gallium FIBs.

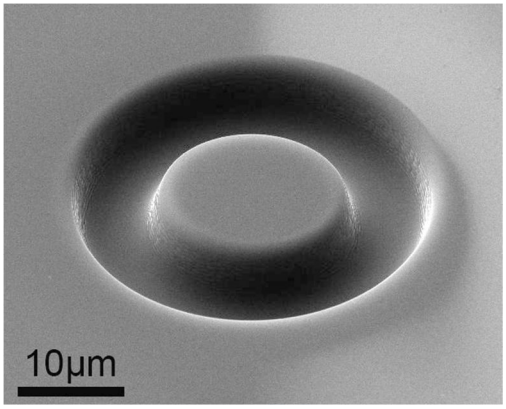

Figure 2.14: Microstructure milled with the focused ion beam of Xe.

CHAPTER 3

Overgrowth

3.1 Introduction

Implantation realized at low energy leads to smaller penetration depth in the sample and, in this case, the properties of the created NV centers can be strongly affected by surface-induced parasitic effects, such as the yield of NV centers formation [56], the control of the charge state [58] and their spin coherence properties [54] (§1.2.3). In this chapter we will investigate if these detrimental effects can be reduced by covering the shallow implanted NV centers with an overgrown layer of ultrapure diamond synthesized by putting the implanted sample in the CVD plasma reactor (see Figure 3.1). We will start with a short concise description of the implantation setup (§3.2) and subsequently describe the experimental results of NV centers implantation close to the sample surface (§3.3.1). We will finally discuss the influence of different overgrowth procedures on the patterns of implanted NV centers (§3.3.2).

Figure 3.1: Schematic representation for the improvement of the properties of shallow created NV centers, based on the overgrowth of an ultrapure layer of diamond material using plasma vapor deposition.

3.2 Nano-beam implantation

3.2.1 Implantation set-up

The energy of implantation is a fine tool for precise ion placement. As already pointed out, ion beams with energy in the keV-range can hardly be focused in a tight spot due to the presence of chromatic aberrations. To avoid this problem, the nanoimplanter used in the experiments we realized at RUBION (Ruhr-Universität Bochum, Germany) during a stay in Jan Meijer's group was designed with an additional collimation based on a pierced atomic force microscope (AFM) tip [62]. Energies well below the 15-keV value used in the previous experiment could then be used in order to decrease the effect of straggling. Moreover, this setup allowed us to reach high accuracy implantation through the nano-hole in the tip, which makes possible the creation of small arrays of coupled NV centers with a placement precision of approximately 20 nm [62].

As in the previous experiment, a gas of nitrogen molecules (N_2) was used as the primary source of ions. The ion column is equipped with a mass separation filter which selects the desirable ion or molecular specie for the implantation. The size of the diaphragm can be changed, but in all presented below experiments its diameter was set to 25 μm. The ion beam is transmitted through a pierced 45°-tilted mirror 3.2, which is used for the on-line positioning control of the sample. The size of the ion beam impinging the sample surface is first controlled using a PMMA layer and observed using an optical microscope. The ion beam affects the surface of the test sample, which becomes darker after the irradiation. In addition the current of the ion beam can be controlled using a Faraday cup and a detecting electron multiplier with a sensitivity of 0.01 pA.

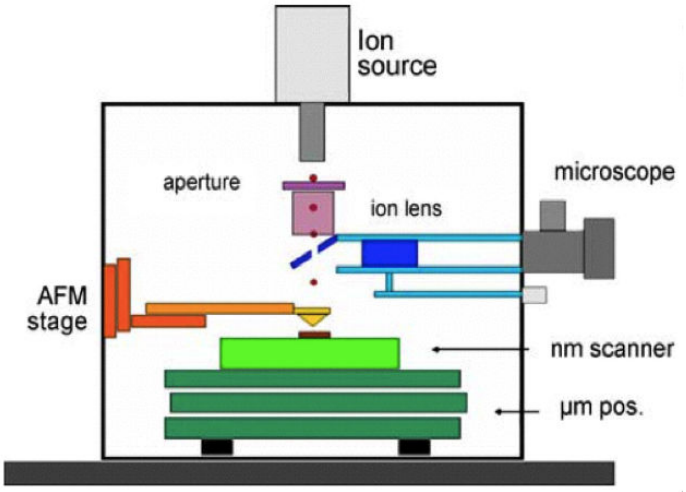

Figure 3.2: Scheme of the implantation chamber realized in RUBION. [87]

3.2.2 AFM tip preparation

The drilling of the holes in the AFM tip is realized using a FIB operated with a gallium ion source [87, 62, 66]. For this a Faraday cup is placed on the axis of the FIB column, and the Ga^+ ion beam is tightly focused on the AFM tip from its concave side. Since the AFM tip is relatively thin, after several seconds of exposure, the ions start to pass through it and as soon as an output ion current is detected by the Faraday cup, the drilling process is stopped.

The AFM tip is made of silicon nitride, which is a perfect insulator without any available free charge carriers. If so it may lead to charging effects of the tip during the ion bombardment. In order to avoid this tentative perturbation over the ion beam, the concave part of the tip is covered with a thin conductive layer. Drilling the holes is then realized at the proximity of the apex of the tip, however not directly at its summit, in order to avoid any contamination of the drilled transmission channel, which could be created by touching the surface of the sample with the AFM tip.

3.3 Experimental results

3.3.1 Shallow implantation

The diamond samples used for the implantation consist of a homoepitaxial CVD layer with a thickness of $\simeq 200$ μm, grown on a HPHT single-crystal substrate at LSPM laboratory (Villetaneuse). Implantation was realized using nitrogen atoms and molecules at energies of 5 kV (5 kV N^+), 2.5 kV (5 kV $N_2{}^+$), 1.5 kV (3 kV $N_2{}^+$), 1 kV (2 kV $N_2{}^+$), 0.8 kV (1.6 kV $N_2{}^+$) and irradiation doses of 3×10^{13} N/cm^2, 1×10^{13} N/cm^2, 3×10^{12} N/cm^2, 1×10^{12} N/cm^2, 3×10^{11} N/cm^2, and 1×10^{11} N/cm^2. Using the results of Monte Carlo Simulations based on the SRIM software [88], the depth of ion implantation was estimated to range from 11 nm to 2 nm accordingly (Figure 3.3).

NV centers in bulk diamond are characterized with a perfectly stable photoluminescence even at room temperature. However implantation performed at low energy (below 2 keV) leads to the creation of NV centers in a close proximity of the surface. Such shallow NV centers are then analogous to NV centers that can be found in detonation nano diamonds with size below 5 nm [89]. These centers display strong blinking and are mostly in the neutral charge state NV^0 [57].

Preliminary experiments, realized in order to investigate the effect of the overgrowth, were performed on ensembles of NV centers which were created with different irradiation doses. The implantation of the sample was followed with annealing at 800 °C during 2 hours in order to activate the implanted N atoms which recombine with vacancies in order to create the NV centers. Finally the sample surface is cleaned in a mixture of boiling acids (1:1:1 nitric, sulphuric, perchloric acids) during 4 hours in order to stabilize the surface charge state and remove any graphite formations, which

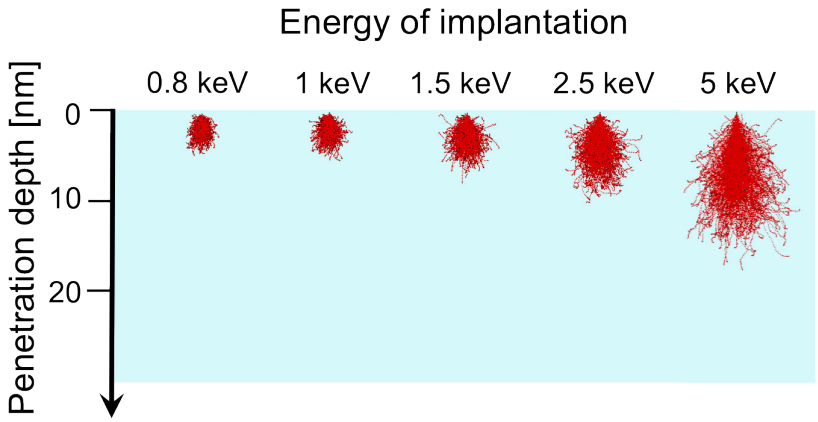

Figure 3.3: Simulations of the implantation using the SRIM software, showing the distribution of the nitrogen ions implanted inside the diamond lattice as a function of the incident kinetic energy of the ion. Since the implantation is realized with a molecular nitrogen beam, the N_2 molecules dissociate when they strike the sample surface and the effective energy of the ion penetrating the matter is equal to half the accelerating voltage of the column.

might have occurred due to implantation damage.

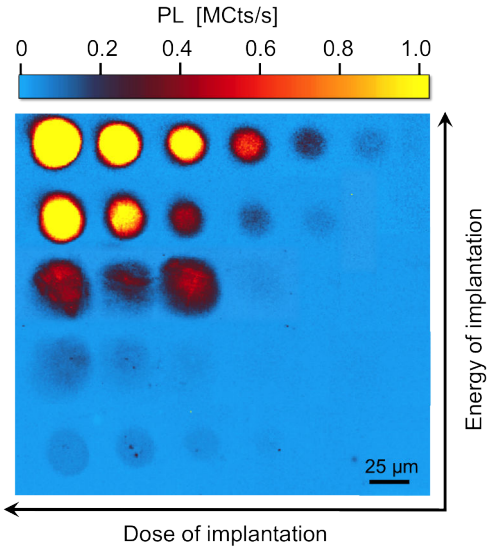

Figure 3.4: Photoluminescence map of ensembles of NV centers, generated by varying the energy of implantation (5 keV, 2.5 keV, 1.5 keV, 1 and 0.8 keV) and the irradiation dose (3×10^{13}, 1×10^{13}, 3×10^{12}, 1×10^{12}, 3×10^{11} and 1×10^{11} N/cm^2). The photoluminescence (PL) is recorded with an optical excitation of 1 mW input power.

As shown on Figure 3.4, the implantation of the nitrogen ions led to the formation of an array of ensembles of NV centers. The size of the generated structures corresponds to the size of the nitrogen beam, with a diameter of 25 μm, except the ones generated at 1.5 keV energy, which are slightly defocused.

For a given energy, the increase of the number of implanted nitrogen atoms as

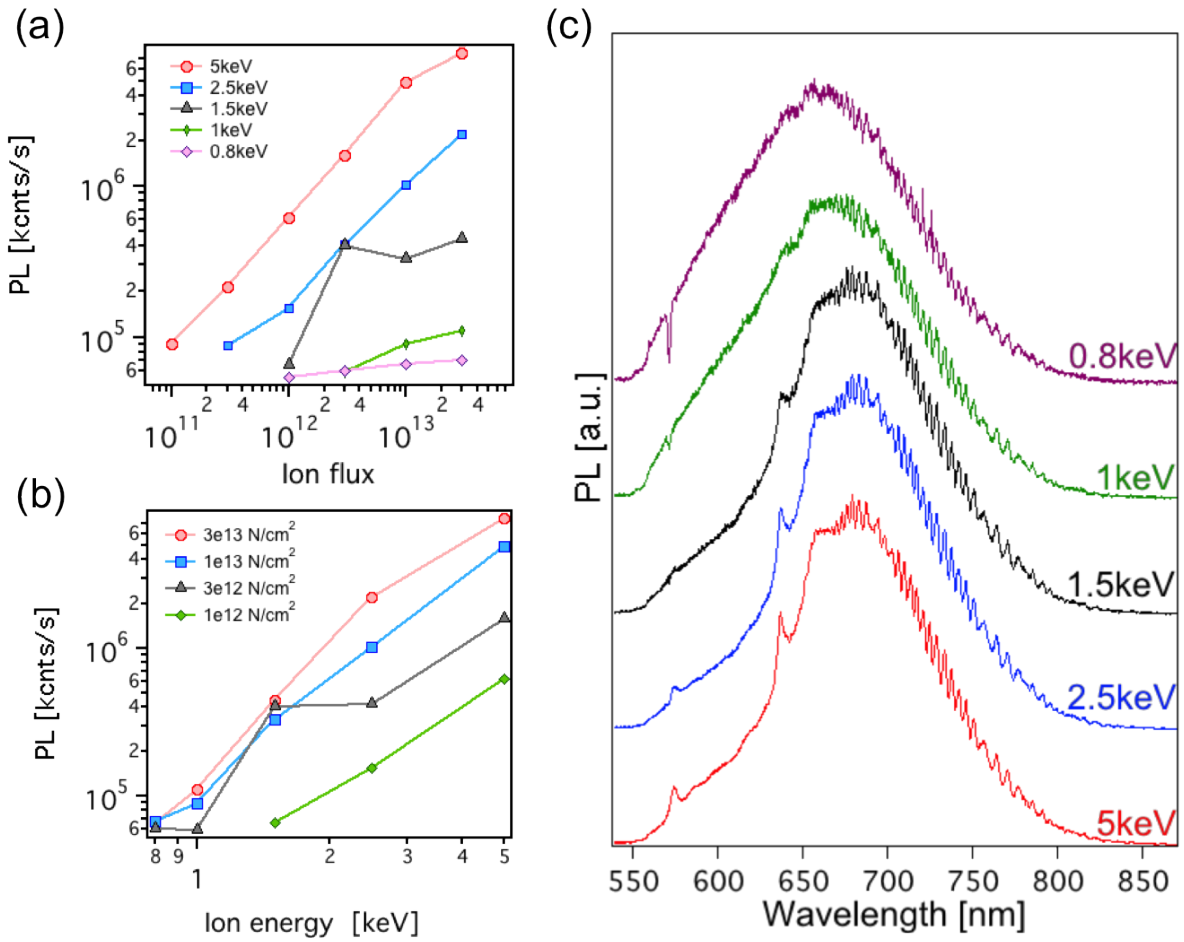

Figure 3.5: Photoluminescence signal detected from the implanted spots shown on Figure 3.4, as a function of the (a) irradiation doses and (b) incident kinetic energies. (c) PL spectra of shallow implanted ensembles of NV centers before the overgrowth.

a function of the irradiation dose leads to a linear raise of the number of created NV centers (Figure 3.5(a)), associated to the increase the number of substitutional nitrogen impurities in the diamond lattice. However the lowest energy used for the implantation (0.8 keV) leads to a smaller yield of N $\rightarrow$ NV conversion even at high implantation dose as shown by the comparison between the slopes of the curves corresponding to 5 keV and 0.8 keV in Figure 3.5 (b). Moreover a higher energy of implantation leads as well proportionally to a higher number of NV centers. Analyzing the PL signal recorded for each spot, we conclude that it has a proportional behavior as a function of the chosen parameters of implantation energy and irradiation dose. Note that the implanted structures at 1.5 keV do not follow this general behavior.

Preliminary characterization of the NV defect luminescence was realized with an optical excitation at 532 nm wavelength. Strong variations of the emission spectrum were observed with the implantation depth. As shown on Figure3.5 (c) the decrease of energy from 5 keV to 0.8 keV leads to the broadening of PL spectra and the shift from NV^- towards the NV^0 emission. The weaker PL signals arising from the implanted spots at low energies (see Figure 3.4) might then be due to the low conversion yield and

also to the charge state of the created NV centers, since the NV^0 center is characterized with a weaker PL intensity than the negatively charged state NV^- [90].

These results confirm the detrimental influence of the surface for NV centers generated by the concentration of shallow implanted nitrogen impurities.

3.3.2 Influence of the capping layer synthesized by CVD overgrowth

The usual procedure for CVD diamond growth requires first to clean and smoothen the surface of the substrate by applying a high temperature hydrogen gas treatment, which introduces a high risk of surface etching. Since the overgrowth performed on a shallow implanted sample, it was crucial to define the plasma conditions which can be used to synthesize a pure single-crystal diamond layer on the top of preserved implanted patterns. To determine these appropriate conditions we used three samples, which were implanted with identical energies and doses, but overgrown under different plasma conditions.

3.3.2.1 "Standard" growth conditions

The first experiment was performed on a diamond layer with a thickness of 210 μm, which was implanted as previously described. Spectra of created ensembles of NV centers showed similar behavior - a shift towards the NV^0 spectrum by getting closer to the surface, as reported on Figure3.5 (c).

Before the overgrowth the implanted layer was cleaned with solvents and acids, then followed by a low-temperature hydrogen plasma treatment. Then, the methane gas was introduced in the chamber once the steady-state growth conditions were reached, *i.e.* when the sample temperature reached 850 °C (3.2 kW microwave power at a pressure of 208 mbar, 4% CH_4). The estimated thickness of the overgrown layer was around 4 $\pm$ 1 μm.

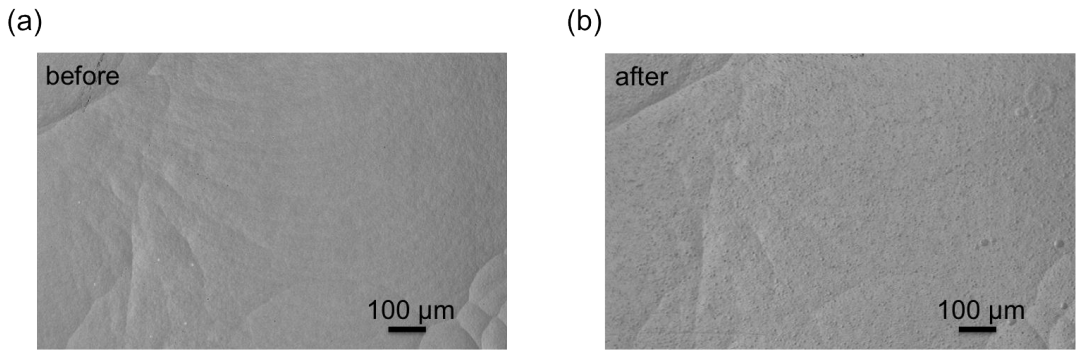

Figure 3.6: Morphology of the sample surface, before and after the overgrowth realized under "standard" growth parameters of the plasma and sample temperature.

It should be stressed out that for these growth conditions the surface morphology remained almost identical after the upgrowth, which gives strong evidence for the good crystalline quality of the deposited single-crystal diamond layer. As shown on Figure 3.6 neither hillocks, nor unepitexial defects appeared, and the sample surface on the both pictures is smooth. Measurements performed using an optical profilometer gave an estimate of the surface roughness between 15 and 17 nm recorded on 50 μm x 50 μm^2 area. Confocal Raman analysis confirmed that the growth realized under these conditions leads to pure single-crystal diamond layer deposition, without any interface between the initial sample and the newly deposited layer. Remarkably, no presence of contaminations like SiV or P1 centers corresponding to single nitrogen impurities was detected.

Unfortunately all the initially implanted NV centers could not be found anymore, even the deepest patterns. We then conclude that this regime for the CVD overgrowth leads to the etching of the surface, with the removal of a thickness of at least 15 nm of initial sample.

3.3.2.2 "Soft" growth conditions

In order to avoid any surface etching and preserve the implanted patterns, the hydrogenation plasma treatment was performed at low temperature. For the same goal, methane was introduced in the chamber before reaching the optimized growth conditions given above. The diamond layer was deposited during 30 min at high-power density (3 kW microwave power, 200 mbar pressure and 4% CH_4).

The thickness of the overgrown layer was roughly estimated by weighting the sample, around 3.5 $\pm$ 1 μm. Figure 3.7 displays surface images before and after the overgrowth. The morphology of the surface has been modified, with the formation of a high number of hillocks and unepitexial defects. This can be caused either by the presence of surface contamination, or by unoptimized growth conditions of the diamond layer.

The creation of the unepitexial defects is usually linked to the formation of dislocations on the interface between the substrate and the overgrown layer. However it should be noted that despite the increased number of morphology-related defects all the implanted patterns of NV centers, including the shallowest one, survived to the overgrowth (Figure 3.7 (c)).

Raman spectra of the overgrown layer recorded with optical excitation at 633 and 488 nm wavelength, showed the presence of contaminations with a strong signal associated to SiV defects (detected emission peak at 740 nm) and NV defects (emission peak at 637 nm), which are not observed by going deeper inside the initial diamond sample (see Figure 3.7 (d) and (e)). This contribution of SiV and NV centers is homogeneously distributed in the bath of the newly overgrown layer. In order to compare the evolution of implanted NV properties all presented spectra on Figure 3.8 were

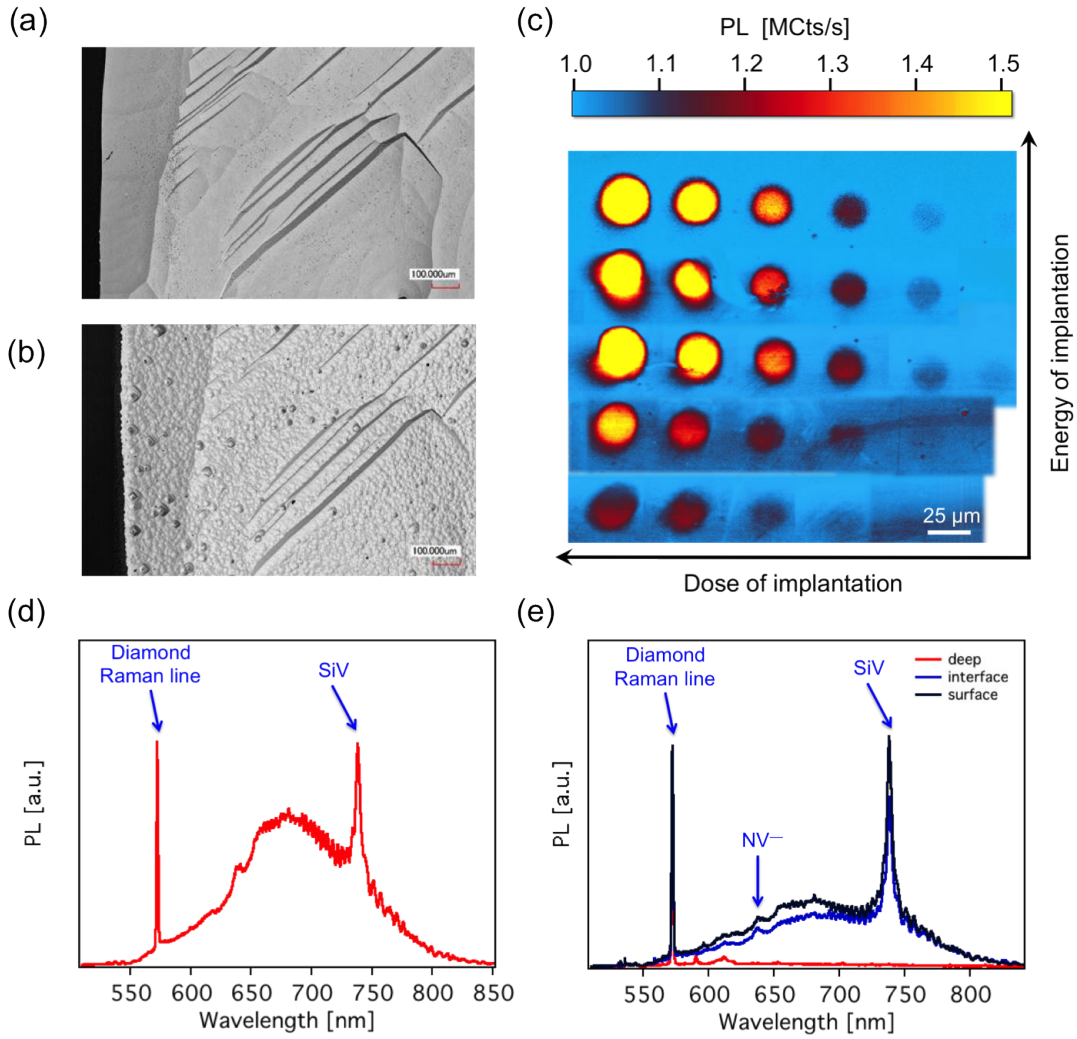

Figure 3.7: Morphology of the sample surface, (a) before and (b) after the overgrowth realized under "soft" growth conditions. (c) Photoluminescence map recorded after the overgrowth of the created ensembles of NV centers by varying the energy and dose of implantation. PL spectrum of one deeply implanted structure (d) and background recorded for different depths in the sample (e).

normalized and background corrected, which then strongly weakens the signal associated to the luminescence of the SiV centers. After the overgrowth all the spectra are not broaden out and show the photoluminescence of NV centers being mostly in their negatively-charged state (Figure 3.8(a)).

Note that for the lowest implantation energy of 0.8 keV, a weak ZPL at 637 nm wavelength appears after the overgrowth (Figure 3.8(a) and (c)). We conclude from these observations that the overgrowth of a thin diamond layer realized with "soft" growth conditions indeed improves the crystalline environment of the shallow-implanted NV centers, leading to features of their PL spectrum which are close to those observed in the case of deeply implanted NV centers.

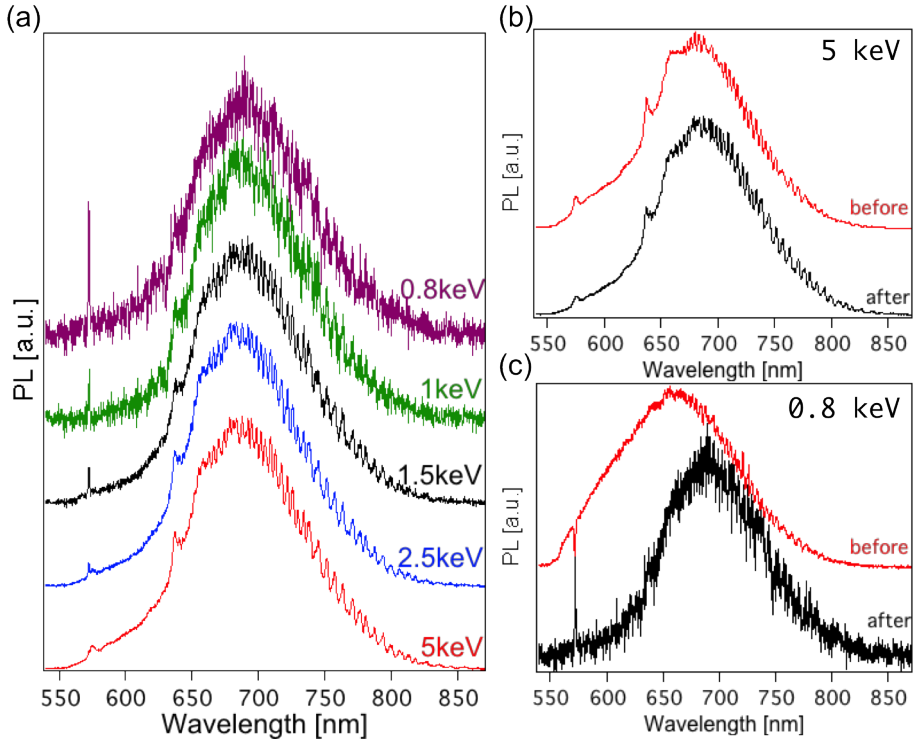

Figure 3.8: Spectral modifications of the photoluminescence associated to the implanted ensembles of NV centers, recorded before and after overgrowth procedure.

3.3.2.3 "Intermediate" growth condition

In this third regime we used a single-crystal ultrapure diamond sample from Element6, with a purity corresponding to the so-called "electronic grade" [91]. As in the previous two experiments, we used a fixed kinetic energy of the ions and a patterned implantation was realized by using a pierced AFM tip (see Figure 3.9 (a)).

By varying the time of exposure of the tip to the focused Ga^+ ion beam two holes were drilled in the cantilever with diameters of 180 nm and 400 nm (see Figure 3.9 (b)) and both single NV centers and small ensembles were created by implanting through these holes (see Figure 3.9 (c)).

Taking into account the sizes of two holes, and the conversion yield of the implanted nitrogen atoms to NV centers as a function of the ion incident energy [56], the first dose used for ion implantation through the hole of 180 nm diameter was set at a value corresponding to the creation of single NV centers. The second irradiation dose was set to a value three times smaller, in order to generate single NV centers using the hole of 400 nm diameter. Finally the doses were set to 5.5×10^{11} N/cm^2 and 1.8×10^{11} N/cm^2 for 5 keV ion energy; 2.2×10^{12} N/cm^2 and 7×10^{11} N/cm^2 for 2.5 keV; 2.2×10^{13} N/cm^2 and 7×10^{12} N/cm^2 for 1.5 keV; 1.5×10^{15} N/cm^2 and 0.5×10^{15} N/cm^2 for 1 keV.

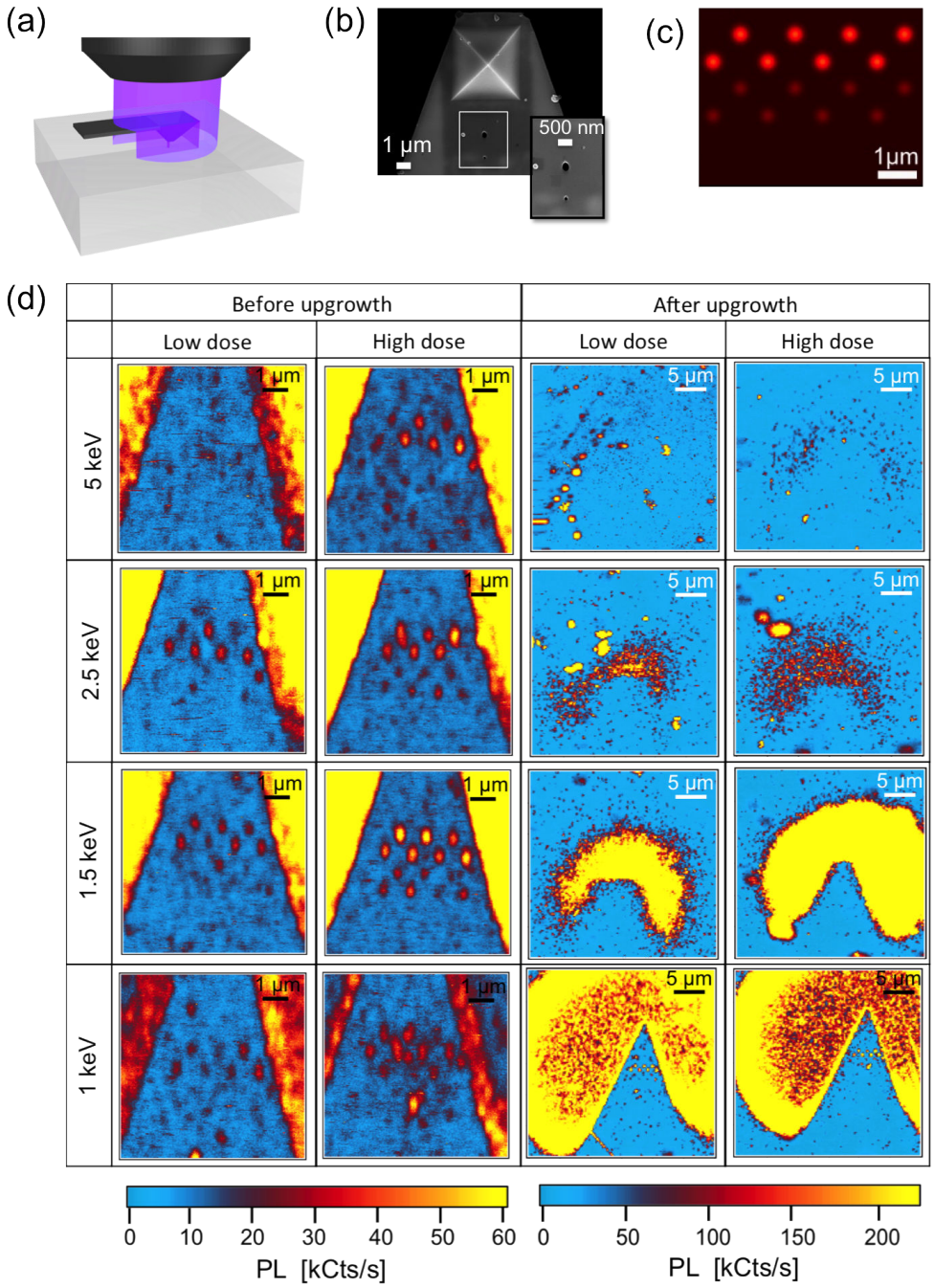

Figure 3.9: (a) Implantation through an AFM tip in order to create patterns of NV centers. (b) The tip is pierced with two holes, of respective diameters 180 nm and 400 nm. (c) Simulated pattern of the performed implantation. (d) Implanted patterns of NV centers before and after the overgrowth. Parameters are an ion energy of 5 keV and doses 5.5×10^{11} N/cm^2 and 1.8×10^{11} N/cm^2; 2.5 keV ion-energy and irradiation doses 2.2×10^{12} N/cm^2 and 7×10^{11} N/cm^2; 1.5 keV ion-energy and doses 2.2×10^{13} N/cm^2 and 7×10^{12} N/cm^2; 1 keV ion-energy and doses 1.5×10^{15} N/cm^2 and 0.5×10^{15} N/cm^2.

The implanted sample was annealed for 2 hours at 800 °C, and then the surface was cleaned in a mixture of boiling acids as previously described. First analysis with

confocal microscopy showed recognizable patterns of formed NV centers (see Figure 3.9 (d)). However all luminescence spots corresponded to defects associated to the neutrally charged state NV^0, even in the case of deep implantation or for spots associated to high nitrogen doping.

Previous works [57, 59, 92] have clearly demonstrated that surface state termination has a strong influence on the charge state of underlying NV centers: the H-termination of the surface favors NV^0, while O-termination leads to mostly NV^- centers [93]. In our case, neither a repeated chemical surface treatment in the mixture of boiling acids which removes residuals of amorphous carbon layers, nor an oxygen plasma treatment intending to create oxygen bonds on the surface [94] could change the charge state of the created NV defects. Therefore it was impossible to measure the initial spin coherence properties of the fabricated NV defects.

The overgrowth procedure started by a cleaning step, with a hydrogen treatment of the sample surface using plasma at low power and low temperature. But for this experiment, the system was switched to medium power conditions, and after the introduction of the methane gas high power conditions for the plasma were reached (3.1 kW of microwave power at 210 mbar of pressure with 4% CH_4). These conditions for the CVD growth were expected to provide the deposition of the diamond layer with a high crystalline quality and, simultaneously to preserve the shallow NV centers from any effect of surface etching [77].

The thickness of the overgrown layer was around 4 μm as in the previous cases. The surface morphology of the sample appeared rather smooth, without formation of unepitexial defects or hillocks. However, the implanted structures were partially removed. Surprisingly a higher degree of damage was detected for the deepest implanted NV centers with 5 keV ion energy, than for the shallowest ones. This effect might be attributed to the dose of implantation. The 5 keV ion energy implantation is characterized with the higher yield, what implies the use of smaller dose of implantation to fabricate a single NV center, compared to the case of implantation realized at 0.8 keV. The fact that the shallowest implantation was still observed in the sample after the overgrowth allows us to conclude that no surface etching occurred during the sample preparation before the deposition of the overgrown layer, whereas a depletion of NV defects probably took place due to hydrogen passivation.

From the patterns associated to the shallowest structures, we can clearly distinguish the preserved NV centers. Moreover this "intermediate" regime for the overgrowth did not induce any undesirable contaminations as observed in the previous case. The measurements of the PL spectra gave an evidence for an improvement of the NV properties, with a charge stabilization due to the acceptors' number minimization (see Figure 3.10 (a), (b)).

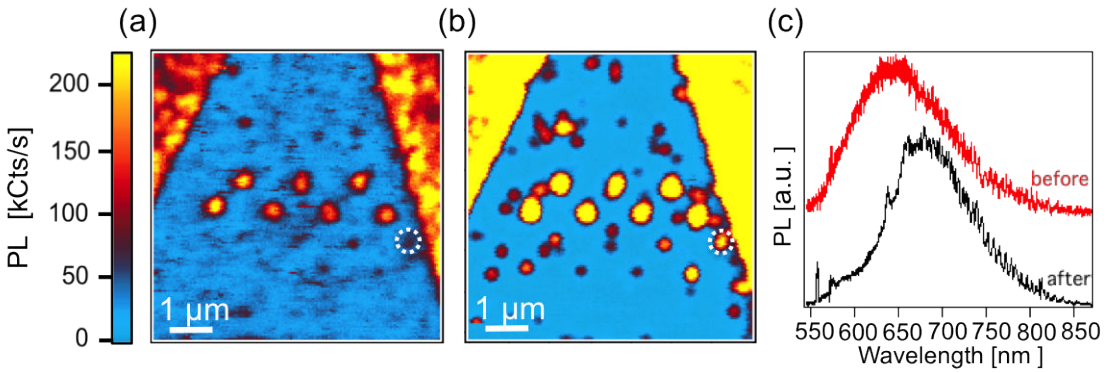

Figure 3.10: PL images of the implanted pattern of NV centers, at 1 keV ion-energy and 0.5×10^{15} N/cm^2 dose recorded at 150 µW of optical excitation power using a microscope objective with NA = 1.35: (a) before the overgrowth, and (b) after. (c) Measured spectra in a particular implanted spot, shown with white dashed line on Figure (a) and (b).

Since in this experiment the implanted species were mainly consisting of ^{14}N isotope, it was necessary to estimate the number of native N impurities, which might have been activated by trapping vacancies created during the implantation. As already mentioned we used a commercial CVD diamond sample from Element6, where the initial nitrogen concentration is specified to be smaller than 5 pp. ("electronic grade"). Such condition corresponds to less than five N atoms per 10^9 sites in the diamond lattice. The unit cell volume of the diamond lattice containing 8 atoms is equal to 0.0454 nm^3, which corresponds to less than five atoms in 6×10^6 nm^3. The diameter of the hole through which the implantation was performed was 180 nm, and the penetration depth the of ions can be estimated from the SRIM simulation. Using these parameters the volume of effective vacancies creation associated to a given spot in the implanted pattern is around 0.52×10^6 nm^3, then hosting less than 0.5 native nitrogen impurity. From this order-of-magnitude, we can then conclude that the NV centers which appeared after the exposure to the ion beam and the annealing are mostly associated to the implanted nitrogen atoms.

Dose-Dependent influence on the overgrowth

Since the dose-dependent behavior of the overgrowth was unexpected and in order to check the repeatability of the results, another sample was prepared. We chose to use an optical grade Element6 sample, which was implanted with an ion energy of 2.5 keV and by varying the dose of irradiation. The sample was then overgrown under identical conditions as previously. The PL signal comparison reproduced the results obtained earlier: indeed, the overgrowth process leads to NV centers density dependent results.

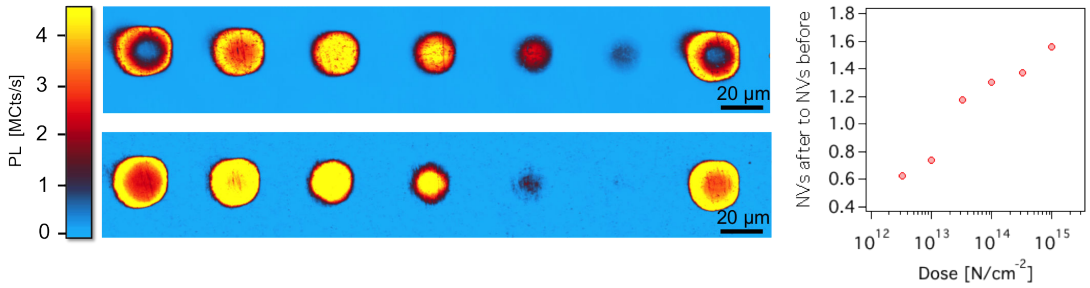

Figure 3.11: PL images of implanted structures in an Element6 optical-grade sample. The implantation was realized with an ion energy of 2.5 keV and doses of (from left to right) 1×10^{15} N/cm^2, 3.3×10^{14} N/cm^2, 1×10^{14} N/cm^2, 3.3×10^{13} N/cm^2, 1×10^{13} N/cm^2, 3.3×10^{12} N/cm^2, and 1×10^{15} N/cm^2. Upper: before the overgrowth, and lower: after overgrowth. The graph indicates the ratio of the number of detected NV centers after the overgrowth to the number of initial NV centers as a function of irradiation dose.

The inset on Figure 3.11 shows the number of NV centers after the overgrowth normalized to the initial number, as a function of the irradiation dose. The ensembles of defects implanted at doses exceeding 3×10^{14} N/cm^2 value, after overgrowth are characterized with an improved yield of conversion from implanted N to active NV centers since the parameter represented on Figure 3.11 is higher than unity. However, for doses smaller than 1×10^{14} N/cm^2, the created structures are characterized with a worsen yield after the overgrowth, the ratio being smaller than unity. However, to fully exclude any etching processes which might have occurred it should be important to see if the implanted nitrogen atoms are still hosted in the diamond lattice. This could be checked by complementary irradiation with for instance electrons in order to create vacancies inside the crystal, and annealing to promote the recombination with the nitrogen atoms already existing inside the lattice.

3.4 Conclusion and perspectives

Ion implantation is a powerful technique which enables the three-dimensional control of the placement of nitrogen impurities, which can be converted into NV centers through the recombination with existing vacancies. Decreasing the energy of implantation below 1 keV leads to the creation of NV centers within a spot of approximately 5 nm. However such shallow point defects interact strongly with the surface and its possible imperfections, leading to parasitic effects. In order to improve the crystalline environment around such centers and remove the detrimental influence of the surface we investigated the efficiency of an overgrowth technique, for different regimes of the CVD growth in the plasma chamber.

The overgrowth realized with “standard” plasma parameters, which were optimized for the homoepitexial growth of an ultra pure single-crystal diamond layer led to an

overgrown layer with almost ideal crystalline quality that could not be distinguished from the initial sample. Unfortunately the plasma conditions induced an etching of at least 15 nm below the surface and none of the implanted NV patterns could be detected after the overgrowth. A decreased temperature for the diamond preparation step to the overgrowth in "soft" conditions allowed us to preserve the shallow implanted structures with a stabilization of the NV center in its negatively-charge state. Nevertheless the newly deposited layer hosts impurities such SiV centers and NV centers not correlated to the implantation.

An "intermediate" regime for the plasma was finally investigated. An improvement of the photoluminescence of shallow created NV centers was observed, which can be qualitatively understood by preserving the negatively-charged NV centers from the ionization associated to electron traps on the surface [95]. Moreover an improved crystalline quality of the overgrown layer can be achieved by slightly increasing the temperature of an initial hydrogen-plasma treatment, and since the initial patterns of NV centers created by implantation can be observed after the overgrowth, this "intermediate" regime combines the advantages of the two regimes previously studied. Further studies are now required to check if these clear improvements lead to better coherence times for the electron spin of the implanted NV centers.

CHAPTER 4

CVD-based δ - doping techniques for the engineering of thin NV-enriched layers

4.1 Introduction

Fabrication of thin highly doped with NV defects layer can be realized using ion implantation technique, however the condition of the surface proximity requires low energy implantation, which is characterized with low conversion yield. In this chapter we will demonstrate another method to form stucked layers by a direct gas insertion to the growth chamber while diamond deposition (§4.2.1). We then discuss an alternative method of NV centers doping control by temperature variation (§4.2.2).

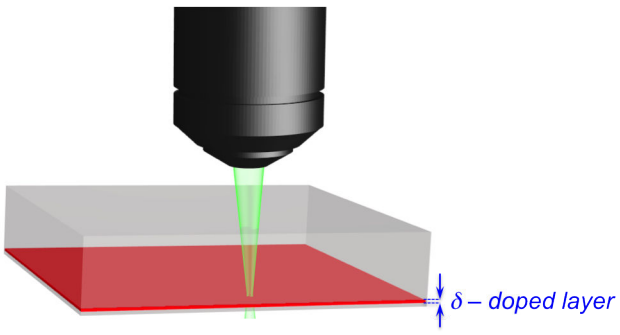

Figure 4.1: Schematic representation of the magnetic field sensor based on the ensemble of NV centers. In such configuration the copper wire is attached to the δ-doped diamond side. The magnetized sample for the imaging is placed below.

4.2 Experimental results

The substrates for the present experiments related to diamond growth are (100) - oriented HPHT single crystals, purchased from *Sumitomo*. These samples are classified as Ib crystals with a high initial content of nitrogen. It should be noted that both top and lateral sides were {100} - oriented. Each experiment was started with the deposition of a buffer layer not thinner than 40 μm in order to bury the poor-quality diamond substrate and provide pure crystalline base for the CVD-enabled diamond growth. The growth conditions for the buffer layer were similar in all experiments, which are discussed in this chapter. The microwave power was set to 3.5 kW at a chamber pressure 250 mbar, a substrate temperature was 850° and 4% CH_4 insertion, no intentional nitrogen impact. The diameter of the plasma ball was around 5 cm. Such growth conditions usually result in the deposition of a high-quality deposited layer of single-crystal diamond [77]. However it should be noted that in order to keep the diamond sample as pure as possible all the growth experiments were realized at once without any interruption of the plasma [96].

In all the experiments described in this chapter, the diamond growth was performed on the identical substrates. After the CVD deposition all the grown samples were cut and polished in Almax easyLab, Belgium, whose polishing capabilities can allow the roughness control down to 1 nm. Optical characterization measurements for all the experiments were performed from the cutoff side as illustrated on Figure 4.2.

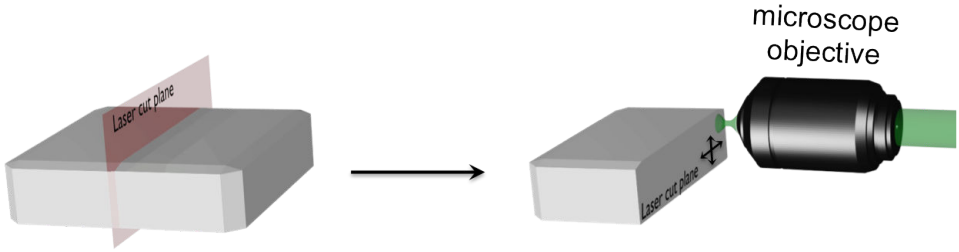

Figure 4.2: Scheme of the laser cut for all the grown samples.

4.2.1 δ - doping by variation of N gas flux

The aim of the first experiment was an estimation of the incorporation of the nitrogen ions and the creation yield of the NV centers as a function of the gas flow in the growth chamber. The substrate used in our experiment was 3×3×1.5 mm, (100)-oriented HPHT single-crystal of a type Ib, first covered with a 40-μm thick buffer layer. The deposition of the CVD layers was realized at standard growth conditions identical to those used for the buffer layer, but with a variable flow of the N_2 gas in the reaction chamber.

The growth time was set to 30 minutes for the two doped layers corresponding to 50 ppm and 100 ppm of intentionally introduced N_2 gas. Between them an undoped

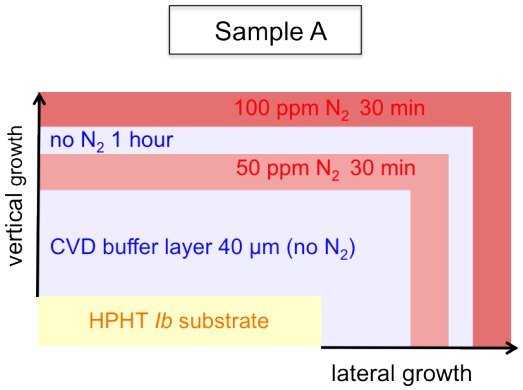

Figure 4.3: Scheme of the first grown diamond sample. 'Sample A' was synthesized with direct N_2 doping and consisted of two nitrogen-doped layers with 50 ppm and 100 ppm nitrogen-content. The layers were separated with a layer grown without any intentional N impact.

spacer was grown during one hour. A schematic representation of the foliated deposited structure is presented on the Figure 4.3.

Previous works showed that nitrogen incorporation during the diamond growth may affect the morphology of the grown sample surface [97, 98, 99]. It happens since the nitrogen incorporation breaks the uniformity of the growth steps and leads to the appearance of step bunching edges, finally resulting in a sample surface modifications: consisting of large number of coplanar {100} facets. Therefore one of the verified parameter while these experiments was the control of the surface morphology which was analyzed with 3D laser microscopy (Keyence VK9700). By employing two light sources: the laser source operating at short wavelength and a white light source, 3D laser microscope enabling to get the information about the real color of studied object and surface roughness in a noncontact mode.

After the growth experiment the total thickness of the deposited layers was estimated to be around 75 μm. Than the sample was cut and polished and proceed the optical characterization measurements using the standard confocal set-up described in appendix A from a cutoff side.

The PL analysis performed along the vertical growth direction showed well-detected stacked layers of diamond doped with NV defects (Figure 4.4 (b)). Spectral analysis done at room temperature showed the presence of negatively as well as neutrally charged NV centers, corresponding to the peaks at 637 and 575 nm wavelength. The high ratio of NV^- was attributed to sufficient number of substitutional nitrogen (N_s) in the diamond lattice providing efficient doping level of the electron donors.

As shown in Figure 4.4 (b) and (d) the nitrogen incorporation along the vertical growth direction is slightly different from the lateral direction. NV centers formation which appeared on the top of the sample is relatively inhomogeneous, and the record of the bright lines gives an evidence for some preferential incorporation at the step-edges [100], which finally lead to the surface effects previously described. However, the

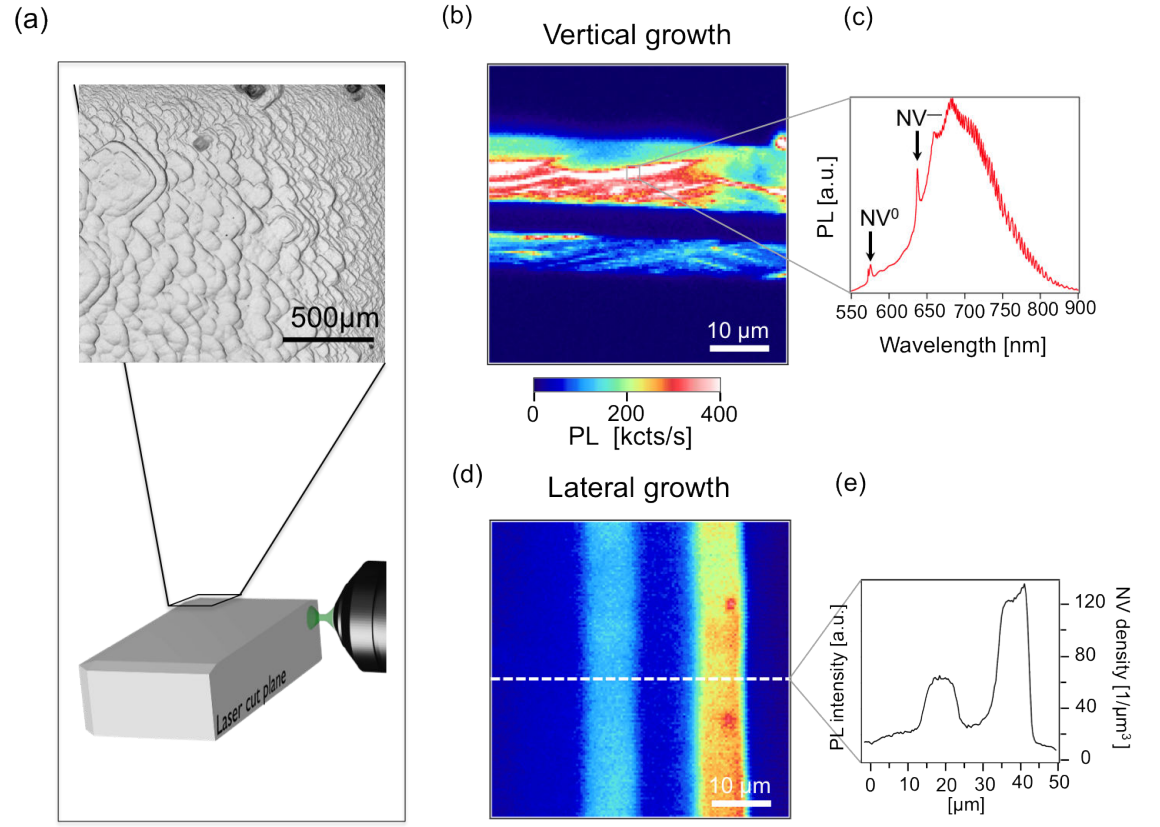

Figure 4.4: Characterization of the sample A. (a) Morphology of the diamond surface after the growth procedure. (b) PL image of the vertically growth layers, spectral measurements on the doped layer with the highest nitrogen content. (d) PL image layers grown in the lateral direction and (e) corresponding image profile along the white dashed line.

incorporation of the nitrogen atoms on the sides of the diamond sample is more uniform. This dissimilarity might be due to the slight difference in the sample temperature during diamond growth either on the top or on the sides of the sample.

The nitrogen-incorporation efficiency was roughly estimated by the ratio of the detected PL signal from the sample to the detected fluorescence from a single NV center. The density of NV defects in doped layers was then estimated to be 130 and 60 $NV^-/\mu m^3$ for the 100 ppm and 50 ppm respectively. The approximate creation yield of inserted nitrogen coming from the growth chamber to formed NV centers is about 10^{-5}, a value in good agreement with the previous research reported by Tallaire et al. [45]. In addition, the thickness of the three deposited layers is different as it was expected. It happens due to the acceleration of the growth rate with the nitrogen insertion in the chamber. For example, the rate of growth for spacer without any intentional N_2 is 5 μm/h, but for the 50 ppm and 100 ppm nitrogen concentration in the chamber the growth rate reaches 18 and 25 μm/h respectively.

It should be pointed out, that even with abruption of the nitrogen gas insertion, a few nitrogen atoms will still remain in the chamber, then leading to appearance of some tail area instead of a sharp border between the doped and undoped layers. The

gas residual time in the chamber may be described using the following expression:

$$t_r = \frac{V_{ch} \times P}{F_{total} \times P_{atm}} \tag{4.1}$$

where t_r is the gas residence time, V_{ch} is the volume of the plasma chamber, P is operating pressure in the reactor (250 mbar), P_{atm} is atmospheric pressure equal to approximately 1000 mbar, F_{total} is the gas flow inserted in the chamber (the unit of the gas flow is expressed in sccm - standard cubic centimeters per minute). It should be noted that in equation is neglected any temperature effect due to the small volume of the high temperature plasma with the respect to the chamber volume.

For example, in our case the gas flow was fixed to 500 sccm, which was inserted in the growth chamber with a volume of approximately 22 liters. The residence time can be estimated of about 10 minutes. However nitrogen incorporation provide higher growth rate of the CVD diamond due to the bonds lengthening [101], therefore 10 additional minutes of deposition becomes an obstacle heading towards thin doped layer formation.

Eq. 4.1 shows that the residence time can be minimized by decreasing the volume of the growth chamber or by changing the nitrogen-gas flow. Another possibility is an alteration of the diamond growth conditions, such as decelerating the speed of growth by decreasing the microwave power and $\%CH_4$. This may lead to the thinning of the nitrogen-doped layers, however usually small growth rates are associated to lower diamond crystal qualities. Moreover it may provoke the drop of nitrogen incorporation efficiency, mainly due to poor N_2 molecules dissociation in the condition of low power densities of the plasma. The decreasing of the nitrogen incorporation efficiency is unwanted for such applications as wide-field magnetic sensing, since it will affect the sensitivity of such magnetometer [11].

Summarizing the results obtained on Sample A, it should be noted that direct nitrogen doping during the deposition process leads to the formation of a high density of NV centers, even at relatively low flow of the nitrogen gas flow in the chamber. Further improvement in the minimizing of the thickness of the doped layer remains a challenging task, since any growth parameter change may worsen the diamond quality as well. An alternative technique for the NV centers'-doped layers creation is based on the temperature variation [77].

4.2.2 δ - doping by variation of the growth temperature

4.2.2.1 Incorporation efficiency of nitrogen impurities

Previous work has reported the possibility of readily nitrogen incorporation with the decreasing of the growth temperature [77]. Therefore this effect can be used for the creation of homogeneously doped and sandwiched layers by slight temperature variation while continuous deposition of CVD layers. In order to estimate the efficiency of the

nitrogen incorporation the following sample was deposited - sample B (scheme of growth is presented on Figure 4.5).

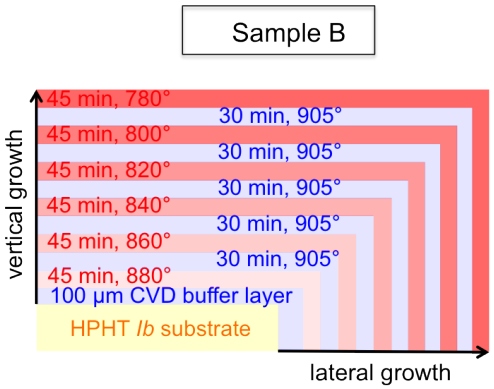

Figure 4.5: Scheme of the second grown sample - 'Sample B'. It was associated to the temperature dependent growth conditions.

At constant gas phase composition in the growth chamber high temperature (905 °C) grown layers were alternated with graduatingly decreasing temperature for the deposition of the each diamond layer (880 °C - 780 °C) in the absence of intentional nitrogen insertion. This temperature variation was achieved by alternating the pressure in the reactor (220-250 mbar range), which took approximately 1 minute. Even by few mbar alternation of the reactor pressure the gas temperature in the plasma can be changed [102]. Moreover it affects the sample surface, which is placed on the cooled stage in the PACVD reactor. The temperature measurements were performed with two-color pyrometer (based on the principle of the thermal radiation measurements).

The final thickness of the grown layers of sample B was estimated to be 150 μm. The absence of nitrogen gas injection during the growth provides a diamond surface of higher quality in comparison to the previous sample A. Indeed, as shown on Figure 4.6 (a) the surface morphology of the sample B is smooth and does not exhibit any step bunching. Using the confocal set-up the PL studies were done along the lateral and vertical growth direction. Performed preliminary characterization did not evidence any NV formation along the vertical direction growth. This fact was mainly aroused by the lack of vacancies, which can be created by postprocessing using electrons or ^{12}C atoms irradiation [103]. Therefore the sample was then irradiated with electrons at 10 MeV kinetic energy and flux 5×10^{15} e^-/cm^2 (Universität Leipzig, Leipzig, Germany). After the sample annealing a higher conversion yield was detected [104]. However similar behavior of the N-ions incorporation efficiency was still observed - lateral growth tends to higher NV centers' incorporation efficiency formation, than vertical.

As expected from the Reference [77] decrease of the growth temperature leads to a more efficient nitrogen incorporation in the diamond layer. However since the number of optically active NV centers was increased by post-processing the sample (vacancies creation and annealing), the nitrogen incorporation occurs mostly as substitutional nitrogen atoms in the lattice. Figure 4.6(b) shows the transformed incorporated im-

purities into NV centers after the electron irradiation and annealing for both growth directions.

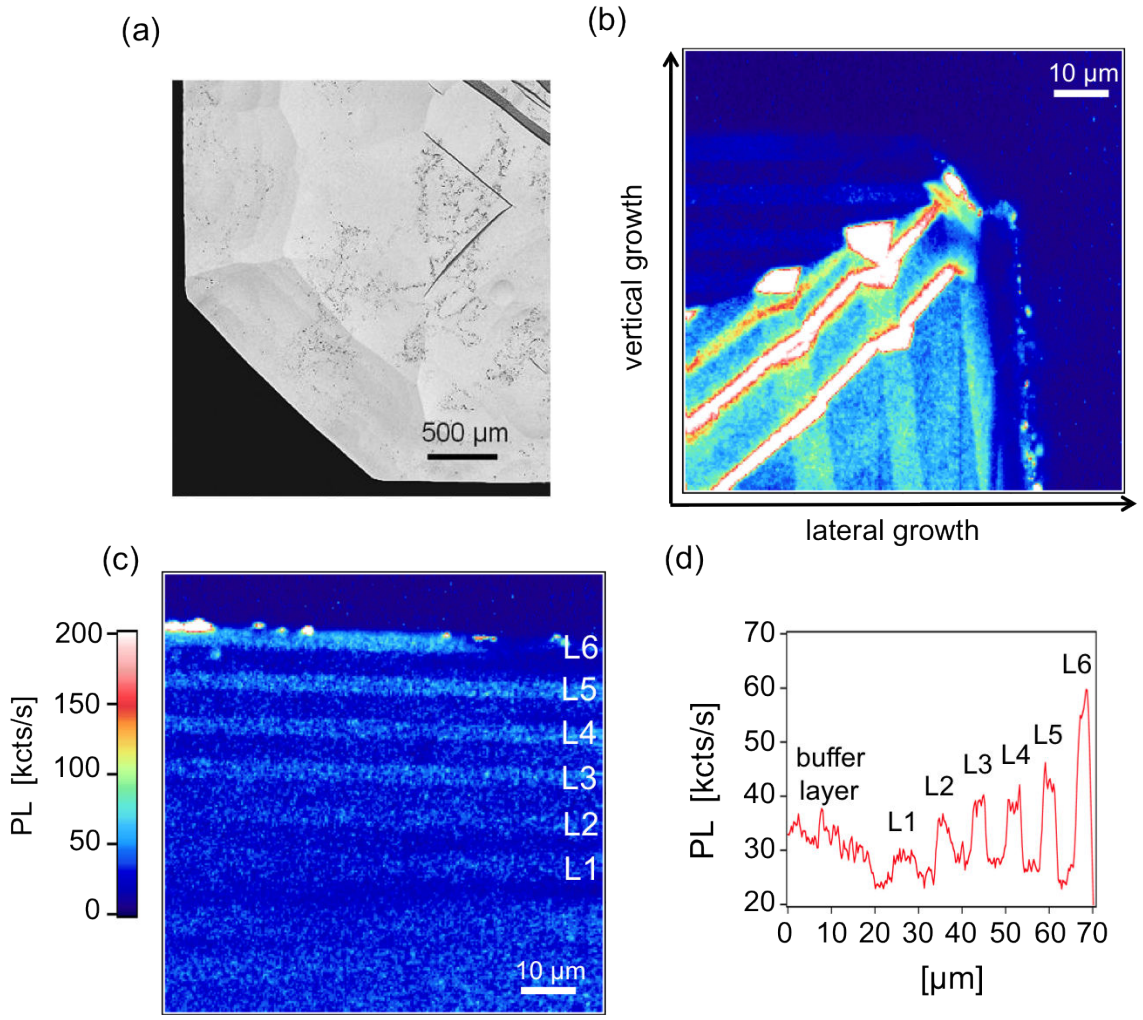

Figure 4.6: Sample B devoted to study the influence of the temperature over the nitrogen incorporation. (a) Microscope image of the surface morphology. (b) PL image of the lateral and vertical grown layers and just lateral grown layers ant its (c). (d) Image profile of the deposited layers in the lateral growth direction.

Figure 4.6(c) shows the PL image of the foliated structure which appeared along the vertical growth direction. Its cross-section image (Figure 4.6(d)) confirms the raise of the efficiency of the nitrogen incorporation with the temperature deterioration, the lower temperature the higher concentration of substitutional nitrogen in the lattice. The nitrogen impact is almost proportional to the the value of decreased temperate, however PL signal attributed to L3 and L4 layers is nearly similar. That might happened due to some surface imperfections, moreover difference of the temperature of the growth is only 20 °C. The created doped layers have a homogeneous NV concentration, since there is no preferential incorporation on the step-edges. However it should be noted that it may be linked to smaller densities of the NV defects incorporation, than for the Sample A. Since the Sample A was analyzed without any post-processing

and it could contain much higher number of substitutional nitrogen affecting stronger diamond growth.

Summarizing the nitrogen incorporation experiment, it could be concluded that the temperature decrease indeed provides a higher number of substitutional nitrogen atoms in the diamond lattice. If to compare the lowest temperature which was tried for growth - 780 °C (layer L6) and the interlayers which were grown at 905 °C, one can notice that the PL signal associated to L6 layer is almost 3 times higher than the spacers PL. However the difference could be even improved for growth temperatures between 700 °C and 1000 °C. This range corresponds to the usual temperature condition for the deposition of the good quality CVD diamonds.

For the next experiment in order to avoid addition electron treatment and increase the NV centers incorporation efficiency it was decided to combine both techniques of nitrogen doping. The diamond growth experiment in the combination of slight N_2 gas insertion and at the same time by varying the temperature of growth as well.

4.2.2.2 NV centers' layer thinning experiment

A clear advantage of the nitrogen-incorporation by the control of the growth temperature in comparison to direct insertion by varying the nitrogen gas flux in the plasma is the higher speed of switch between doped and undoped layers. It provides better control of the doping process, which can be used in order to minimize the thickness of the doped layer. Therefore the next experiment was devoted to the thinning of the doping layer, which requires only the switch from low to high temperature and growth time minimization.

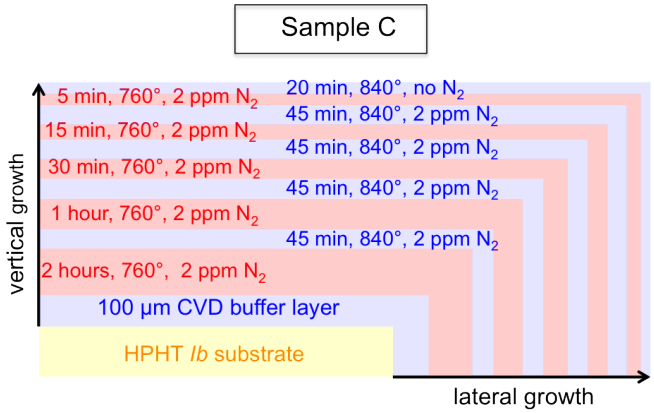

Figure 4.7: Scheme of growth of the sample B. Five low temperature (760°C) deposited layers during the time 120, 60, 30, 15 and 5 minutes were separated by 4 high temperature (840°C) 45 minutes grown layers while 2ppm of N_2 insertion. On the top of the sample was deposited a cap layer, without intentional gas insertion during 20 minutes.

The third experiment was realized following the scheme of growth presented on Figure 4.7. In order to verify the thickness variation of the doped layers as a function of growth duration, the layers grown at low temperature (760 °C) for different time

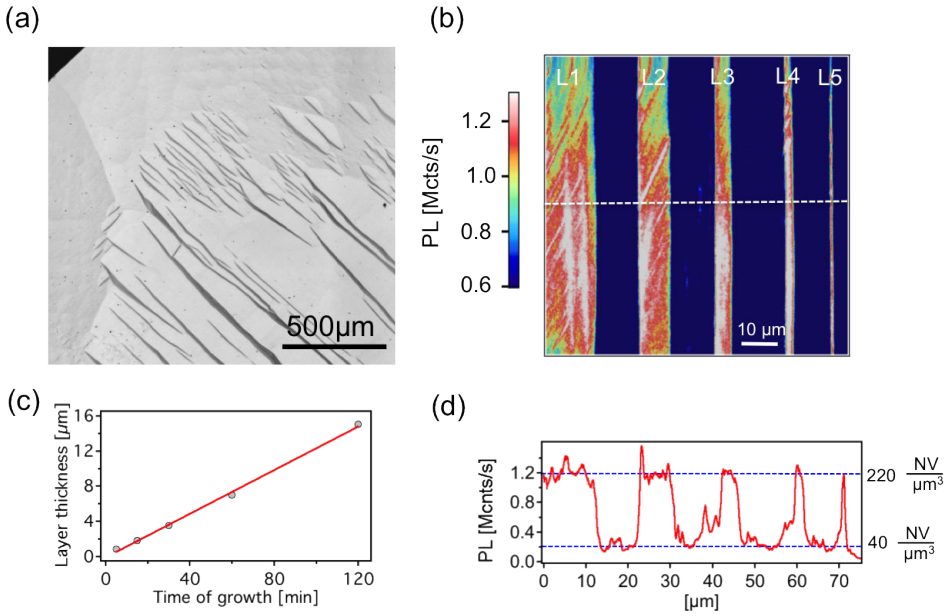

Figure 4.8: (a) Surface microscope image of the as-grown sample. (b) PL image of the foliated deposited structure, where bright lines correspond to high concentration of NV centers. (c) The thickness of the grown layer as a function of the time of deposition. (d) Line profile of the Sample C deposited structure plotted along the white dashed line.

of deposition ranging from 2 hours till 5 minutes were altered with layers grown at high temperature. During all the deposition process apart the final capping layer in the chamber was added 2 ppm of the N_2 gas in order to increase the incorporation efficiency.

The surface of as-grown sample had a small number of step-bunching as shown on Figure 4.8 (a). However first confocal measurements showed that nitrogen gas insertion with 2ppm concentration is not enough for a directly detectable formation of NV centers in the vertical direction. No post-processing of the synthesized sample was done, therefore all the further presented results were measured on the laterally grown part of the sample.

As shown on the Figure 4.8 (b), all the low-temperature stripes are easily detectable with high contrast between doped and undoped layers. However it can be seen that some preferential NV defects formation are still observable on the PL scan images, but not as numerous as in the case of only nitrogen gas insertion. The chosen growth durations from 2 hours to 5 minutes, lead to the fabrication of highly doped layers, which are characterized with similar PL intensities provided by similar incorporation efficiency 4.8 (c). The thickness of the largest layer was found to be 15 μm and the thinnest one was 850 nm Figure 4.8 (c). PL signal levels noted with the blue dashed lines correspond to NV densities of 220 NV/μm^3 in the lines and around 40 NV/μm^3 between the doped layers. The defects' density was estimated from the ratio of detected PL signal from the NV centers formed in the L5 line and PL signal of a single NV to

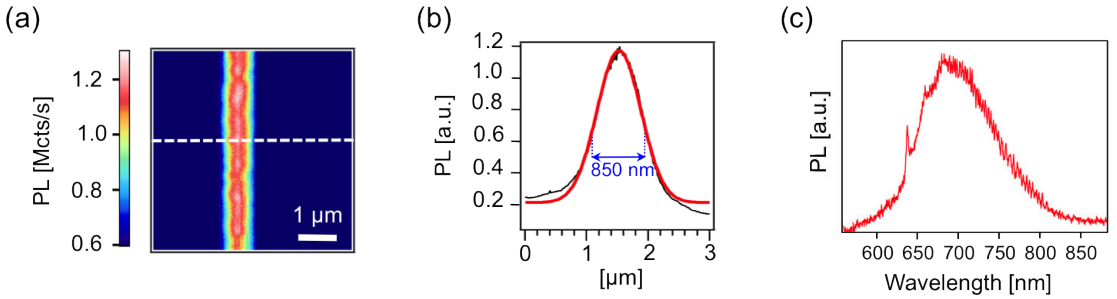

Figure 4.9: (a) Zoom on the thinnest fabricated line denoted as L5 and its (b) line profile fitted with a Gaussian function with FWHM $\approx$ 850 nm. (c) PL spectra measured on the ensemble of NV centers formed in the thinnest line L5 of the Sample C.

be 10^{15} NV/cm^3. Despite this estimation is rather approximate, it is in good order with reported earlier measurements of magnetic field sensing experiments based on ensembles of NV defects [105][38].

It should be noted that the zoom-in on the thinnest fabricated line presented on Figure 4.9 (c) and (b) is rather uniform. In addition the spectral measurement of the PL signal showed mixing between negatively and neutrally charged NV centers in the thin line, but negatively-charged NV centers are predominant. One may conclude that NV^- centers formation is rather limited with the number of created vacancies, than the number of available donors of electrons.

It should be noted that presented images were recorded using a standard optical confocal system, whose diffraction limited resolution is around 250 nm. Tacking into account the convolution by the diffraction peak the thickness of the thinnest layer L5 is 500 nm. The growth rate was estimated to be 7 μm/h for the low temperature growth condition and 10 μm/h for high temperature. For the future experiments aimed to minimize the layer thickness it could be still possible to decrease the time of deposition and as well deceleration of the growth rate may provide even smaller layers.

It should be noted that obtained results for the Sample C are still remaining worse, than earlier published one [74, 47, 75], but it could be further improved by varying the time of growth while low temperature regime and in addition to use bigger temperature difference between high and low temperature growth. However already at this point temperature dependent diamond doping can be considered as a proof-of-principle for delta-doping tasks.

4.2.2.3 Measurement of the spin coherence properties

Most of the applications of NV center either for quantum information processing or magnetometry requires on good coherence properties of the electronic spin. Therefore it was important to ensure of long or at least comparable T_2^* value with the one of usual native NV centers appearing in ultra-pure diamond samples grown on a (100)-oriented substrate.

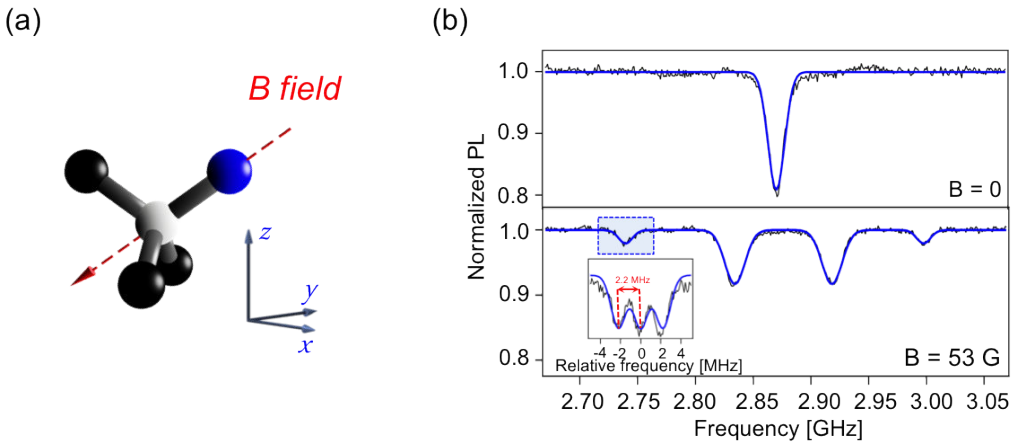

Figure 4.10: (a) Schematic representation of the B field axis (red dashed arrow) aligned along the [111] crystal axis. (b) Typical ESR measurements at the zero magnetic field (upper graph) and at 53 G applied along the [111] crystal axis (lower graph).

A typical room-temperature electron-spin resonance (ESR) is shown on Figure 4.10. It was measured by detecting the PL signal while applying microwave field sweeping the frequency at the absence of external magnetic field [24]. The detected resonance at 2.87 GHz corresponds to a zero-field splitting transition between $m_s = 0$ and $m_s = \pm 1$ spin sub-levels of the negatively charged NV centers. Applying a static magnetic field along the [111] crystallographic axis allows us to lift the degeneracy between the $m_s = +1$ and $m_s = -1$ levels due to Zeeman effect for all four possible orientations. In addition the magnetic field aligned in the [111] axis provides two possible groups of NV centers splittings: one of four orientations of NV will experience the absolute value of magnetic field and three others will have smaller. Moreover three other groups of NV centers will exhibit a similar splitting since they possess the same projection of the applied B-field along their axis (Figure 4.10). The inset is showing a zoom of the extreme left resonance displaying the hyperfine structure due to the coupling of the electron spin with the ^{14}N nuclear spin.

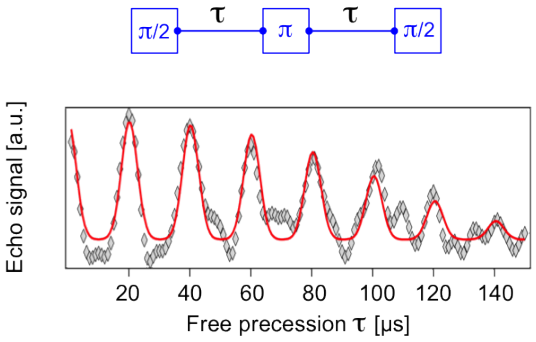

Figure 4.11: Measurement of the spin coherence time using Hahn Echo sequence consisting of two $\pi/2$ and one π pulses, which are separated with free evolution duration time τ. The echo was recorded with external magnetic field equal to 53 G aligned along the [111] crystallographic axis.

Then focused on the lowest frequency resonance, which corresponds to the well aligned [111] - magnetic field orientation, in order to apply the Hahn-echo pulse sequence. As can be seen from Figure 4.11, the spin-echo PL signal exhibits characteristic collapses and revivals of the electron spin coherence induced by the Larmor precession of nuclear spins associated to the ^{13}C atoms in the lattice with 1.1% isotopic abundance [106, 42]. The decay of the envelope indicates coherence time $T_2 = 232 \pm 7$ μs. This value stays comparable to the known earlier values of T_2-time for diamond samples with the same natural abundance of ^{13}C [42]. We then can conclude that spin-coherence properties are protected for the thin highly doped layers of NV centers which were created using with the temperature variation method.

4.3 Conclusions and perspectives

Summarizing the chapter devoted to two diamond delta-doping techniques first of all should be noted that the use of plasma-assisted CVD growth technique at the high power density regime provides highly doped layers of diamond even in the condition of moderate gas insertion. In particular the density of the NV centers created at the condition of 3.5 kW of the microwave power and relatively low N_2 addition (ppm range) can be $>10^{12}$ cm^{-3} and preserving good crystalline quality. However the precise lateral control of the diamond doping becomes hard in the condition of high rates of growth and long residence times of inserted nitrogen ions in the chamber.

Therefore we proposed an alternative method of diamond δ-doping technique, based on the condition of the growth temperature. The change of temperature can be achieved faster than gas interruption process. In addition it was demonstrated that growth temperature deterioration leads to the proportional increase of the number of incorporation of substitutional nitrogen atoms, which can be converted in NV defects by post processing the sample. Combination of low temperature growth with slight constant doping allows to obtain uniform and thin doped layers of diamond. Despite the decrease of the growth temperature condition created NV defects in the thinnest layer exhibit still comparable coherent properties to a conventional growth methods.

Thin diamond layers containing a high number of NV defects will find applications for magnetic field imaging. However further improvements are still possible as, for instance, doping in the isotopically purified diamond with the reduced thickness of the NV centers' containing layer. In addition magnetic field sensor based on ensemble of NV centers uses only group of NV aligned along one of 4 crystallographic axis. Therefore the recent publications devoted to the possibility of the orientation control of NV center could improve their sensitivity. It can be done by using higher number of NV to measure the B field and consequently lower number will impact to the noise. Moreover it might be used for the increase of the PL collection efficiency. Therefore it was decided to explore the possibility to control the NV centers' orientation, what will

be described in the following §5.

CHAPTER 5

Deterministic preferential orientation of NV centers

5.1 Introduction

In this Chapter we will show that the orientation of nitrogen-vacancy (NV) defects in diamond can be efficiently controlled through chemical vapor deposition growth on a (111) and (113)-oriented diamond substrates (§5.2 and §5.3). More precisely, we demonstrate that spontaneously generated NV defects are oriented with a high probability along the [111] axis, corresponding to the most appealing orientation among the four possible crystallographic axes.

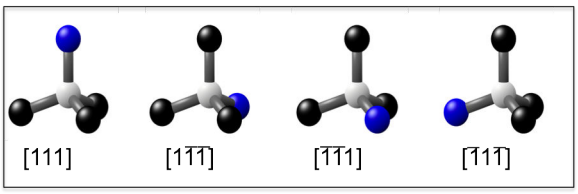

Figure 5.1: Schematic representation of the four possible orientations of NV defects in a (111)-oriented diamond sample, where the light-grey, blue and black balls represent vacancy, nitrogen and carbon atoms respectively.

This work is a significant step towards the design of optimized diamond samples for quantum information and sensing applications. It should be noted that this tailored orientation along the [111] axis is ideal for quantum information and sensing applications, since it maximizes the collection efficiency of NV defect emission in bulk (111) and (113) single-crystal samples in comparison to (100) one and provide a well-defined geometry with an electronic spin pointing in a direction of normal to the diamond sample surface.

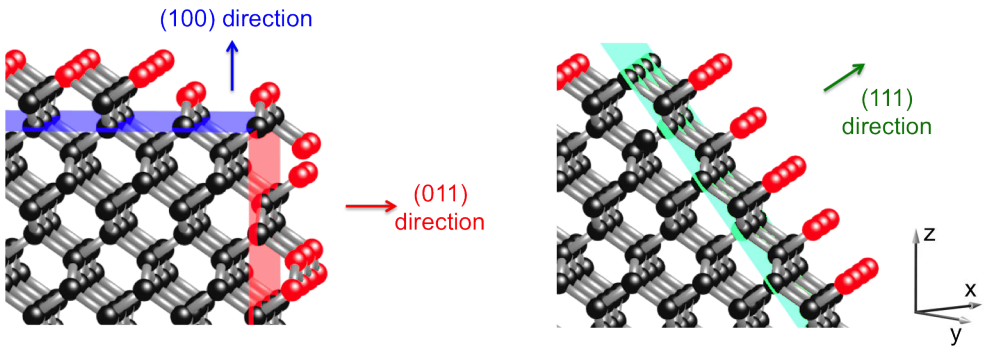

Figure 5.2: Diamond crystal model showing a (100)-oriented surface (blue horizontal plane), (011)-oriented surface (denoted with red vertical plane) and (111)-oriented surface (inclined greed plane). Black and red balls representing carbon and hydrogen atoms respectively.

5.2 111-oriented diamond

5.2.1 Experimental results

The sample used in this experiment was provided by the Diamond group at LSPM laboratory (CNRS and Université Paris-13, Villetaneuse), who succeeded in growing a single-crystal (111)-oriented diamond layer (appendix C). In this work was used homoepitaxial PACVD technique of the diamond deposition on a (111)-oriented HPHT substrate in the condition of a plasma with of high power densities. Finally, based on the fact that the twinning could be avoided, if the growth rate would be faster than rate of the twinned plane. The sample grown in these conditions had thickness of 50 μm shown on the Figure 5.3. As it can be seen from the presented microscope image of the sample, its surface is rather smooth and untwined, moreover it varies all over the sample. The measured root-mean-square (rms) roughness is around 150 nm over a 50×50 μm^2 area. The upper side with the smallest roughness was chosen for further characterization of the sample.

It should be however noted that the crystalline quality of such CVD films remains fairly lower than that the one of conventional (100) CVD films [107] due to the occurrence of stress and extended defects which lead to the intense blue fluorescence observed under UV light excitation (see inset in Figure 5.3 (a)). Although no particular shift of the Raman line was evidenced within the accuracy of the instrument, the width of the line was as high as 2.2 cm^{-1}, when typical values below 1.7 cm^{-1} are usually obtained for the CVD growth on a (100) substrates.

NV defects were optically isolated in this (111)-oriented diamond sample by using a scanning confocal microscope (see appendix A). A typical PL raster scan of the sample is shown in Figure 5.3 (b), showing intense diffraction-limited spots which correspond to single NV defects. This was verified through electron spin resonance (ESR) spectroscopy [24]. In order to resolve the hyperfine splitting a static magnetic

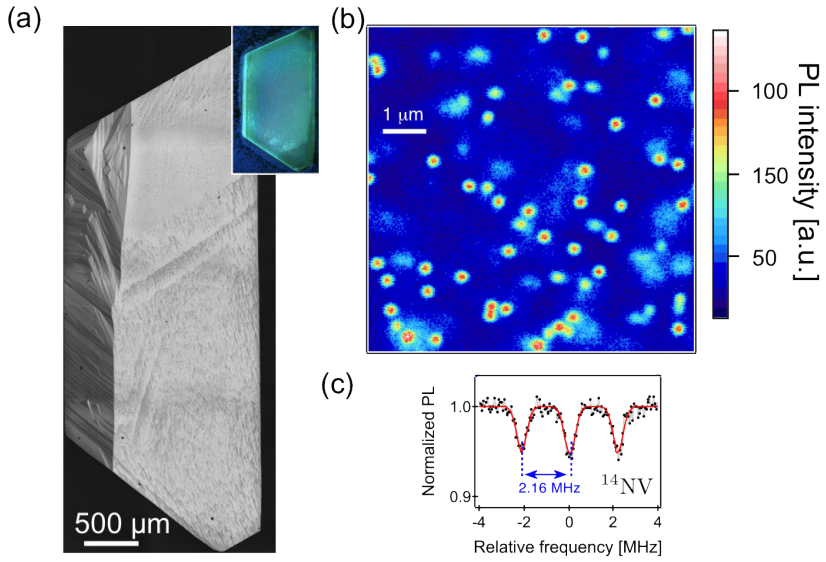

Figure 5.3: (a) Microscope image of the diamond layer grown on a (111)-oriented HPHT substrate. The inset indicates the sample luminescence recorded under ultraviolet light excitation with a DiamondView^{TM} equipment, where intense blue luminescence evidences presented stress and defects of the crystal. (b) PL raster scan of the sample recorded with a scanning-confocal microscope under green laser excitation. (c) ESR spectrum measured for a single NV defect on one of the ESR lines, by recording the PL intensity while sweeping the frequency of a MW field in the presence of a static magnetic field B ≈ 5 G. ESR line reveals the hyperfine structure associated with the ^{14}N nucleus of the NV defect, giving direct evidence for the high purity of the crystal.

field was applied to split $m_s = +1$ and $m_s = -1$ spin sub-levels, where m_s indicates the spin projection along the NV defect quantization axis [108]. A typical ESR spectrum recorded from a PL spot is shown in Figure 5.3 (c), revealing the characteristic hyperfine structure associated to the ^{14}N nuclear spin.

5.2.1.1 Discrimination of the NV center orientation using ESR

The orientation of the created NV centers can be determined by several means, for instance, by recording an ESR spectra while applying a static magnetic field B_0 along one of the four possible orientations in the lattice. In this case differently oriented NV will exhibit the ESR resonances according to the following equation:

$$\nu_{\pm} = D \pm g\mu \mid B_{NV} \mid \tag{5.1}$$

where $g\mu B \approx 2.8$ MHz/G and $\mid B_{NV} \mid$ is the projection of the axis of applied magnetic field to the NV defect quantization axis. In the present experiment the magnetic field was oriented along the [111] crystallographic axis, and this means that for [111]-oriented NV defects $\mid B_{NV} \mid = B_0$, while for the three other orientations this value will be smaller according to

$$\mid B_{NV} \mid = B_0 \cdot \cos\alpha \tag{5.2}$$

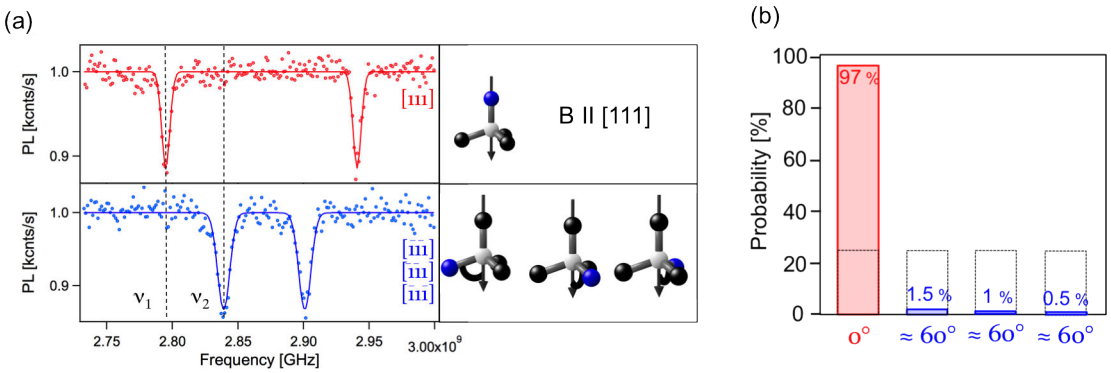

Figure 5.4: (a) Orientation-dependent ESR spectra recorded from single NV defects, while applying a static magnetic field $B_0 = 26$ G along the [111] crystal axis. (b) Histogram demonstrating the distribution of NV defect orientations extracted from ESR measurements for a set of 206 single NV defects. The black dotted bars indicate the expected distribution for randomly oriented NV defects.

where $\alpha = 109.5°$. Typical ESR spectra recorded for a [111]-oriented NV defect and for one of the three other orientations are shown in Figure 5.4, revealing the expected orientation-dependent Zeeman shift of the NV defect electron spin sub-levels. In order to estimate the relative population of each NV defect orientation, ESR spectra were recorded for a set of ≈ 200 single NV defects dispersed inside the layer.

Supposing random orientation the probability to obtain a single center oriented along the [111] axis would be equal to 25 %. However we observe [111]-oriented NV defects with a probability of 97 % (Figure 5.4 (b)). This result reveals an almost ideal preferential orientation of the NV defects created during the growth of the (111)-oriented single crystal layer.

Preferential orientation studies could be checked as well by encoding the NV defect orientation into the PL signal while scanning the diamond sample. In order to achieve this complementary diagnostic, two fixed microwave (MW) frequencies ν_1 and ν_2 were consecutively applied at each point of the scan. Then calculating the difference of NV defect PL intensity $\mathcal{D} = \mathrm{PL}(\nu_2) - \mathrm{PL}(\nu_1)$ a PL map could be obtained.

As depicted in Figure 5.4, the MW frequency ν_1 is set on resonance with the electron spin transition linked to a [111]-oriented NV defect while ν_2 is resonant for NV defects with $\{[1\bar{1}\bar{1}], [\bar{1}\bar{1}1], [\bar{1}1\bar{1}]\}$ orientations. In that case, the recorded signal $\mathcal{D}$ is positive for [111]-oriented NV defects and negative for all the three other possible orientations. A PL raster scan of the sample recorded with this dual-MW frequency method is shown in Figure 5.5. This result confirms the almost perfect degree of the preferential orientation of the created NV defects.

However it should be noted that despite easiness of this two-MW frequencies application scanning-method, this result does not allow us to ensurely distinguish between the NV centers' orientation. Mainly it is caused by the type of the sample used in the experiment, which contain ^{13}C impurities in the host lattice with natural abundance. As can be seen from Figure 5.5 (b) in the case of resonance lines of (111)-oriented NV

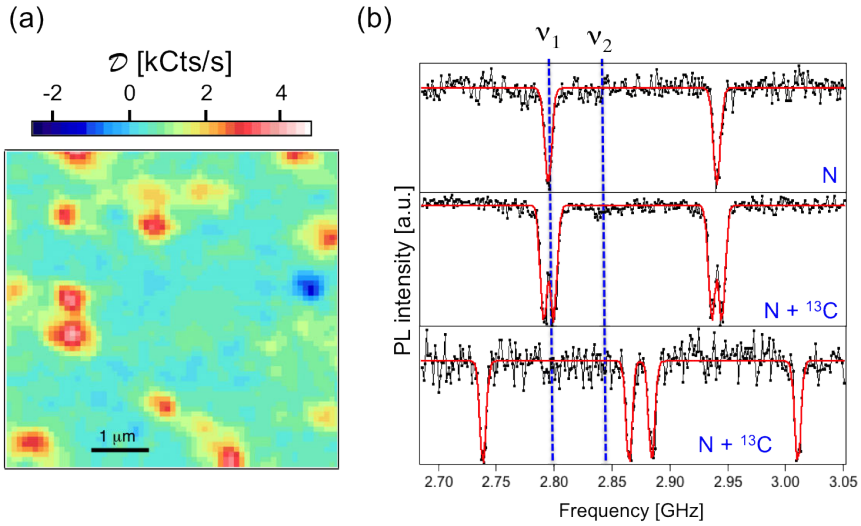

Figure 5.5: (a) PL raster scan of the diamond sample recorded by applying consecutively two fixed microwave frequencies ν_1 and ν_2 as shown in Figure 5.4, while monitoring the difference of NV defect PL intensity $\mathcal{D}$. This signal is positive (red spots) for [111]-oriented NV defects and negative (blue spots) for NV defects with $\{[1\bar{1}\bar{1}], [\bar{1}\bar{1}1], [\bar{1}1\bar{1}]\}$ orientations. (b) ESR spectra recorded on several NV centers coupled to ^{13}C

center the red point appears on the scan, if the NV center is coupled to a neighboring ^{13}C nuclear spin causing a $\approx$ 10 MHz splitting this will produce on a raster scan a red spot with a lower intensity. Finally if a ^{13}C nuclear spin is located in the first coordination shell it will induce a splitting of 130 MHz [109]. As can be seen from the lower graph, such structure will not affect the final scan image, since the difference of the PL signals will then be equal to zero. Therefore an additional discrimination method is required to unambiguously determine the NV center orientation.

5.2.1.2 Orientation discrimination based on polarization-dependent PL

The NV defect orientation can also be determined by recording the PL intensity while rotating the polarization of the excitation laser [110]. The NV center possesses two mutually orthogonal dipoles, which are lying in the plane perpendicular to the NV center axis [83].

The effective excitation rate of the NV defect is then linked to the projection of these dipoles along the linearly-polarized laser field, *i.e.* in the diamond sample surface plane. For [111]-oriented NV defects, the two orthogonal dipoles are equally excited in geometry of the optical microscope (see appendix A), and the PL intensity does not depend on the laser polarization angle. Conversely, for NV defects with $\{[1\bar{1}\bar{1}], [\bar{1}\bar{1}1], [\bar{1}1\bar{1}]\}$ orientations, the unbalanced excitation of the two dipoles leads to a polarization-dependent PL intensity, as shown in Figure 5.6 (b). This complementary method enables us to distinguish between all four possible NV defect orientations [110].

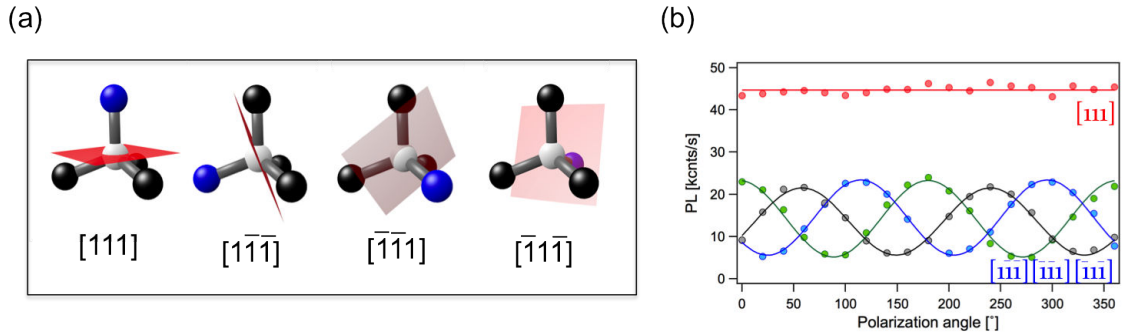

Figure 5.6: (a) Schematic representation of the four possible orientations of NV defects in a (111)-oriented diamond sample with the plane orthogonal to the NV axis containing the two orthogonal absorbtion dipoles. (b) Polarization-dependent PL intensity for single NV defects with different crystal orientations. These measurements were performed at weak laser excitation power (P = 15 µW) in order to avoid saturation effects of the optical transition.

5.2.1.3 PL collection efficiency

We finally note that the PL signal from a [111]-oriented NV is always higher, even at saturation of the optical transition, since the collection efficiency is also maximized for this specific orientation (see Figure 5.7) in the geometry of the optical excitation and collection of PL signal. This is a further advantage for quantum information and sensing applications since non-ideal collection efficiency will limit the sensitivity.

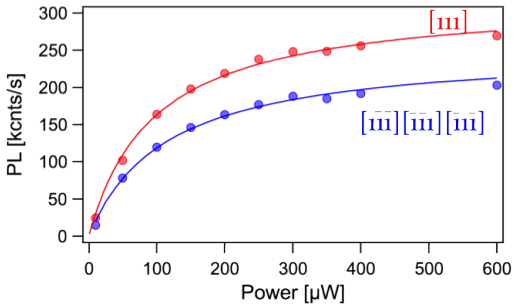

Figure 5.7: Collected PL intensity as a function of the excitation laser power for single NV along the four possible orientations in the lattice.

5.2.1.4 The mechanism of the preferential orientation

In order to qualitatively explain the observed preferential orientation, we adapt the growth mechanism proposed by Edmonds et al. [78] for the (110) surface. For that purpose, it is useful to represent a clean, perfectly oriented (111) surface in a CVD environment (Figure 5.8 (a)).

A (111)-oriented surface exhibits only one hydrogen-saturated bond pointing towards the [111] direction whereas a (110) surface would have two of them as shown on Figure 1.14. It was demonstrated that diamond growth on a flat (111) surface first

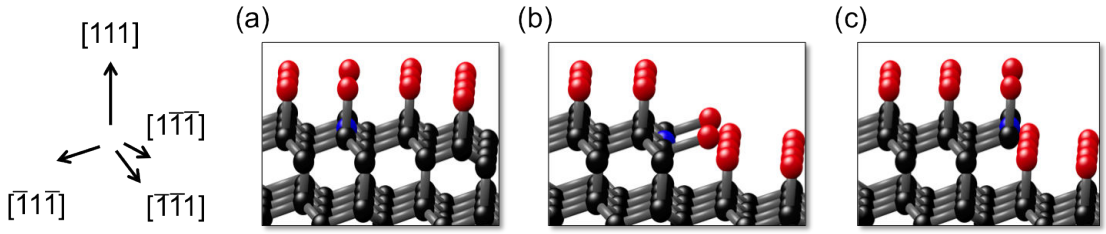

Figure 5.8: Crystal model showing (a) a clean (111)-oriented surface and a surface step requiring the addition of 2 carbons (b) or 1 carbon (c) for the growth to continue. Carbon, hydrogen, and nitrogen atoms are symbolized by grey, red and blue balls, respectively.

requires the formation of a new nucleation island created by abstraction of hydrogen and bonding of a cluster of 3 carbon atoms [111, 112]. This process limits the growth rate since it takes a relatively long time to occur. On the other hand, once a step of atoms is placed on the surface, then the layer completes very quickly by the addition of two carbon atoms (Figure 5.8(b)) or even only a single carbon atom (Figure 5.8(c)) until its full construction.

From this qualitative picture, it appears that if a N atom is incorporated at a step edge during the step-flow growth, it is unlikely that it will be directly followed by a vacancy since steps are very attractive for CH_3 radicals in the plasma environment. In other words it is favorable that the N atom is fully bonded to the surface in a threefold coordination, as illustrated in Figure 5.8 (a). On the other hand, when the surface is overgrown by the next layer, it will occasionally leave a vacancy above the N atom, which is favored by the fact that it has no available bonding electron to attract another carbon atom. Although this simple picture of the atomic layer growth mechanism provides insights into the preferential orientation of NV defects, it would be interesting to conduct atomistic modeling in order to evaluate the energy of the different configurations of the N atom during the (111)-oriented CVD growth [113]. Nevertheless, we note that the reported preferential orientation confirms that a native NV defect is grown in as a single unit rather then by first adsorption of a nitrogen impurity followed by diffusion of vacancies through the lattice, which then recombine with the nitrogen atom [78].

This experiment has been later on confirmed by some other research groups. For instance, simultaneously appeared article of J.Michl et al., has demonstrated the probability of 94% that NV center aligns along [111] crystallographic direction [114]. Moreover within all the centers aligned perpendicularly to the diamond surface they performed an additional experiment based on ac-electrometry to establish wether the centers were formed with N atom looking up or down. Finally they found that 74% of [111] oriented NV centers are formed with nitrogen incorporation and then it is followed by vacancy. Fukui et al. has reported a 99% fidelity of the preferential orientation formation while [111]-oriented diamond layer growth, moreover they found that it can be

explained by the energetically advantageous organization of the structure [115].

5.2.1.5 Measurement of the spin coherence properties

Since (111)-oriented CVD growth is known to favor the incorporation of different kind of impurities and defects [116], we now investigate the coherence properties of electron spin of single NV defects and compare the result to reference values obtained in high-purity single crystal samples grown with PACVD on a conventional (100)-oriented substrate. Typical Ramsey signal and spin-echo measurement recorded from a single NV defect are depicted in Figure 5.9 in the presence of the static magnetic field of applied along the axis of the observed NV center [106].

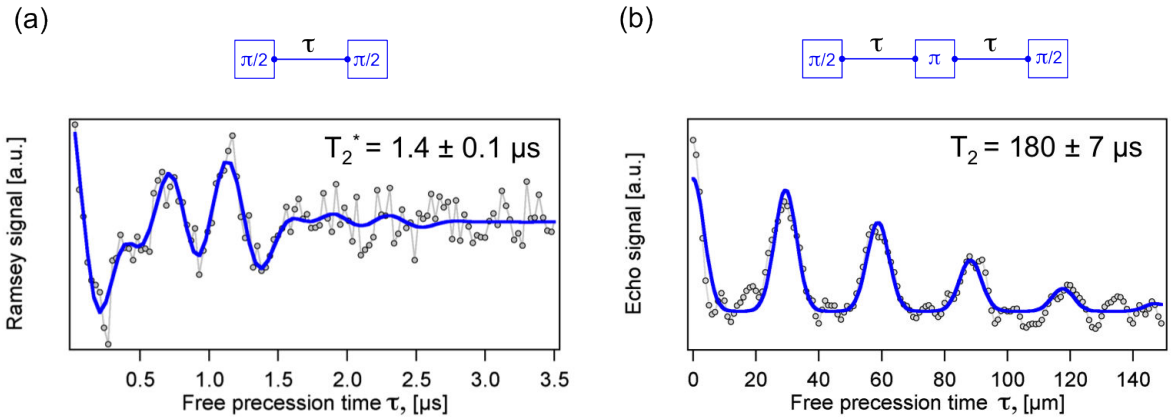

Figure 5.9: Typical (a) Ramsey signal and (b) spin echo signal recorded from a single NV defect in a (111)-oriented CVD grown layer, which indicates a coherence time T_2^* = 1.4 ± 0.1 μs and T_2 = 180 ± 7 μs . A static magnetic field B_0 = 31 G is applied along the [111] axis. Similar results were obtained by investigating a set of 10 randomly chosen NV defects.

The envelope of the spin echo signal indicates a coherence time T_2 = 180 ± 7 μs. This value is similar to those obtained for single NV defects hosted in a high purity (100)-oriented layer with the same natural abundance of ^{13}C (1.1%) . This result shows that the incorporation of impurities and defects that might occur during the growth on the (111)-oriented substrate does not impair the coherence time of single NV defects. We note that the spin coherence time could be further improved either by applying advanced dynamical decoupling protocols or by using methane isotopically enriched with ^{12}C in the CVD reactor [46].

5.3 113-oriented diamond

5.3.1 113 growth

These results devoted to control of the NV center orientation using (111)-growth are promising. However, as it was already pointed out the crystalline diamond quality

remains fairly lower in comparison to the conventional (100)-growth, due to higher number of incorporated impurities and higher strain parameter. Moreover it becomes even harder to reach good quality diamond for the thicknesses of the grown layers more than 10 μm.

It should be noted that in order to grow (111)-oriented layer the substrate should be prepared from a (100)-grown diamond. Since the angle between the planes is rather big (45°, as can be seen from Figure 5.10) this requires the thickness of the initial sample to be big as well.

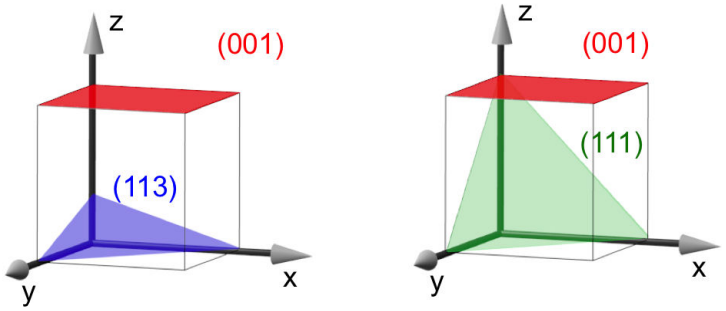

Figure 5.10: Location of (a) (111) and (b) (113) crystal planes relatively to (001) plane

An alternative to the (111)-oriented layer is the (113)-oriented diamond growth. As it is shown on Figure 5.10 the angle between (113) and (111) planes is only around 25° to the normal direction of the surface of the sample. This feature simplifies significantly the preparation of the substrate for the further PACVD growth.

According to previous results it could be expected a preferential orientation along [111]-crystallographic direction which forms a 30° angle with the normal direction to the (113) plane. The NV centers oriented along $[\bar{1}\bar{1}1]$ are expected to be presented with a small probability, since this orientation forms a 80° angle with the normal to the

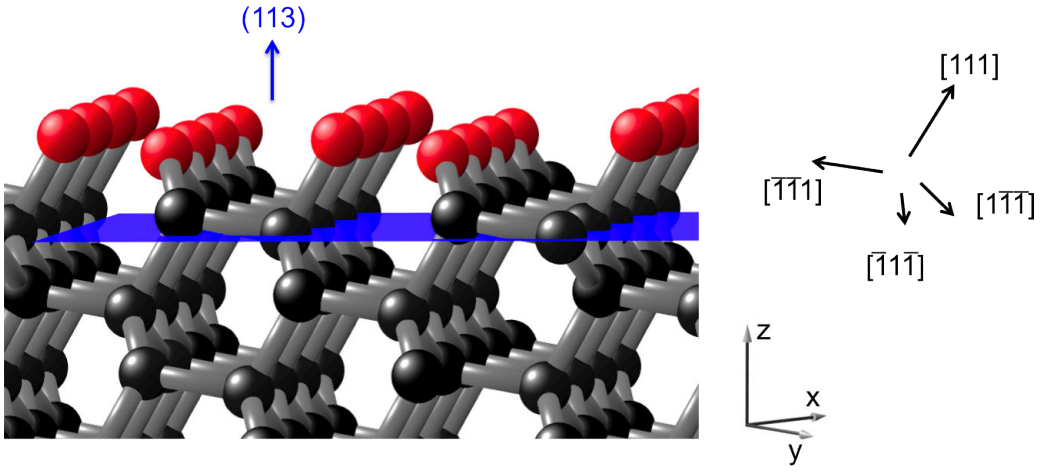

Figure 5.11: Hydrogen-terminated 113-oriented diamond layer and associated crystal axis.

sample surface making it lying almost perfectly in the plane. Two other crystallographic orientations $[\bar{1}1\bar{1}]$ and $[1\bar{1}\bar{1}]$ which are forming relatively similar angles (around 60°) with the normal direction should be presented with almost equal probability (see Figure 5.11).

5.3.2 Experimental results

The sample used in the present experiment was provided as well by the LSPM Diamond group, who deposited a PACVD layer with 460 μm thickness on the prepared (113)-oriented substrate (appendix C). The growth rate was estimated to be in the range 16 μm/h without any intentional N_2 insertion. The surface morphology is rather smooth and flat, as can be seen from Figure 5.12 (a).

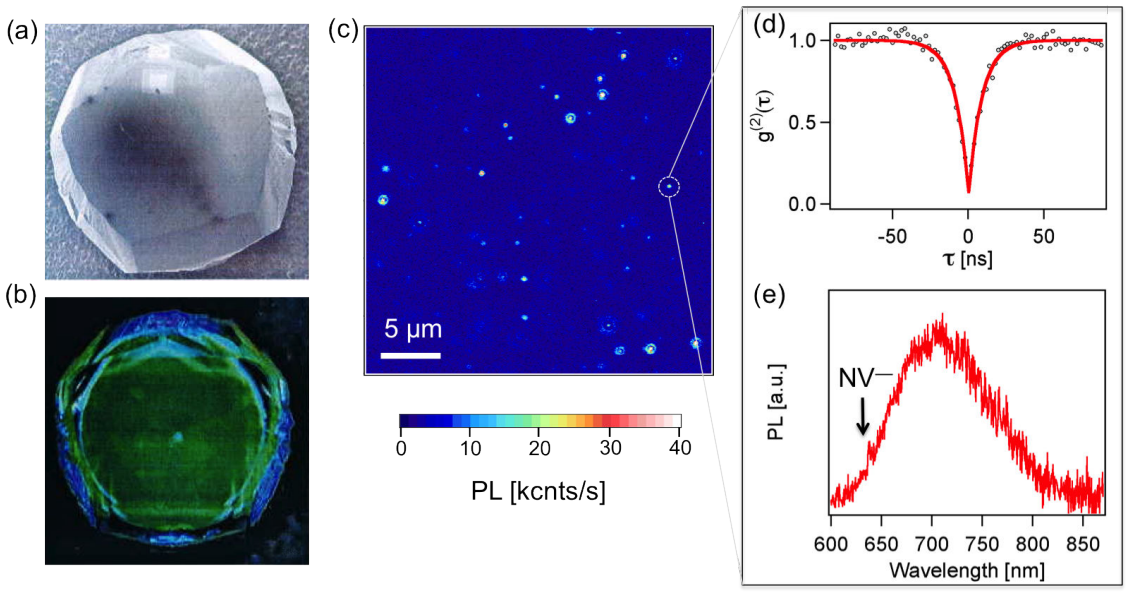

Figure 5.12: (a) Microscope image of the (113)-oriented diamond sample consisting of a 460 μm deposited CVD layer. (b) Image of the sample obtained using ultraviolet light excitation with a DiamondViewTM equipment. (c) Typical PL scan of the sample, where the bright spots correspond to the emission of single NV centers. A typical photon correlation measurement (d) and PL spectrum (e) associated to one emission spot.

The quality of the grown substate was first estimated with the Diamond-View^{TM} technique. The microscope image of the sample under UV light excitation displays some blue fluorescence on the edges of the substrate (Figure 5.12 (b)), while exhibiting much less strain compared to previous experiment with a (111)-oriented sample. These observations allow us already to conclude that the estimated crystalline quality of (113)-substates will be improved. Figure 5.12 (c) shows a typical PL raster scan image of the grown layer. Characterization performed on several luminescent spots prove that they are single emitters as can be seen from Figure 5.12 (d). Moreover, spectral

measurements indicate that the layer contains mainly negatively charged NV centers, as shown on Figure 5.12 (e).

5.3.2.1 Orientation discrimination using ESR

The NV center orientation discrimination was performed by applying identical methods as for the characterization of the (111)-oriented sample. An external magnetic field was applied in the perpendicular direction to the surface and the PL response of the NV centers was recorded while sweeping MW frequencies. The orientation dependent Zeeman shifts of the electron spin sub-levels then define possible ESR spectra for the given applied magnetic field.

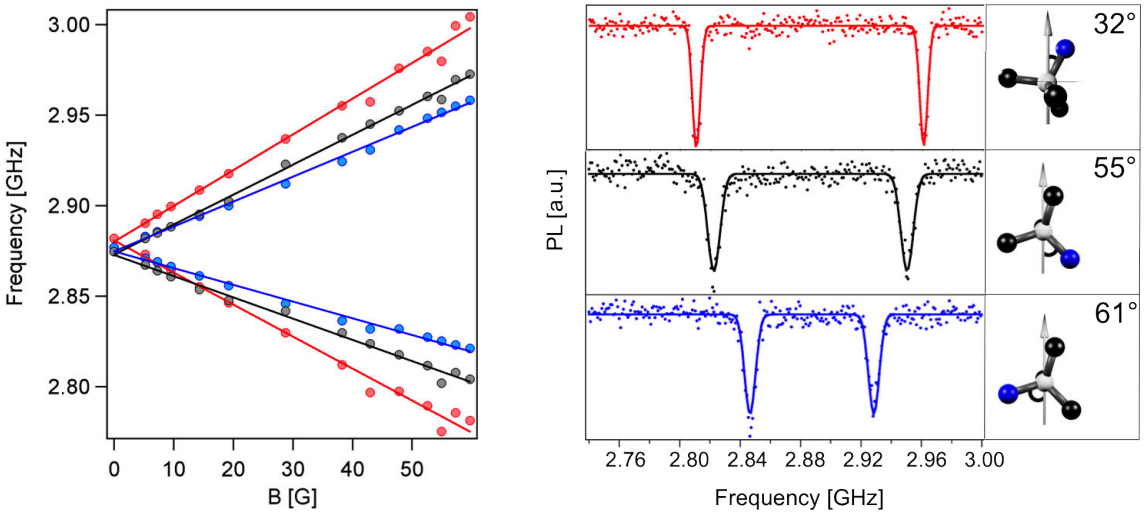

Figure 5.13: (a) Orientation-dependent Zeeman splitting recorded from three single NV defects, while applying a magnetic field aligned perpendicular to the surface of varying amplitude. (b) Associated typical ESR signals recorded with B_0- field amplitude of 23 G.

Varying the value of applied magnetic field for three different NVs' orientations were obtained the curves presented on Figure 5.13 (a). Then, by fixing the magnetic field an amplitude of 23 G and recording one ESR spectrum per NV center we could determine its orientation in the crystal. Such measurements were performed for more than 200 NV centers. The statistics reveals that most of them are oriented along the [111] direction. The insets of Figure 5.13 (b) schematically represent three possible NV orientations with associated ESR spectrum.

The real value of the angle between the axis perpendicular to the surface and the NV center axis was experimentally measured using a system consisting of three coils. By changing the B field direction in one plane and detecting the NV center's electronic spin sub-levels splitting it allowed us to find the value of the angle of magnetic field, when the center and the B-field are in the position of best parallel alignment. Then repeating the same experiment for each two other planes gives the space coordinates of the orientation of the NV axis.

It should be noted that in the investigated set of ≈ 200 centers, the other forth orientation forming 80° with the normal direction to the surface in the crystal was never detected.

5.3.2.2 Orientation discrimination using polarization-dependent PL

Again similarly to the previous study, discrimination between the possible orientations of the NV center was studied using polarization-dependent PL signal. The change of the polarization of the excitation beam in the plane of the sample was achieved by rotating a half-wave plate. As already pointed out, the NV center possesses two mutually orthogonal dipoles [83, 110], which are lying in the plane perpendicular to the N-to-V axis. Since we perform measurements at room temperature both dipoles are coupled between them[1] and even if one of them is excited, both dipoles will emit.

For [111]-oriented NV defects, the two orthogonal dipoles not equally polarized as they were for (111)-oriented sample, since N-to-V axis placed with the angle of approximately 30° relatively the axis perpendicular to the sample surface. However this orientation optimizes the PL collection efficiency as shown on Figure 5.14. Instead the two other detected PL signals for the NV axis oriented along the $[1\bar{1}\bar{1}]$ and $[\bar{1}1\bar{1}]$ crystallographic axis correspond to weaker detection rate compared to [111]-orientation, even at their maximum[2].

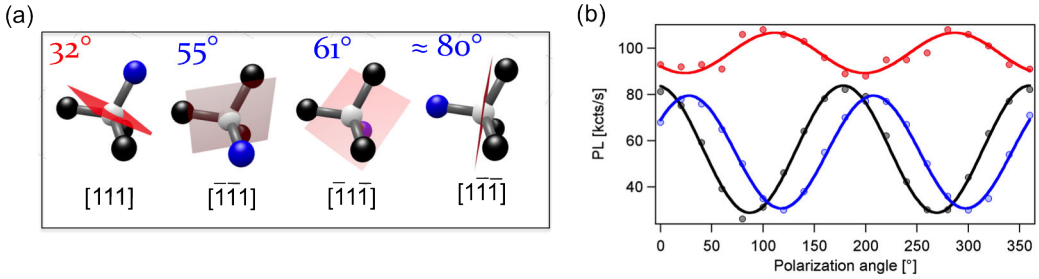

Figure 5.14: (a) Schematic representation of the four possible orientations of NV defects in a (113)-oriented diamond sample and the plane containing the two orthogonal dipoles. (b) Polarization-dependent PL intensity for single NV defects with the different crystal orientations previously analyzed. These measurements were performed at weak laser excitation power (P = 50 μW) which avoids saturation effects of the optical transition.

This method allows to distinguish between the three orientations which were detected in the (113)-oriented sample. However NV centers created along $[1\bar{1}\bar{1}]$ and $[\bar{1}1\bar{1}]$ are close to each other, since they form relatively similar angles with the normal incidence to the surface and almost 180° shift between the corresponding emitting dipole in the plane of the sample surface.

[1]Low-temperature measurements allow selective dipole excitation [117]

[2]It should be noted that the confocal setup has been slightly changed, therefore impossible to compare the PL detection efficiency for the NV centers formed in (111) and (113) samples

5.3.2.3 PL collection efficiency

The saturation curves recorded for the three possible orientations previously described demonstrate that NV centers aligned along the [111] crystallographic axis are characterized with the higher intensities of the detected PL. Even a slight difference of several degrees between the N-to-V axis center axis and the normal incidence to the sample leads to a decrease of saturation signal of more than 10 kcounts/s. Measured data are consistent with the previously reported concerning the significance of the angle of the emittance for the standard NV centers measurement setup, corresponding to an optical axis for excitation and collection perpendicular to the sample surface.

Collection efficiency depends as well on the depth of the NV center placement, or more precisely from the distance of the NV center till the air/diamond or oil/diamond interface. Therefore it should be noted that in the experiments of polarization dependent PL signal and saturation of the emittance, all curves were recorded for NV centers placed on approximately one plane parallel to the surface.

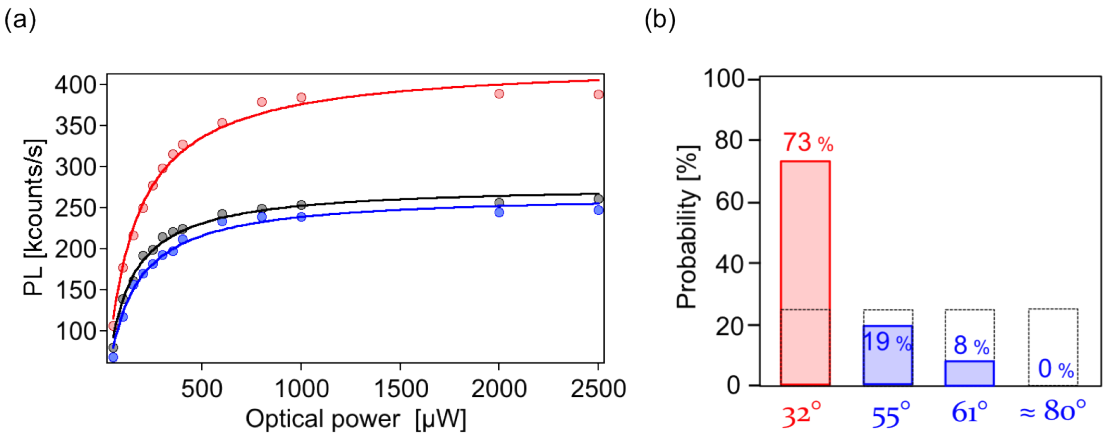

Figure 5.15: Detected PL intensity as a function of the laser power, recorded for the three possible orientations of a single NV center observed in the sample.

Summarizing all the orientation discrimination experiments in the (113)-oriented sample we conclude that 73% of them are formed along the [111] crystallographic axis (see Figure 5.15 (b)).

5.3.2.4 Coherence properties' measurements

As in the previous experiment for the spin coherence time measurement, two sequences were used: the Ramsey signal sequence and the Hahn-echo sequence [106]. The typical signals recorded from a single NV defect are shown in Figure 5.16. The measured T_2^* value is in the range of 1.9 μs.

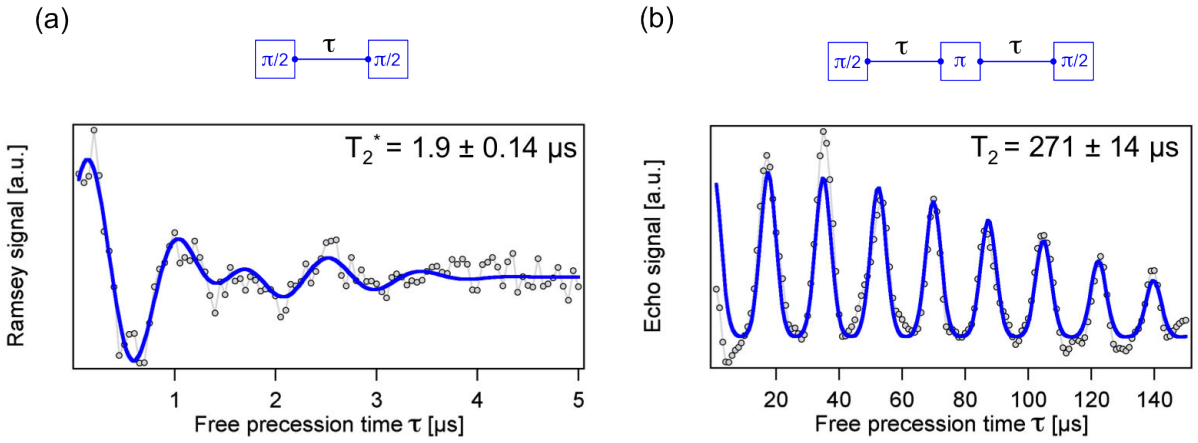

Figure 5.16: Spin coherence signals recorded for a [111]-oriented NV center with a static magnetic field set to 53 G and applied along the [111] crystallographic axis. The solid line is a fit with the sum of Gaussian peaks modulated by a decay envelope, as explained in the Ref. [106].

The envelope of the spin echo signal indicates a coherence time $T_2 = 271 \pm 7$ μs. As in the case of the (111)-oriented sample, these values are similar to the one obtained for single NV defects hosted in high purity (100)-oriented diamond samples with the same natural abundance of ^{13}C (1.1%). We conclude from this results that the defects incorporation while diamond growth in the (113) direction as well does not worsen the coherence properties of the native centers which appear during the growth.

5.3.2.5 Doping of (113)-oriented sample

The control of the NV center orientation is useful for implementing the wide-field magnetic sensing technique [118],[38]. An attractive way to realize a sensitive device is to use a magnetic response of a thin layer of oriented NV centers in a doped diamond. For that purpose another (113)-oriented sample was prepared in order to increase the number of the NV centers created during the growth of the layer on the top of a (113)-oriented substrate by adding nitrogen gas in the plasma chamber.

The (113)-grown sample was provided by Diamond group at LSPM laboratory with the final thickness of 760 μm. The growth rate was approximately 30 μm/h. During the deposition process a content of 0,5 ppm N_2 gas was first introduced and finally 10 ppm N_2 gas was added during the last 30 minutes of growth. It should be noted that the sample surface had a relatively smooth morphology. Using the confocal setup for characterization it was impossible to resolve single NV centers, whereas the ESR analysis showed the presence of 2.87 GHz resonance line, which corresponds to the zero-field splitting of the ensemble of negatively-charged NV centers. By adding a static magnetic field we could then resolve three pairs of Zeeman splitted lines, corresponding to the three orientations previously observed (Figure 5.15 (b)).

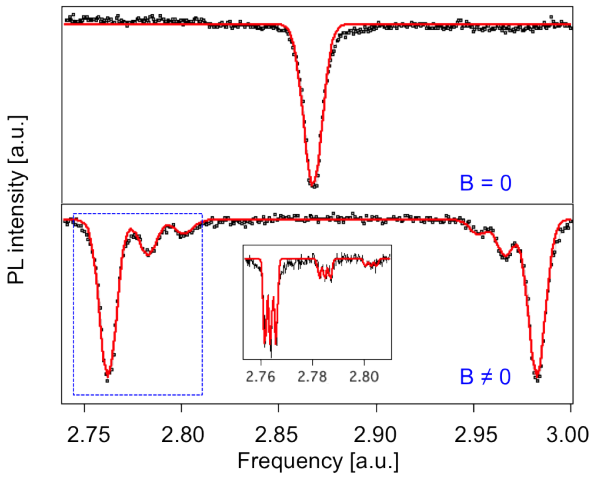

Figure 5.17: ESR spectra recorded from an ensemble of NV centers while sweeping the frequency of the applied microwave field. Upper graph demonstrates zero-field resonance in the absence of magnetic field. The lower graph, is taken at the same confocal spot in the sample in presence of static magnetic field B ≈ 30 G. A high resolution zoom inside the resonance lines reveals the hyperfine structure created by the coupling with the ^{14}N nucleus of NV defects.

5.4 Conclusion and perspectives

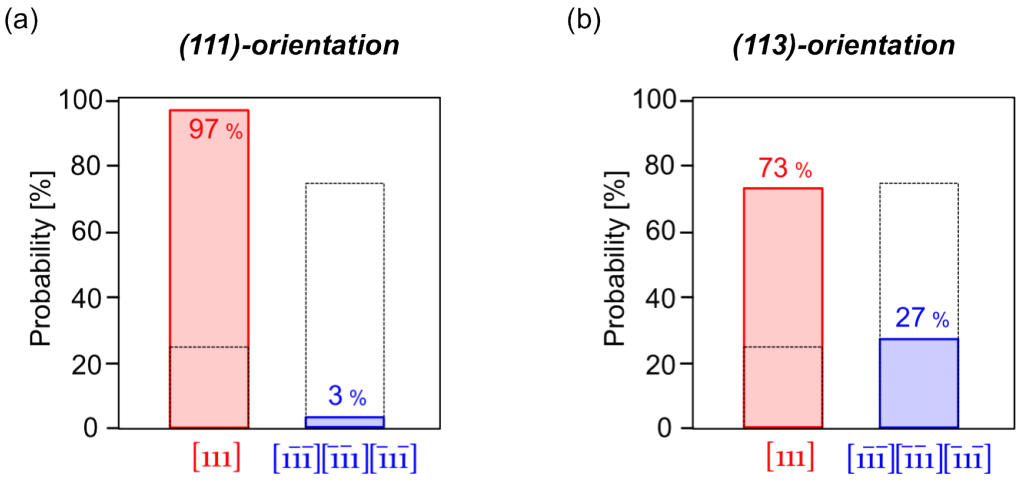

Figure 5.18: Statistics of the NV defect orientations extracted from ESR measurements and polarization-dependent PL intensity. The data correspond to a set of more than 200 single NV defects, in the case of (111)-oriented or (113)-oriented substrates. The black dotted bars shows the expected distribution for random NV defects orientation.

In summary, an almost perfect orientation of NV defects in the [111] direction was achieved by the CVD growth on a (111)-oriented substrate and preferential orientation was also achieved in (113)-oriented sample. These results, together with an increased photon collection efficiency and long spin coherence times, paves the way towards high sensitivity magnetometry with either single or ensemble of NV defects [119, 37,

120, 121] and also the optimization of the coupling with superconducting qubits in hybrid quantum systems [122, 123]. Furthermore, the orientation also optimizes the coupling to photonic waveguide or cavities, since the emitting optical dipoles are then lying in the diamond surface [124, 67, 125]. This work, which could be extended to other defects in diamond [78] or silicon carbide materials [126], therefore provides a significant step towards the design of optimized samples for quantum information and sensing applications.

Due to the Zeeman effect on the electron spin structure, we were able to determine the orientation of NV centers which spontaneously arose during CVD growth, by measuring an applied magnetic field along the N-to-V axis. By using a magnetic field oriented perpendicular to the surface and then measuring the set of electron-spin resonances we could discriminate between the four possible orientations in the diamond lattice. These possible NV orientations can also be distinguished by recording the PL intensity depending on the polarization of the excitation laser, as shown on Figure 5.6 (b). In the case of [111]-oriented centers this specific orientation leads to an optimal collection efficiency with the emitting dipoles perpendicular to the axis of the optical collection system. Using these complementary diagnostics, we found that for the [111]-oriented layer nearly all of centers had their axis along the [111] crystallographic orientation, and only 6 centers out of 206 showed three other possible orientations (Figure 5.18(a)). This result can be understood from the growth mechanism of the diamond layer.

Preferential orientation was also observed for the (113)-growth (Figure 5.18(b)). Despite less pronounced effect of the [111]-crystallographic orientation preference in a (113)-oriented substrate, compared to the (111) case, it has some other important advantages. For example, as it was already noted the growth in (113) direction leads an improved quality of the diamond layer with a smooth surface, and less strain inside the diamond lattice. Moreover such crystals can be grown faster and thicker, and in general the growth conditions in (113) direction has a wider range of flexibility. Doping of nitrogen at high content can be easier achieved, since less perturbation is added to the growth procedure compared to the (111) case.

CHAPTER 6

NV center spin coherence manipulation

6.1 Introduction

Most applications of the NV center benefit from the optimization of the spin coherence properties, which are mainly limited by the noise due to the fluctuations of the magnetic field created by paramagnetic impurities in the lattice, such as the nuclear spin $I = 1$ of nitrogen ^{14}N or the nuclear spins $I = 1/2$ of the nitrogen ^{15}N and carbon ^{13}C nucleus [42, 127]. In the context of nuclear magnetic resonance, different techniques have been developed in order to decouple an ensemble of spins from a fluctuating magnetic field. It goes from the Hahn echo sequence, which "refocuses" the spin ensemble to the state it would be in the absence of magnetic perturbations [128], to sophisticated dynamical decoupling sequences such as the CPMG protocol [129] which has been adapted to the NV center [130]. As introduced in §1.4 another approach is to remove the parasitic spins through the control of material by using ultrapure diamond samples with a nitrogen concentration down to the ppb level and by growing isotopically pure diamond consisting only of ^{12}C which has no nuclear spin [46].

In this Chapter, we will introduce another strategy consisting in a scheme where the NV center spin is in a quantum stage which is intrinsically protected against fluctuations of the magnetic field. We will start in §6.2 with the description of the NV center spin Hamiltonian. Then in §6.3 we will report the experimental results of the coherence time evolution for "deep" NV centers when submitted to strain. Finally, in §6.4 we will consider the T_2^* time for a shallow NV center either in a diamond crystal or inside a nanodiamond.

6.2 Ground-state spin Hamiltonian of the NV defect

The ground-state spin Hamiltonian of the NV defect is given by:

$$\mathcal{H}_{NV} = \mathcal{H}_{ZFS} + \mathcal{H}_B + \mathcal{H}_H, \tag{6.1}$$

where $\mathcal{H}_{ZFS}$ includes the zero-field splitting parameters describing the ground state interaction, $\mathcal{H}_B$ is the Zeeman term induced by the interaction with a static external magnetic field, and $\mathcal{H}_H$ describes the hyperfine interaction with nearby nuclear spins in the diamond lattice.

6.2.1 Zero-field splitting Hamiltonian $\mathcal{H}_{ZFS}$

The zero-field splitting Hamiltonian of the NV defect can be written as

$$\mathcal{H}_{ZFS} = hD\hat{S}_z^2 + hE\left(\hat{S}_x^2 - \hat{S}_y^2\right), \tag{6.2}$$

where z is the NV defect quantization axis corresponding to the direction between the nitrogen impurity and the bonded vacancy (see Figure 1.1), h is the Planck constant, D and E are the zero-field splitting parameters, and $(\hat{S}_x, \hat{S}_y, \hat{S}_z)$ are the components of the spin operator associated to the electron spin $S = 1$. The axial zero-field splitting parameter $D \approx 2.87$ GHz results from spin-spin interaction between the two unpaired electrons of the defect. The off-axis zero-field splitting parameter E results from local strain in the diamond matrix which lowers the C_{3v} symmetry of the NV defect. The E parameter therefore strongly depends on the diamond sample which hosts the NV defect. In high purity CVD-grown diamond samples it has a typical value $E \approx 100$ kHz [70], while in nanodiamonds, where local strain is much stronger, E can reach few MHz [131]. Note that however the regime $E \ll D$ is always fulfilled.

The eigenstates of $\mathcal{H}_{ZFS}$ are given by:

$$|0\rangle = |m_s = 0\rangle \ , \tag{6.3}$$

$$|+\rangle = \frac{1}{\sqrt{2}}\left[|m_s = +1\rangle + |m_s = -1\rangle\right] \ , \tag{6.4}$$

$$|-\rangle = \frac{1}{\sqrt{2}}\left[|m_s = +1\rangle - |m_s = -1\rangle\right] \ . \tag{6.5}$$

Interestingly, the $|+\rangle$ and $|-\rangle$ eigenstates are insensitive to first-order magnetic field fluctuations, since $\left\langle \pm|\hat{S}_z|\pm \right\rangle = 0$.

The central idea is then to achieve an experimental configuration for which $\mathcal{H}_B + \mathcal{H}_H = 0$ in Eq. 6.1, *i.e.* $\mathcal{H}_{NV} = \mathcal{H}_{ZFS}$. Then, the NV defect electronic spin becomes protected against decoherence processes which would be induced by the fluctuations of the magnetic field created on the NV center by the paramagnetic impurities in the diamond lattice [70]. This configuration is then appropriate to investigate the influence of other sources of decoherence, such as the electric field noise which through the Stark effect, is equivalent to fluctuations of the E parameter.

6.2.2 Zeeman interaction

When a static external magnetic field **B** is applied to the NV defect, the Hamiltonian describing the Zeeman interaction with the NV electron spin is

$$\mathcal{H}_B = g\mu_B \mathbf{B} \cdot \hat{\mathbf{S}}\,, \tag{6.6}$$

where $g \simeq 2.0$ is the Landé g-factor, and μ_B is the Bohr magneton. In the following, we consider a magnetic field amplitude B much smaller than the longitudinal zero-field splitting, so that $g\mu_B B \ll hD$. In that case, the quantization axis remains determined by the NV defect axis z and the influence of the off-axis magnetic field components (B_x, B_y) can then be neglected so that $\mathcal{H}_B \cong g\mu_B B_z \hat{S}_z$.

Neglecting the hyperfine interaction with nearby nuclear spins $\mathcal{H}_H$, the two ESR frequencies $\nu_\pm$ of the NV defect are then given by

$$\nu_\pm(B_z) = D \pm \sqrt{\left(\frac{g\mu_B}{h} B_z\right)^2 + E^2}. \tag{6.7}$$

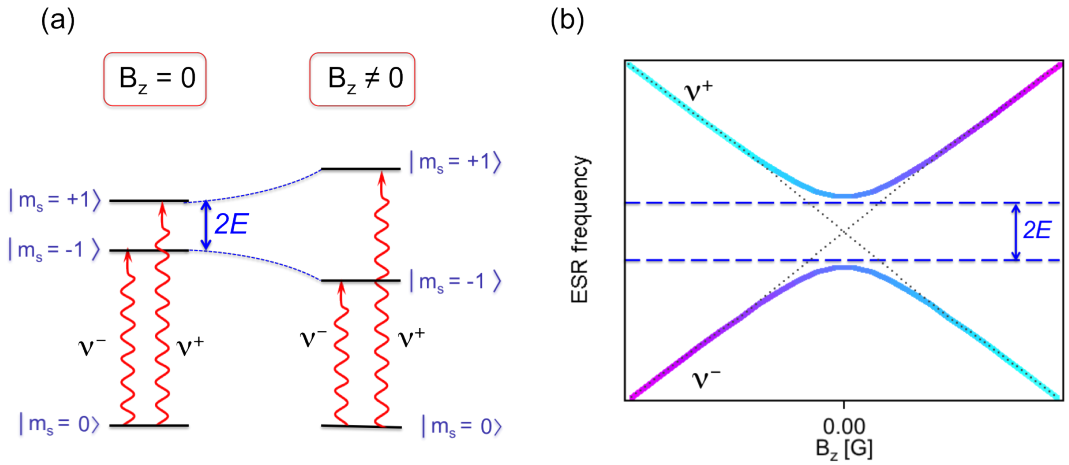

Figure 6.1: (a) NV defect fine structure at (a) applied magnetic field$B_z = 0$ and $B_z \neq 0$. (b) Schematic representation of the shift of the ESR resonance lines as a function of the applied magnetic field along the NV axis.

As shown in Figure 6.1, the ESR frequencies $\nu_\pm$ evolve quadratically with the magnetic field as long as $g\mu_B B_z \sim hE$ with an anti-crossing around the zero field. Around this anti-crossing, $\nu_\pm \approx D \pm E$ with eigenstates $|+\rangle$ and $|-\rangle$ defined by Eq. 6.4 and 6.5, and the NV defect electron spin remains insensitive to any magnetic field fluctuation at first-order.

6.2.3 Hyperfine interaction $\mathcal{H}_H$

We now discuss the part of the Hamiltonian which describes the hyperfine interaction with nearby nuclear spins. In the secular approximation and neglecting the anisotropic part of the hyperfine tensor [10], this coupling can be simplified as

$$\mathcal{H}_H = h\mathcal{A}_{\shortparallel}\hat{I}_z\hat{S}_z \ , \tag{6.8}$$

where $\hat{I}_z$ is the Pauli operator describing the nuclear spin state and $\mathcal{A}_{\shortparallel}$ is the axial component of the hyperfine tensor. The hyperfine interaction can then be considered equivalent to a Zeeman effect induced by an effective magnetic field B_H associated to the hyperfine interaction. The amplitude of this effective field depends on the nuclear spin projection along the NV axis, denoted m_I, and the hyperfine coupling can be written as

$$\mathcal{H}_H = g\mu_B B_H \hat{S}_z \quad \text{with} \quad B_H = \frac{h\mathcal{A}_{\shortparallel}}{g\mu_B} m_I \, . \tag{6.9}$$

We can then use Eq. 6.7 to compute the ESR frequencies $\nu_{\pm,m_I}$ of a single NV defect coupled to a single nuclear spin through this simplified hyperfine interaction:

$$\nu_{\pm,m_I}(B_z) = D \pm \sqrt{\left[\frac{g\mu_B}{h}(B_z + B_H)\right]^2 + E^2} \, . \tag{6.10}$$

Anti-crossings of the ESR frequencies are then observed when $B_z + B_H = 0$, *i.e.* when the hyperfine interaction and the Zeeman interaction with the external magnetic field cancel each other.

Two nuclear spin species commonly interact with the NV defect, namely the intrinsic nitrogen nucleus, of the defect, and the nucleus of a ^{13}C atom which can be found in the lattice with a natural abundance of 1.1%.

The nitrogen atom has two isotopes ^{14}N and ^{15}N. The ^{14}N isotope is found with 99.6% abundance and corresponds to a nuclear spin $I = 1$. The ^{14}N hyperfine tensor has been extensively characterized over the last years [132, 133, 134] and leads to a splitting of $\mathcal{A}_{\shortparallel}^{(^{14}\mathrm{N})} = 2.16$ MHz between ESR frequencies associated with the three different ^{14}N nuclear spin projections[1]. In that case, three anti-crossings of the ESR frequencies can be achieved for $B_z = 0$ and $B_z = \pm h\mathcal{A}_{\shortparallel}^{(^{14}\mathrm{N})}/g\mu_B$, as shown in Figure 6.2 (a). The ^{15}N isotope exists only with 0.4% abundance but can be selectively used for the creation of NV defects using ion implantation [86]. It corresponds to a nuclear spin $I = 1/2$ with an axial hyperfine constant of $\mathcal{A}_{\shortparallel}^{(^{15}\mathrm{N})} = 3.15$ MHz. In that case, only two anti-crossings are achieved for $B_z = \pm h\mathcal{A}_{\shortparallel}^{(^{15}\mathrm{N})}/2 \cdot g\mu_B$ (see Figure 6.2 (b)).

A neighboring lattice site of the NV defect can be randomly occupied by a ^{13}C isotope, corresponding to a nuclear spin $I = 1/2$. The strength of the hyperfine interaction $\mathcal{A}_{\shortparallel}^{(^{13}\mathrm{C})}$ strongly depends on the lattice site occupied by the ^{13}C with respect to the NV defect [135, 109]. As an example, Figure 6.2 (c) shows how the ESR frequencies are evolving as a function of the magnetic field for a single NV defect coupled both to its intrinsic ^{14}N nuclear spin and to a nearby ^{13}C nuclear spin. Here, six anti-crossings can be obtained.

[1]For clarity purpose we have not introduced the ^{14}N quadrupolar electric hyperfine interaction since this parameter does not modify the ESR transitions.

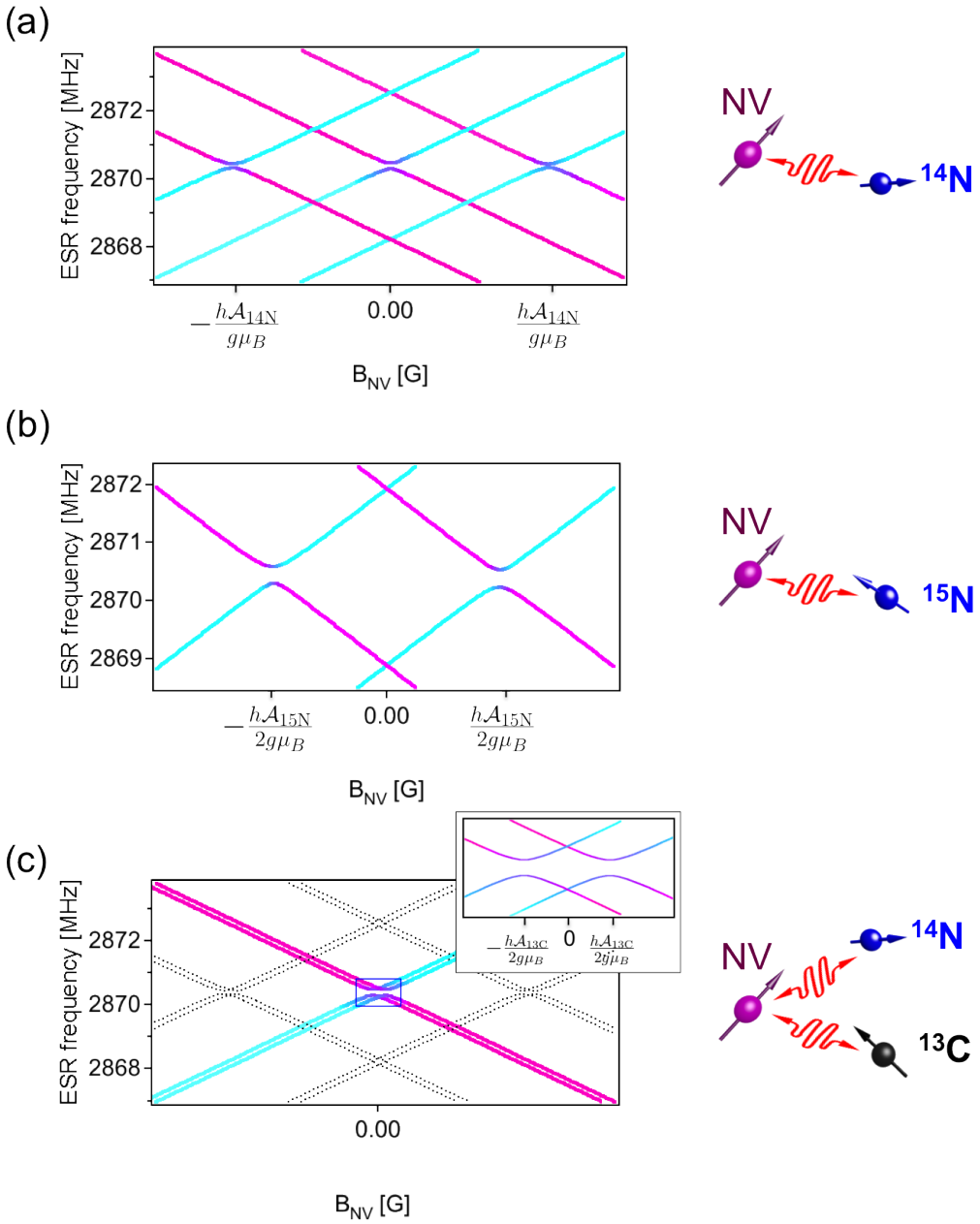

Figure 6.2: Representation of the frequency shifts of the ESR lines as a function of the magnetic field amplitude for the NV center electron spin coupled to a ^{14}N nuclear spin $I = 1$ (a), to a ^{15}N nuclear spin $I = 1/2$ (b) and to both ^{14}N and ^{13}C nuclear spins (respectively $I = 1$ and $I = 1/2$) (c).

6.3 Enhancement of coherence near level anti-crossing

6.3.1 Experimental procedure

We will first consider a native NV center, formed deep inside in an ultrapure single-crystal diamond substrate with the natural abundance of ^{13}C atoms (1.1%) and a N concentration less than 5 ppb (Element6, "electronic grade" sample [91]). For the first experiment we chose a NV center, whose electron spin was coupled only to its intrinsic

^{14}N nuclear spin. The ESR spectrum recorded in the absence of intentionally applied magnetic field is shown on the upper graph of Figure 6.3. The detected six resonance lines correspond to the ^{14}N hyperfine structure splitted with approximately 1 MHz. This splitting is associated to Zeeman shifts induced by a remaining external field magnetic field. The inferred value of 0.357 G is coherent with the amplitude of the Earth magnetic field.

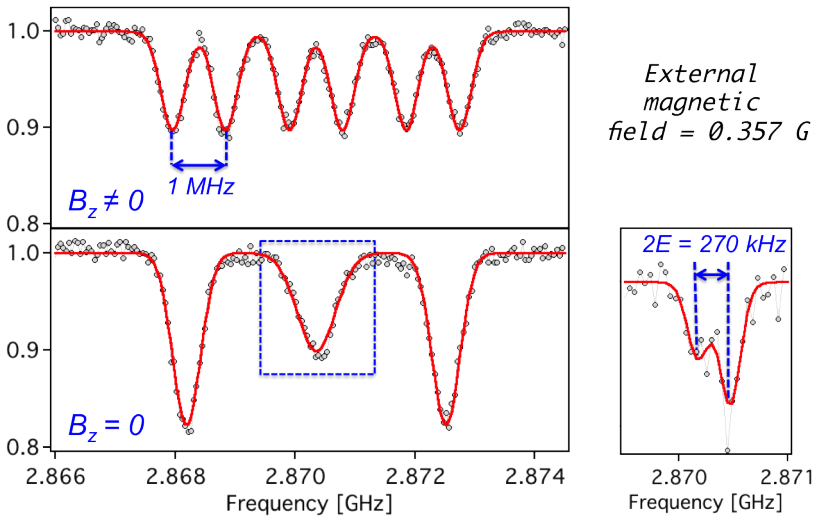

Figure 6.3: Pulsed ESR spectra (π-pulse duration equal to 2 μs) of a single NV center in the ambient condition of the experiment on the upper graph. The frequency spit inferred from the fit gives an estimate of the magnetic field amplitude, equals to 0.357 G. This value is compatible with the Earth magnetic field in the laboratory once projected on the NV axis. The lower graph shows the ESR of the same center at $B_z = 0$ after the compensation of the Earth magnetic field. Zoom on the $m_I = 0$ projection recorded with a π-pulse duration equal to 8 μs, which shows a splitting corresponding to the strain $E = 135$ kHz.

This specific NV center used in the experiment corresponds to the situation of Figure 6.2 (a) with three anti-crossings. We focus on the $m_I = 0$ nuclear spin projection, which anti-crossing appears at zero field. In order to compensate the Earth magnetic field and reach the condition of $B_z = 0$, a coil was added close to the sample. By adjusting the intensity of the applied current in the coil, we can observe the full superposition of the three resonance lines of $m_s = \pm 1$ and then the linewidth of the ESR resonances is minimized (lower graph of Figure 6.3). The expected strain parameter is around 100 kHz, and can not be directly resolved on the presented Figure 6.3 (lower graph). In order to avoid any power broadening effect [136], the π-pulse duration was further increased from 2 μs till 8 μs, then allowing us to record an ESR spectrum with a resolution that can detect the splitting due to strain. From the ESR spectrum recorded on the central lines (inset on the Figure 6.3) we can infer the magnitude of the transverse coupling associated to the strain $E = 135$ kHz. This result agrees with published values of the strain parameter in the case of conventional (100)-oriented samples of CVD-grown diamond [70].

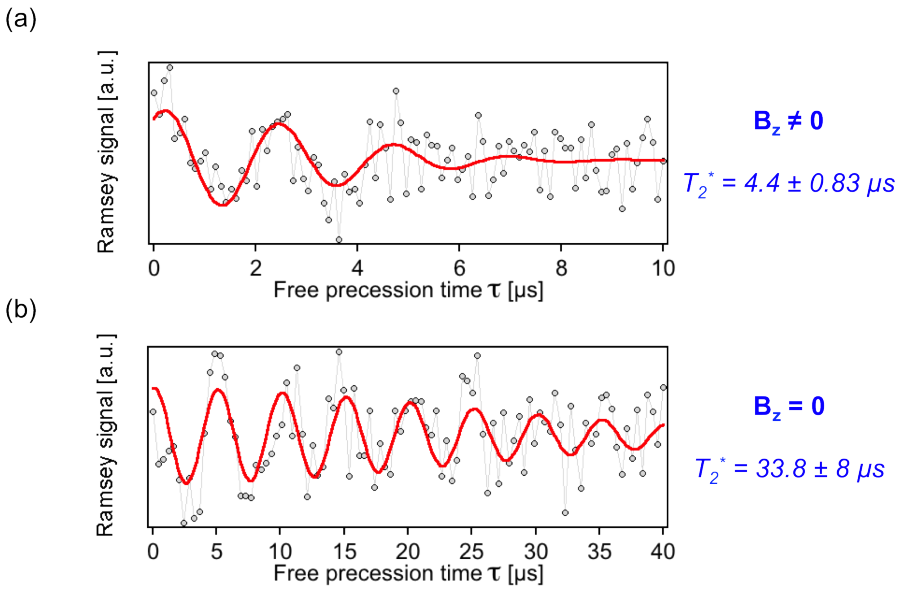

Figure 6.4: Typical relaxation curves obtained using Ramsey sequence applied for a single NV center, which electron spin is only coupled to the ^{14}N nucleus, recorded in the Earth magnetic field (a) and after compensation (b). The selective excitation of the anti-crossing states leads to an enhancement of the spin coherence.

6.3.2 Results and discussion

Since the anti-crossing appears at zero magnetic field, two other resonance may influence the microwave excitation of the NV electron spin (see Figure 6.2 (a)). The measurement of T_2^*-time, performed with a Ramsey sequence, is then realized by applying a selective microwave excitation.

Typical time evolutions recorded with the Ramsey sequence are shown on Figure 6.4. When $B_z \neq 0$ the value of T_2^* is on the order of few μs, which corresponds to the usual value of the coherence time measured for native NV centers placed in ultrapure CVD diamonds. At the anti-crossing $B_z = 0$, much more Ramsey oscillations are observed indicating a clear enhancement of T_2^*.

If then to repeat Ramsey signal measurements by varying the applied magnetic field, it can be seen that in the proximity of $B_z = 0$, the coherence time increases till its maximum value reached for $B_z = 0$ (Figure 6.5 (a)). This can be explained by the fact that the chosen NV center in the mixing states $|\pm\rangle$ of Eqs. 6.4 and 6.5 becomes decoupled from any magnetic noise generated by the other existing spins in the lattice and which are the main source of decoherence for the NV electron spin.

As can be seen from Figure 6.2 (c), in the case of a NV center coupled to both ^{14}N and ^{13}C nuclear spins, this protection effect will not occur for $B_z = 0$. Nevertheless, two anti-crossings are achievable around this value, if an external applied magnetic field is applied in order to compensate the hyperfine splitting due to the ^{13}C nucleus.

The measured time evolutions using Ramsey sequences gave a similar distribution

of the coherence time, with an enhancement of T_2^*-time observed at the mixing states condition. The value of enhancement corresponds to the earlier measured for the NV center - around a factor $\times 6$.

However the coherence time depends not only on magnetic field fluctuations of the environment, but as well on the electric field fluctuations. That means that even after canceling the effect of magnetic field fluctuations, the NV center spin is still affected by electric noise. In order to verify this property at least in the qualitative way, the amplitude of the fluctuations associated to the E-field noise should be tuned.

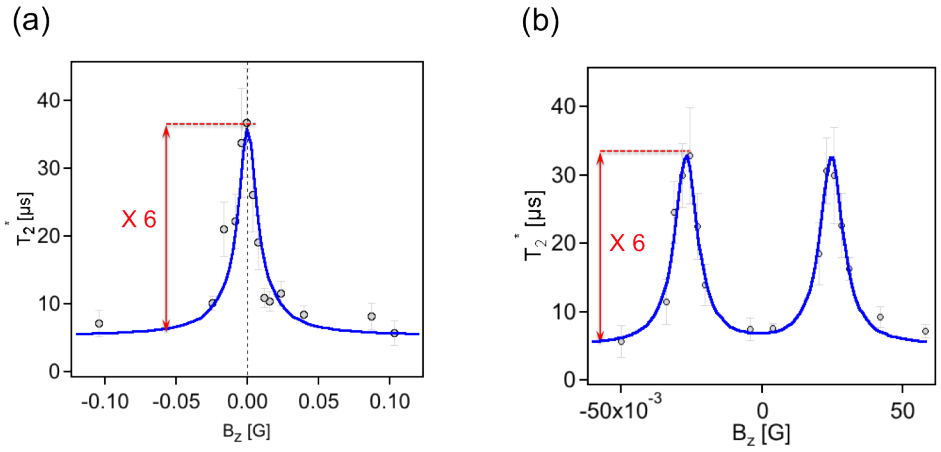

Figure 6.5: Coherence time enhancement for the native NV center coupled to ^{14}N nuclear spin (a) and to both ^{14}N and ^{13}C nucleus (b). The splitting between two enhancement peaks correspond to 150 kHz, which is the hyperfine splitting with the ^{13}C carbon nucleus [135, **?**].

It should be noted that the pulsed ESR technique allowing us to avoid any optical power broadening will be limited by coherence properties of NV centers [136]. For instance, a typical NV center in CVD diamond with the natural abundance of ^{13}C atoms possesses $T_2^* = 2$ μs, what corresponds to an ESR linewidth of $\approx$ 200 kHz FWHM. This value defines the sensitivity of the pulsed ESR method as a spectroscopy technique, since splittings smaller than 200 kHz will not be possible to detect on the spectra. Moreover it leads to a significant drop of the contrast in the optical detection of the magnetic resonance. However the full elimination of magnetic field noise could be used to detect weaker couplings between the NV center electron spin and ^{13}C nucleus.

6.4 Influence of electric field noise on the T_2^*-time

In the previous section we demonstrated that in the case of a NV defect deep inside the crystal, the properties of the NV electron spin can be protected from decoherence effects induced by the magnetic field fluctuations (Figure 6.6 (a)). In order to investigate the influence of electric field fluctuations we should consider the coherence time evolution

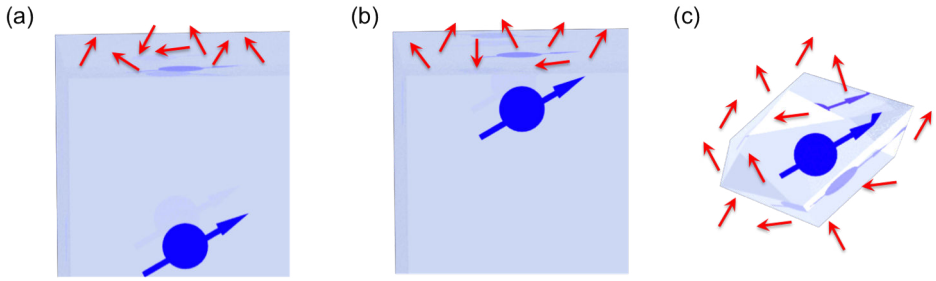

Figure 6.6: Schematic representation of (a) a native NV center deep inside the sample; (b) an implanted NV center placed around 12-15 nm below the surface, and (c) a NV center hosted in a nanodiamond. These three configurations correspond to different regimes of the electric field fluctuations that are experienced by a NV center in the proximity of the surface.

at higher impact of E field. This regime can be realized by approaching the NV center towards the surface of the bulk sample (Figure 6.6 (b)) or by considering a NV center hosted inside a nanodiamond (Figure 6.6 (c)).

6.4.1 NV defect implanted close to the surface

In order to investigate the property of a shallow NV center, an ultrapure CVD diamond was implanted with a 10 keV nitrogen ion-beam. Based on the SRIM software [88], the estimated depth of the defects corresponds to approximately 12 to 15 nm below the surface. To ensure that we investigate the property of an implanted NV center and not a native one that might already exist in the sample, the implantation was performed with the ^{15}N isotope [86]. As expected, the value of the measured strain parameter $E = 220$ kHz is higher than the one previously reported for a native NV center (Figure 6.7 (a)).

The Ramsey sequence recorded with a static magnetic field out of the anti-crossings at $B_z \neq \pm h\mathcal{A}_{\shortparallel}^{(^{15}\mathrm{N})}/2 \cdot g\mu_B$ gave $T_2^* \cong 1\mu$s (Figure 6.7 (b)). The slight reduction in the value of the coherence time may be attributed to the substitutional nitrogen atoms in the diamond lattice introduced by the implantation which remain as P1 defects without being converted into NV centers. Thus, by canceling the magnetic field influence on the NV center after compensation with an external magnetic field $B_z = \pm h\mathcal{A}_{\shortparallel}^{(^{15}\mathrm{N})}/2 \cdot g\mu_B$, equal to $B_z = \pm 0.54$ G, the system becomes insensitive to any magnetic field interaction while remaining affected by the electric field fluctuations, and impact the value of coherence time reaches $T_2^* = 2$ µs. The increased influence of the surface and the associated electric field fluctuations leads to an enhancement of T_2^*-time of only a factor of $\times 2$, weaker than the one previously measured (Figure 6.8 (a)).

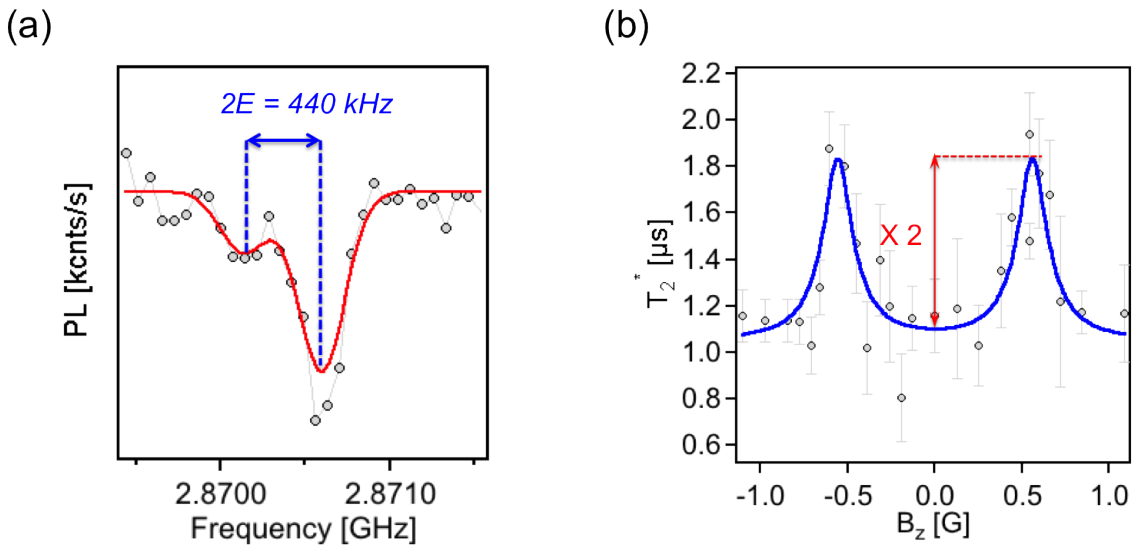

Figure 6.7: (a) ESR spectrum zoom recorded with $B_z = 0.54$ G showing the strain splitting $E \approx 220$ kHz. (b) Coherence time enhancement for an implanted NV center at 12-15 nm depth below the surface of a bulk single-crystal diamond.

6.4.2 NV defect hosted in a diamond nanoparticle

NV centers hosted inside nanodiamonds have usually reduced coherence properties compared to the bulk case with similar nitrogen impurity concentration, and the reported values of T_2^*-time are of few hundreds of nanoseconds [131]. Since a NV center hosted inside a nanodiamond is in close proximity to "noisy" spins associated to broken bonds at the surface of the nanoparticle, the surface could be expected to have a detrimental influence on the coherence properties of the NV center electron spin. The technique discussed on this chapter, which allowed us to improve the T_2^*-time could then help to protect the NV spin from the surface magnetic noise.

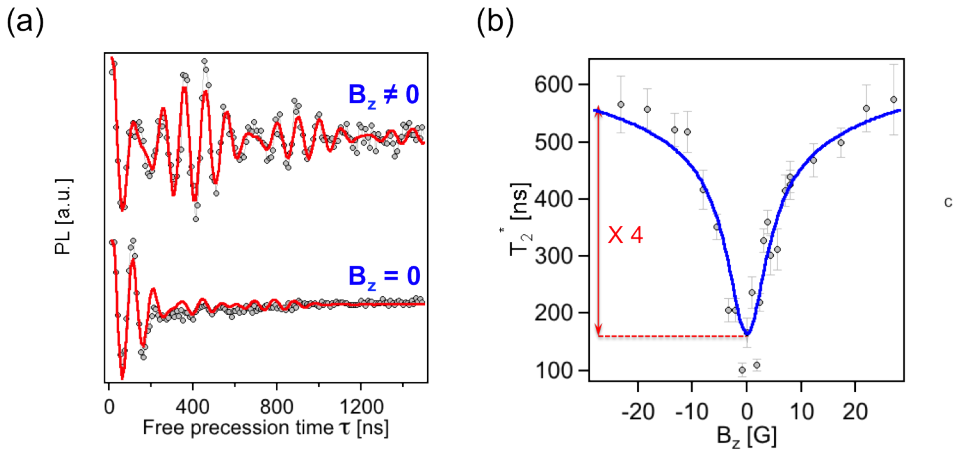

Figure 6.8: (a) Typical curves of free precession signal recorded on a native NV center hosted in a nanodiamond by applying a Ramsey sequence. (b) Coherence time evolution as a function of the magnetic field.

Figure 6.8 (b) shows the result of the experiment performed on a NV center hosted

in a nanodiamond with ≈ 50 nm diameter. As expected, the electron spin possesses a smaller coherence time than in the case of the previous bulk samples (Figure 6.5). By applying an external magnetic field on the NV center to $B_z = 0$, we observed a decrease of the coherence time T_2^*. The evolution of T_2^* as a function of B_z is shown on Figure 6.8, with the opposite behavior compared to the bulk case.

Analyzing the value of the coherence time modification in the strain-protected region we can notice that it is mostly defined by the value of the strain. Its positive or negative behavior depends on the ratio between the B-noise and E-noise. Indeed, from the measured graphs we can see that a NV center deep inside the sample leads to an enhancement of $\times 6$, even if it is coupled to a ^{13}C nucleus. In the case of NV centers in proximity of the surface, the T_2^*-time enhancement is only a factor of $\times 2$ due to an increased electric field noise component. Finally performed studies on a NV center hosted in a nanodiamond showed again similar effects, but leading to the inverse behavior for T_2^*. We attribute this result to higher electric field fluctuations, modifying their relative influence compared to the magnetic field fluctuations. These preliminary results will however require complementary experiments and modeling.

6.5 Conclusion

We showed that the influence of strain in the diamond lattice can put the electron spin of the NV enter in eigenstates which are insensitive to the magnetic field at first order. Since the spin becomes decoupled from the magnetic noise, its coherence properties are improved, indeed as observed from measurements of the T_2^*-time performed with Ramsey sequence. The enhancement of the coherence in those "strain-protected" quantum states is then limited by the electric field noise which modify on the spin energy levels through Stark shifts.

We observe that the strong influence of strain in nanodiamonds leads to an opposite effect. By applying an external magnetic field which sets the NV center spin in B-protected eigenstates, the coherence time T_2^* is then decreased by a factor of $\times 1.4$. This effect is attributed to an enhancement of detrimental influence of the electric noise which could be generated by the defects on the surface of the nanoparticle.

Conclusion

The main objective of the thesis was to investigate a set of methods aimed to engineer NV centers in diamond and optimize their physical properties. After the introduction in the first chapter of the relevant properties of these point defects for their applications in quantum information and sensing, and the challenges which are associated to the control of the basic material, the second chapter described how NV centers can be created using FIB technology. The ion beam can be associated to scanning electron microscopy allowing us to simultaneously observe the implantation spot on the target. The additional implementation of the sub-diffraction optical imaging technique based on ground-state depletion allowed us to evaluate the resolution reached in the implantation of the nitrogen atoms, due to the focus of the ion beam of approximately 100 nm. This method paves the way to the engineering of arrays of magnetically-coupled NV centers ultimately limited by the straggling of the ions when they penetrate in the matter, and their fabrication inside a photonic microstructure such as a photonic crystal or at the apex of a diamond AFM tip.

The NV centers as spin-based qubits are extremely sensitive to their environment. Therefore the possibility to gain in ion-positioning by using low-energy implantation turns over worse properties of the created NV centers due to the proximity of the surface. In the third chapter we showed that the CVD technique used for the plasma-assisted growth of diamond can improve the properties of such shallow NV centers, by overgrowing an ultrapure single-crystal diamond layer over the implanted patterns.

The CVD technique is also a powerful tool for the formation of a thin layer doped with NV centers and which is embedded inside the crystal. The possibility to control precisely the thickness of this "δ-doped" layer was previously demonstrated using an optimized power of the microwave injected in the chamber in order to create the plasma. However, the plasma in this regime can only dissociate N_2 molecules with a low efficiency and as a consequence leads to a poor incorporation of native NV defects, in the contrary to a plasma with high-power microwave which enhances the nitrogen doping. We also investigated an alternative technique for "δ-doping" with nitrogen by decreasing the temperature of the deposition substrate. The rough estimate of the doped layer, inferred from the intensity of the detected photoluminescence, showed a NV density higher than 10^{12} NV/cm^3 within a thickness smaller than 1 μm. Further improvements could be achieved by decreasing the duration of growth.

The following chapter was devoted to the orientation control of NV centers. We showed the possibility to obtain a diamond layer hosting identically oriented NV centers with 97% fidelity in a [111]-oriented sample, compared to a random distribution between the four possible axis associated to the orientation of a NV center in a standard (100)-oriented sample. This result originates from the creation of the NV center as a unit during the atom-by-atom built-up of the diamond atomic layers during the vapor deposition. We then showed that the degree of orientation reached for a (113)-oriented sample is 73%, which is still an attractive value since single-crystal diamond in (113)-orientation can be grown more easily and with less defects compared to the (111) case.

This almost ideal control of the NV axis is well appropriate to magnetic sensing. It also optimizes the coupling to photonic structures, such as micropillars or photonic crystals. Moreover combined with the "δ-doping" technique described in Chapter 4, it can dramatically increase the sensitivity of a magnetic field sensor based on a thin highly doped diamond layer since all the NV centers in the layer will have an identical response to the magnetic field.

All applications of NV centers benefit from the optimization of the coherence properties of the electron spin. The last chapter was devoted to this issue. We showed that for a NV center hosted in the diamond crystal with large strain parameter, the electron spin can be decoupled from the magnetic noise induced by the bath consisting of magnetic fluctuations created by the uncorralated spins in the diamond lattice. As a direct consequence, the coherence time T_2^* of the NV center electron spin is strongly enhanced, as experimentally checked. Since the defect becomes insensitive to the magnetic field fluctuations, weaker sources of decoherence, such as the electric field noise, could be probed. This property opens the way to new sensing applications for the NV center in order to investigate electric noise and transport properties in condensed matter, biology, and microelectronics technology.

APPENDIX A

Experimental setup

All sample characterization and measurement of properties of NV centers reported in this work were performed using a customized setup for optical confocal microscopy, first implemented in Bochum during the first year of the thesis work and then brought back to ENS Cachan. It is schematically presented on Figure A.1. The main purpose of this set-up was the possibility to study implanted samples, what implies the implementation of photoluminescence spectral analysis for fabricated structures using the confocal microscope, photon-statistics measurement to ensure if it is a single emitter [137] and Ground-State Depletion (GSD) imaging to resolve the position of the emitters below the diffraction limit [84].

Optical excitation of the NV color centers was realized with a green laser operating at 532 nm wavelength (Gem FC, Laser Quantum), focalized through an oil-immersion microscope objective (Olympus, ×60, 1.32NA). In order to perform the raster-scan images of the sample the microscope objective was mounted on a piezo-electric stage combined with Nano-Drive controller (Mad City Labs, USA), which enables translations within three axes with displacement range 75×75×50 μm in transverse and axial direction.

The emitted photoluminescence by NV centers was collected by the same microscope objective, filtered with a dichroic mirror and bandpass filter centered at 697 nm with 75 nm transmission window. This combination allows us to cut residuals of green laser light while keeping most of the light emitted by NV^- center (Figure A.3). The detection of the collected photoluminescence is realized with a set of two avalanche photodiodes (Perkin Elmer, SPCM-AQR-14) operating in photon counting mode.

A.1 Imaging

The confocal imaging resolution is diffraction limited. It has a resolution given by the Abbe formula:

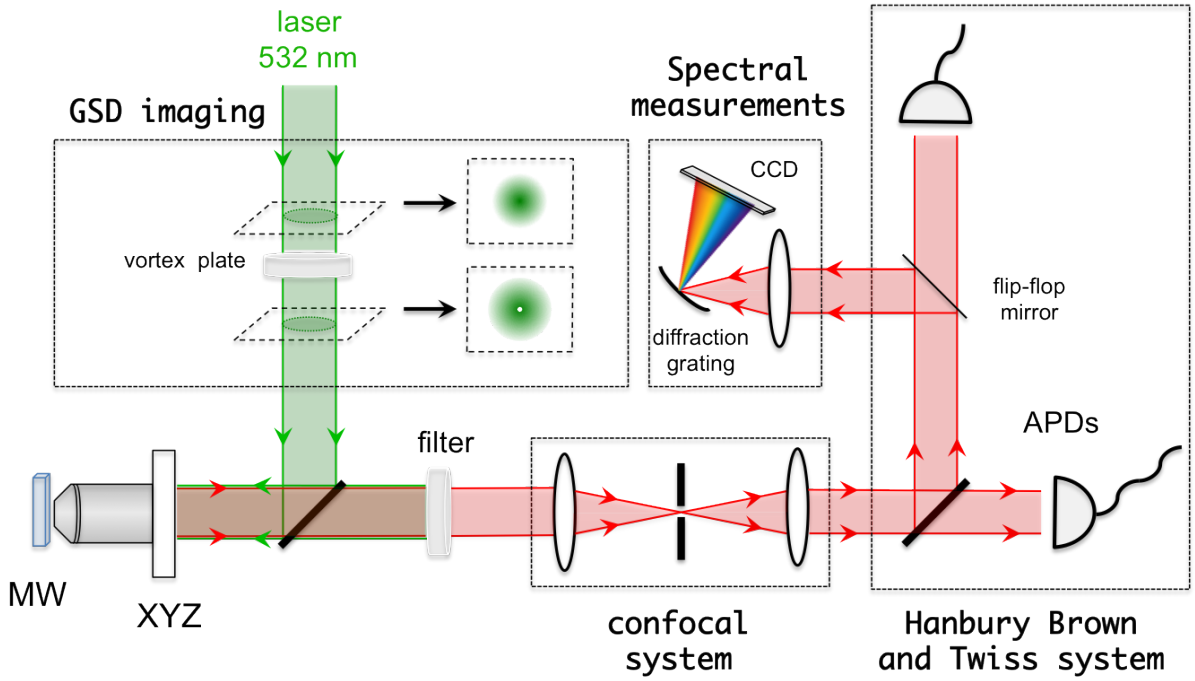

Figure A.1: Schematic representation of the optical confocal microscope setup. The detection part consisted of 2 avalanche photodiodes, equipped with an electronic delay line to enable photon statistics measurements. GSD part was added for sub-diffraction imaging.

$$d = 1.22 \cdot \frac{\lambda}{2 \times NA} \cong 300\,\text{nm} \tag{A.1}$$

where λ is the wavelength and NA is numerical aperture.

To enhance the imaging and be able to resolve the position of two emitters separated by a distance below the diffraction limit the Ground-State Depletion (GSD) technique was implemented. The vortex plate is introduced on excitation beam in order to turn a standard gaussian beam profile into a doughnut-shaped beam.

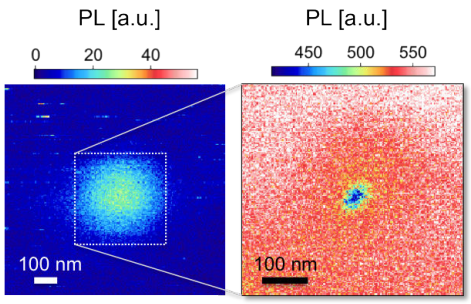

Figure A.2: Single NV center detected with the standard confocal setup (on the left) and then using a doughnut-shaped excitation (on the right).

The geometry allowed us to implement the GSD technique by simply adding a telescope system to enlarge the beam size and the vortex plate at the input of microscope

objective. A $\lambda/4$-plate was installed just before the microscope objective to ensure the circular polarization of the light [138]. The detection part remained unchanged.

A.2 Spectral measurement

The characterization of the samples required to perform the spectral analysis of the collected luminescence. A mirror on a "flip-flop" mount was introduced in the detection part of the setup to detect the luminescence with a customized spectrograph consisting of a grating and CCD detector (Andor Technology).

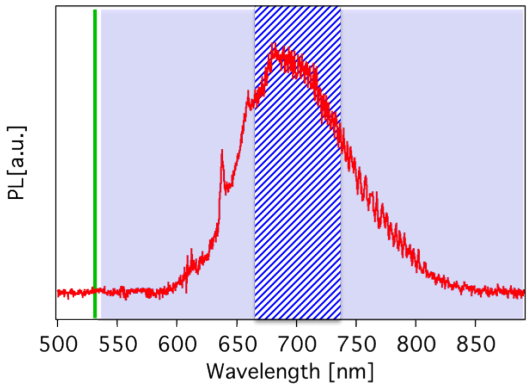

Figure A.3: Photoluminescence spectrum measured for a single negatively-charged NV center. Green line is representing the operating wavelength of the excitation laser, and the blue-transparent region corresponds to the transmitted light through the 535-nm longpass filter. The region indicated blue stripes corresponds to the filter mounted on the confocal imaging part, which is centered at 697 nm wavelength and with a 75 nm-wide transmission window.

It should be noted that for measurements of polarization-dependent PL described in chapter 5 the configuration of the optical setup was slightly modified. Studies on (113)-oriented layers experiments were performed in the configuration with only one detector without beam-splitter, leading to slightly higher PL intensities compared to the PL recorded case of (111)-oriented sample.

A.3 Antibunching experiment

Two detectors were in the Hanbury Brown and Twiss configuration, in order to measure the photon correlation in the emitted light [81]. This experiment is based on the fact that a NV center acts as a single-photon source, leading to the observation of antibunching in the photon statistics (Figure A.4) [5].

The Hanbury Brown and Twiss consists of a beam splitter separating the detected signal into two optical paths configuration with two avalanche photodiodes, focused on the the $g^{(2)}(\tau)$ measurements. The delivered signals are then recorded using a start/stop system, in order to build the histogram of the time correlation between the two photodetection events. Supposing that NV center is a single-photon source, *i.e.* it is able to emit only one photon per unit of time means that at a 0 delay time the emitted photon can not be detected by both APDs at once.

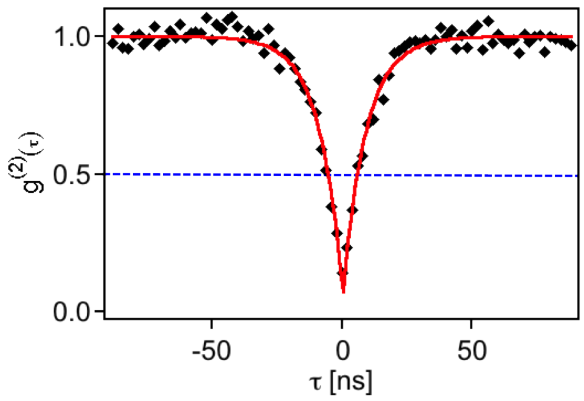

Figure A.4: Antibunching measurement performed on a single NV. The blue dashed line indicates the limit below which measured luminescent spot can be considered as a single emitter. If the dip is less than 1/2, then the spot can contain 2 or more emitters.

A.4 Magnetic resonance experiments

The diamond sample is attached to a printed circuit board in order to perform experiments related to magnetic resonance. To address microwave excitation to a given zone on the sample a copper wire of 20 μm diameter was placed directly on the sample surface and connected to the sample holder by two copper stripes. The printed circuit board is equipped with two SMA connectors soldered on it, corresponding to the input/output for the current driving the transitions between the spin levels of the NV center. The microwave signal is provided by a synthesizer (Rhode&Schwarz, SMB 100A).

The pulsed measurements were implemented from a computer card (Spincore, Pulse Blaster) to generate the TTL pulse sequence corresponding to the pulsed microwave excitation and optical excitation with the time resolution of 2.5 ns. Since the green laser source was emitting in continuous mode, an acousto-optic modulator (AOM) (Opto-electronic) enabled controlled pulsed excitation. A double-pass configuration through the AOM optimized the extinction rate, with ≈75% of diffraction efficiency

for single pass and 13 ns of rise time in the output optical pass. Switch (Mini-ciruits, ZASW-2-50DR+) was used to control the microwave signal.

APPENDIX B

Diagnostics for retrieving the NV center orientation

Carbon-nitrogen bond in diamond will unequally share electrons, making this bond polar. As a consequence one side of the bond possesses a fractional negative charge and the other has a positive charge. Since the electronegativity of the nitrogen atom is higher than of the one carbon (2.55 and 3.04 respectively), the C-N connecting bond will be strongly polarized towards nitrogen. As described in chapter 1 the NV center has C_{3v} symmetry, and since C_{nv} point groups do not have a center of inversion, the NV center has a dipole moment.

As pointed out the NV center exhibits four possible orientations in the diamond layer. In order to facilitate the alignment of an external magnetic field along the NV center axis we used a method of polarization-dependent luminescence of the defect.

The detection of the photoluminescence of a given NV center pinpointed in the sample can be used to retrieve its spatial orientation. The NV center possesses two orthogonal dipoles located in the plane perpendicular to the NV axis, as shown on Figure B.1. Taking an incident linear polarization of the excitation laser, and the angles defined on Figure B.1, the absorbed intensity can be written as [139]:

$$I = I_{(dipole\,1)} + I_{(dipole\,2)} = I_0 \left[1 - cos^2\left(\alpha - \phi\right) sin^2\theta\right] , \tag{B.1}$$

where we assume that two dipoles have equivalent absorption cross-sections. Then the absorption efficiency depends on the value of both angles ϕ and Θ. The laser polarization angle $\alpha = \phi \pm \pi$ gives the minima of absorption $I_{min} = I_0 \cdot \cos^2\Theta$, while for $\alpha = \phi + \pi/2$, the absorption is at its maximum value $I_{max} = I_0$. The minimum of the detected PL intensity occurs when the laser polarization is parallel to the projection on the xy-plane of the NV center axis. This diagnostics can be used to retrieve the angle ϕ modulus π, since the detected signal can not distinguish between the two orientations of the N-to-V axis.

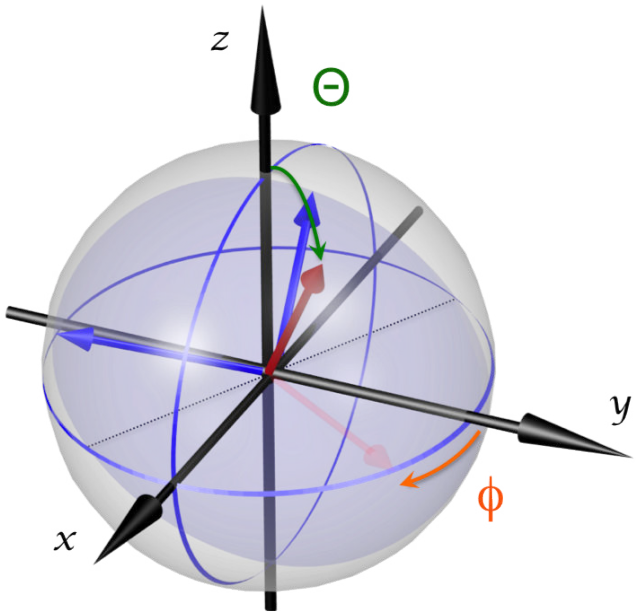

Figure B.1: Schematic representation of the NV center axis (with red arrow) and its two mutually orthogonal dipoles (with blue arrows), which are forming an orthogonal plane (blue transparent) to its axis. The crossing line of the dipole plane and surface plane is denoted with the black dashed line. The azimuthal angle ϕ - depends on the NV center axis projection (red transparent arrow) on the sample surface plane defined as XY. The polar angle Θ is the angle between the NV center axis and the normal to the diamond sample. It corresponds to the optical axis in the used setup geometry described in appendix A.

As depicted in chapter 5, we investigated the orientation of NV centers in different types of substrates, which are schematically presented on Figure B.2.

B.1 (100)-oriented sample

NV centers in the conventional (100) diamond sample oriented along four crystallographic axis will form similar angles with the normal to the diamond surface. Therefore fixing the B-field axis perpendicular to the diamond sample will provide equivalent Zeeman shifts of the magnetic resonance lines. However the recorded PL intensity can be used as a diagnostics of the center orientation, which is possible due to the fact that the dipole moments of optical transitions are lying in the perpendicular plane to the NV center quantization axis [83].

The efficiency of NV center excitation rate and collection efficiency of emitted signal depends on how the sample is mounted way and the experimental setup geometry which is described in appendix A. In our case the sample is placed perpendicular to the optical axis of optical excitation and collection paths. Therefore as the laser polarization is rotated in the plane of the sample surface, the effective excitation rate of the NV color center will vary according to the projection of its two dipole transitions on it.

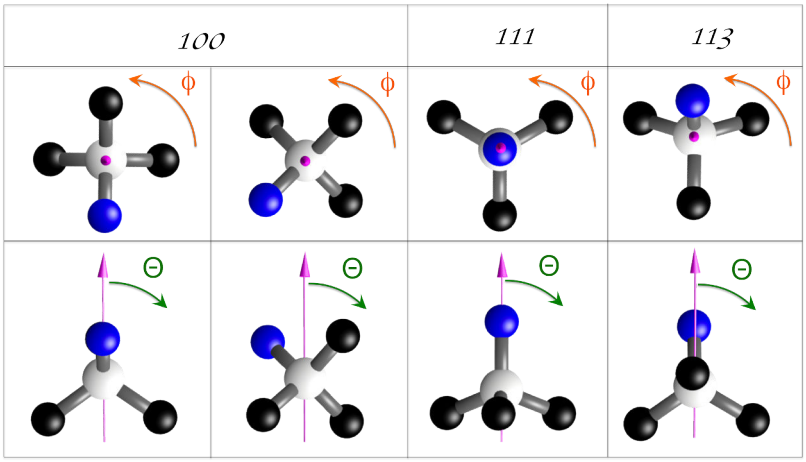

Figure B.2: Schematic representation of the crystallographic orientations for different substrates. The top raw corresponds to the projection of the possible NV center orientations onto the diamond surface with associated values of ϕ. The lower raw is depicting the side view of these NV center orientations; where the pink arrow indicates the normal to the surface and the formed angles Θ.

The plane formed by two orthogonal dipoles is represented on Figure B.3 (a). As shown in Figure B.3, the angle ϕ is inferred directly from the minima of detected PL signal, denoted with dashed arrows. Since the diagnostics can not discriminate between ϕ and $\phi \pm \pi$, all four orientations will exhibit one of two polarization-dependent PL polar plots shown on Figure B.3 (b) and (c).

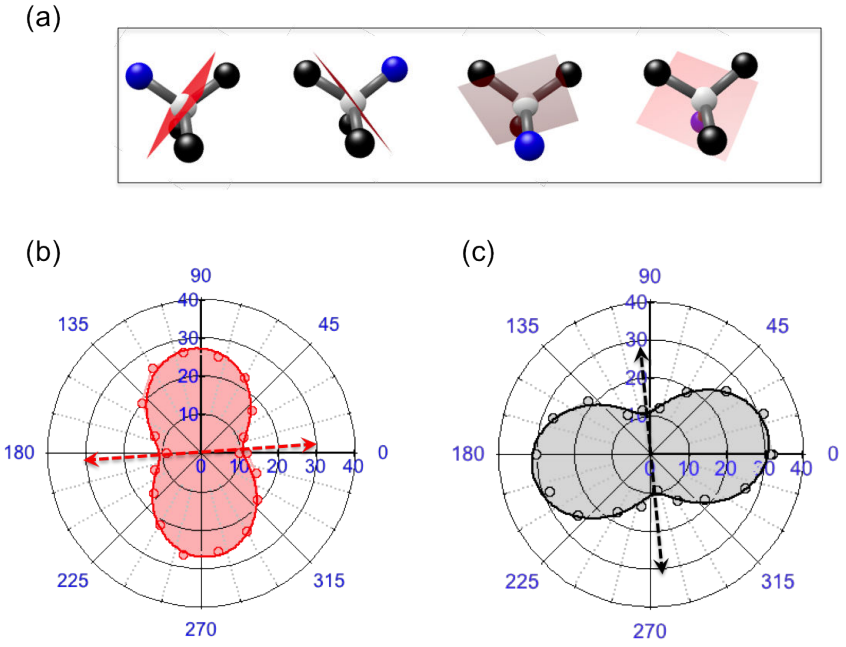

Figure B.3: Polarization-dependent PL signal for two NV centers inside a (100)-grown sample, with two different orientations.

B.2 (111)-oriented sample

The (111)-orientation of diamond crystal, corresponds to one of the crystallographic axis of the lattice being perpendicular to the diamond surface (Figure B.2). It provides dipoles located inside a plane which is parallel to the sample surface leading to efficient and equal excitation rates of both of them. Figure B.4 shows the PL signals in a polar plot detected from two NV centers formed in a [111]-grown diamond layer.

Moreover the polarization-dependent PL intensity provides an information concerning complementary the angle Θ, which can be estimated using the following equation, so that the orientation (ϕ, Θ) can be retrieved [140]:

$$\Theta = \arccos \sqrt{\frac{I_{min}}{I_{max}}} \tag{B.2}$$

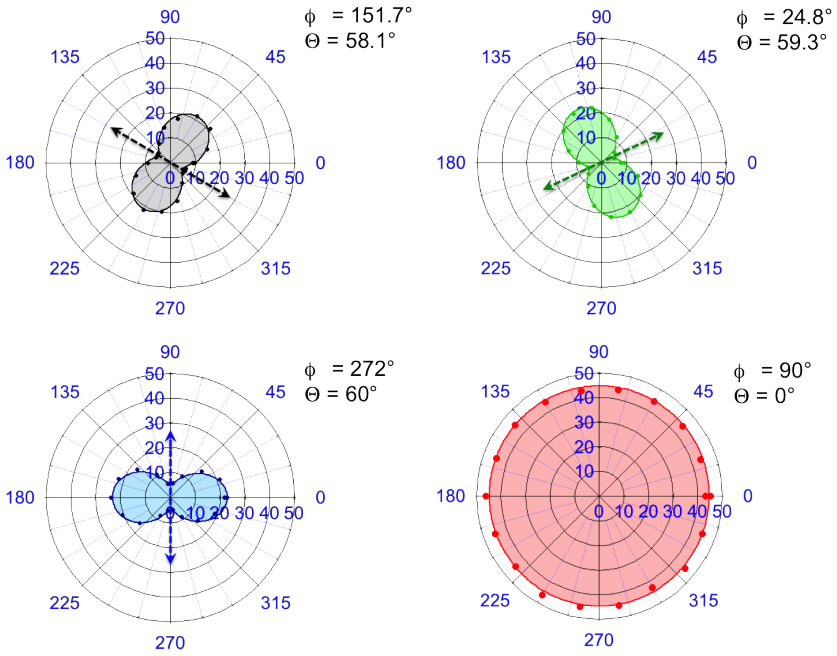

Figure B.4: Polarization-dependent PL signal measured on four differently oriented NV centers formed in [111] oriented diamond layer

The statistics measured and analyzed in chapter 5 devoted to the occurrence of each of the four orientations, was obtained using this polarization-dependent method, since this three orientations with similar Θ are associated to the same resonance lineshift in the condition of an applied magnetic field parallel to the [111]-crystallographic axis. It can be seen that [111]-oriented NV center formed sample has no PL luminescence fluctuation, due to the polar angle $\Theta = 0$.

B.2.1 (113)-oriented sample

As described in chapter 5, we also investigated a layer grown on a (113)-oriented substrate. The oriented diagnostics gave the polar graphs shown on Figure B.5. The angles found by the fits roughly correspond to the expected axis projection, however with an uncertainty remaining quite important. Note that the diagnostics can nevertheless be considered as a useful tool to determine the absolute orientation of a pinpointed NV center, e.g. in order to align on its axis in the external magnetic field.

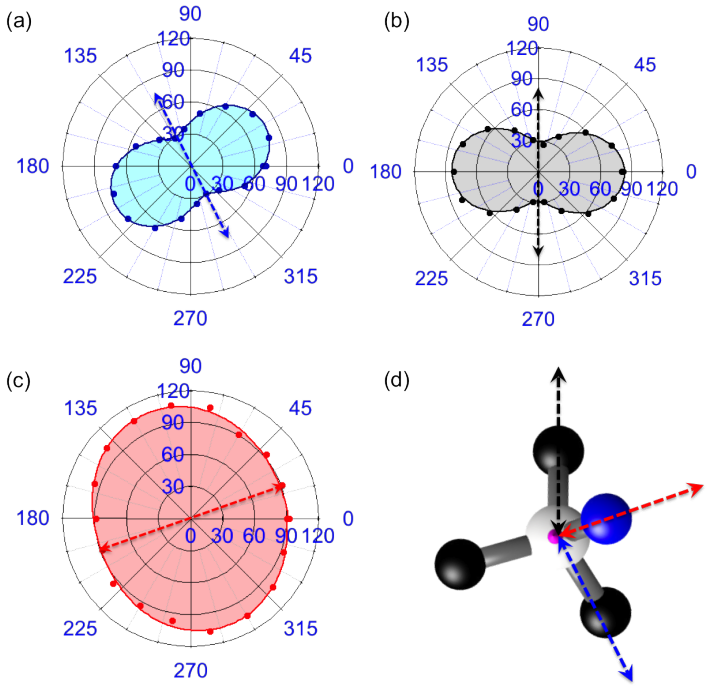

Figure B.5: Polarization-dependent PL signal measured on four differently oriented NV centers formed in [111] oriented diamond layer

APPENDIX C

Homoepitaxial growth of diamond

C.1 Growth on a (111)-oriented substrate

The production of high-quality (111)-oriented crystals is a hard-to-reach goal, since it is mainly complicated by its intrinsic bias towards the growth in the twinning configuration. Such morphology defect can happen if the diamond growth along a given direction is interrupted or modified due, for instance, to the incorporation of an atom with a different size than the carbon atom of the diamond lattice. The consequence is an increased surface roughness which might affect the electronic properties of the grown diamond layer. Moreover growth in the (111)-direction is known to induce a higher incorporation efficiency for impurities compared to the (100)-oriented homoepitaxial growth.

Significant progress as in the quality of (111)-oriented diamond growth has been achieved using the HPHT method, which the synthesis of diamonds of *IIa* purity as large as 4 nm [141]. Alternative technique for the diamond synthesis is the plasma-assisted chemical vapor deposition (PACVD) method, which allows fine control of the diamond growth environment and a high flexibility for the choice of the growth parameters. However the PACVD growth technique was mainly optimized for the synthesis of single-crystal (100)-oriented diamond samples.

Diamond growth using the PACVD technique can lead to twinning effects originating from some growth errors caused by crystal domains rotations relatively to its parent crystal [142]. Twinning configuration on the (111)-plane lead to the crystal-growth rotation with the angle of 70.5°. Such defects lead not only to the structural modifications as shown on Figure C.1, but as well to the formation of electronic defects , and therefore should be carefully avoided.

The simulation of the twin formation were performed taking into account an assumption that the growth rate on {100} and {111} facets is constant, independently

Figure C.1: Electron microscope image of the diamond surface with the twinned configuration [143].

from the size of the substrate and its orientation. Then the only relevant parameter affecting the growth of the crystal is:

$$\alpha = \sqrt{3} \cdot \frac{V_{(100)}}{V_{(111)}} \tag{C.1}$$

where $V_{(100)}$ and $V_{(111)}$ are the growth velocities for the (100) and (111) planes respectively. The occurrence of twin defects can hardly be controlled, but α defines the ratio between the rates of growth in order to control the twins propagation along the crystal growth. Finally it was found that for the regime corresponding to $\alpha < 1.5$, the penetration of the twins can be interrupted.

The effect of the different growth parameters on the value of α has been already investigated, and the possibility to grow thick and high-quality (111)-oriented layers using the PACVD technique was demonstrated [144]. Details of this synthesis show that the raise of the growth temperature leads to the decrease of the α parameter, while N_2 or O_2 gas insertion in the growth chamber increases the α value. Finally it was found that the combination of low CH_4 pressure and high plasma temperature can be combined to significantly decrease the α parameter and optimize the growth.

C.2 Growth on a (113)-oriented substrate

Diamond samples studied in chapter 4 were grown on the cylindrical plates fabricated from standard (100) HPHT diamond crystals. The process leading to the (113)-oriented substrate is depicted on Figure C.2. Laser-cuts along the parallel planes and cylinder were performed at Almax EasyLab (Belgium). The angle of cut was chosen as 25.2°, which corresponds to the angle between the (100)-plane and the (113)-plane in the diagonal direction of the initial cubic lattice.

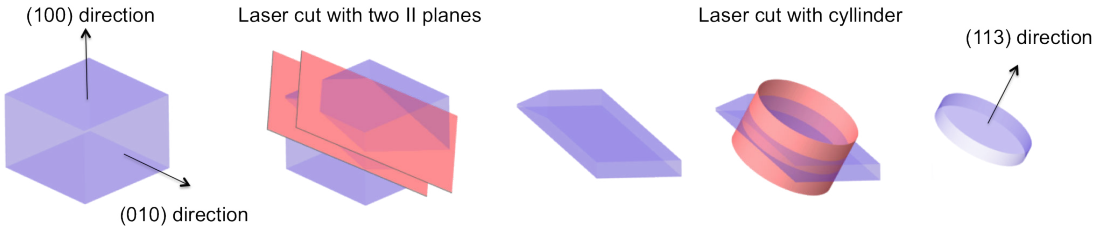

Figure C.2: (113)-oriented substrate preparation process. As initial (100)-oriented diamond is cut using 2 parallel planes rotated with 25.2° angle respectively to the sample surface. This operation is followed with a cylindrical laser cut ending in substrate formation with a 2.4 mm diameter.

The facets of the laser-cut sample were polished. Plasma-assisted CVD growth was then performed on this substrate, with identical conditions as for the standard PACVD growth on a (100)-oriented substrate (high power density plasma, temperature of 900 °C, and $^{H_2}/_{CH_4}$ gas mixture equal to $^{94}/_{6}$).

Bibliography

[1] R. Brouri, A. Beveratos, J.-P. Poizat, and P. Grangier, "Photon antibunching in the fluorescence of individual color centers in diamond," *Opt. Lett.*, vol. 25, no. 17, pp. 1294–1296, Sep 2000. [Online]. Available: http://ol.osa.org/abstract.cfm?URI=ol-25-17-1294

[2] C. Kurtsiefer, S. Mayer, P. Zarda, and H. Weinfurter, "Stable solid-state source of single photons," *Phys. Rev. Lett.*, vol. 85, pp. 290–293, Jul 2000. [Online]. Available: http://link.aps.org/doi/10.1103/PhysRevLett.85.290

[3] A. Beveratos, S. Kuhn, R. Brouri, T. Gacoin, J.-P. Poizat, and P. Grangier, "Room temperature stable single-photon source," *Eur. Phys. J. D*, vol. 18, no. 2, pp. 191–196, 2002. [Online]. Available: http://dx.doi.org/10.1140/epjd/e20020023

[4] V. Jacques, E. Wu, F. Grosshans, F. Treussart, P. Grangier, A. Aspect, and J.-F. Roch, "Experimental realization of wheeler's delayed-choice gedanken experiment," *Science*, vol. 315, no. 5814, pp. 966–968, 2007.

[5] A. Beveratos, R. Brouri, T. Gacoin, A. Villing, J.-P. Poizat, and P. Grangier, "Single photon quantum cryptography," *Phys. Rev. Lett.*, vol. 89, p. 187901, Oct 2002. [Online]. Available: http://link.aps.org/doi/10.1103/PhysRevLett.89.187901

[6] J.-R. Bertrand, C. Pioche-Durieu, J. Ayala, T. Petit, H. A. Girard, C. P. Malvy, E. L. Cam, F. Treussart, and J.-C. Arnault, "Plasma hydrogenated cationic detonation nanodiamonds efficiently deliver to human cells in culture functional sirna targeting the ewing sarcoma junction oncogene," *Biomaterials*, vol. 45, no. 0, pp. 93 – 98, 2015. [Online]. Available: http://www.sciencedirect.com/science/article/pii/S0142961214012514

[7] M.-P. Adam, L. L. Xuan, A.-M. Lepagnol-Bestel, A. Thomas, G. Dantelle, C.-C. Chang, N. Mohan, H.-C. Chang, F. Treussart, and M. Simonneau, "Fluorescent diamond nanoparticle as a probe of intracellular traffic in primary neurons in culture," *Colloidal Nanocrystals for Biomedical Applications VII*, p. 823203Ð823203Ð6, 2012.

[8] L. Hall, D. Simpson, and L. Hollenberg, "Nanoscale sensing and imaging in biology using the nitrogen-vacancy center in diamond," *MRS Bulletin*, vol. 38, pp. 162–167, 2 2013.

[9] M. Markham, J. Dodson, G. Scarsbrook, D. Twitchen, G. Balasubramanian, F. Jelezko, and J. Wrachtrup, "CVD diamond for spintronics," *Diamond and Related Materials*, vol. 20, no. 2, pp. 134 – 139, 2011. [Online]. Available: http://www.sciencedirect.com/science/article/pii/S0925963510003274

[10] J. R. Maze, P. L. Stanwix, P. L. Stanwix, J. S. Hodges, S. Hong, J. M. Taylor, P. Cappellaro, L. Jiang, M. V. G. Dutt, E. Togan, A. S. Zibrov, A. Yacoby, R. L. Walsworth, and M. D. Lukin, "Nanoscale magnetic sensing with an individual electronic spin in diamond," *Nature*, vol. 455, no. 0028-0836, pp. 644–647, 2008.

[11] J. M. Taylor, P. Cappellaro, L. Childress, L. Jiang, D. Budker, P. R. Hemmer, A. Yacoby, R. Walsworth, and M. D. Lukin, "High-sensitivity diamond magnetometer with nanoscale resolution," *Nature Physics*, vol. 4, pp. 810–816, 2008. [Online]. Available: http://www.nature.com/nphys/journal/v4/n10/abs/nphys1075.html

[12] L. Rondin, J.-P. Tetienne, P. Spinicelli, C. Dal Savio, K. Karrai, G. Dantelle, A. Thiaville, S. Rohart, J.-F. Roch, and V. Jacques, "Nanoscale magnetic field mapping with a single spin scanning probe magnetometer," *Applied Physics Letters*, vol. 100, no. 15, pp. –, 2012. [Online]. Available: http://scitation.aip.org/content/aip/journal/apl/100/15/10.1063/1.3703128

[13] A. Zaitsev, *Optical Properties of Diamond: A Data Handbook*. Springer, 2001.

[14] M. N. Satoshi Koizumi, Christoph Nebel, *Physics and Applications of CVD Diamond*. WILEY-VCH Verlag, 2008.

[15] V. S. Babu, *Solid State Devices and Technology*. Pearson Education (2010), 2010.

[16] K. Groot-Berning, N. Raatz, I. Dobrinets, M. Lesik, P. Spinicelli, A. Tallaire, J. Achard, V. Jacques, J.-F. Roch, A. M. Zaitsev, J. Meijer, and S. Pezzagna, "Passive charge state control of nitrogen-vacancy centres in diamond using phosphorous and boron doping," *physica status solidi (a)*, vol. 211, no. 10, pp. 2268–2273, 2014. [Online]. Available: http://dx.doi.org/10.1002/pssa.201431308

[17] J. R. Rich Mildren, Ed., *Optical Engineering of Diamond*, 1st ed. Wiley-VCH, 20 May 2013.

[18] D. Talbot-Ponsonby, M. Newton, and J. Baker, "Electron paramagnetic resonance imaging of the distribution of the single substitutional nitrogen impurity through

polycrystalline diamond samples grown by chemical vapor deposition," *Journal of Applied Physics*, vol. 82, no. 3, pp. 1201–1204, Aug 1997.

[19] A. Cox, M. E. Newton, and J. M. Baker, "^{13}C, ^{14}N and ^{15}N ENDOR measurements on the single substitutional nitrogen centre P1 in diamond," *Journal of Physics: Condensed Matter*, vol. 6, no. 2, p. 551, 1994. [Online]. Available: http://stacks.iop.org/0953-8984/6/i=2/a=025

[20] G. Davies, S. C. Lawson, A. T. Collins, A. Mainwood, and S. J. Sharp, "Vacancy-related centers in diamond," *Phys. Rev. B*, vol. 46, pp. 13 157–13 170, Nov 1992. [Online]. Available: http://link.aps.org/doi/10.1103/PhysRevB.46.13157

[21] Y. Mita, "Change of absorption spectra in type-Ib diamond with heavy neutron irradiation," *Phys. Rev. B*, vol. 53, pp. 11 360–11 364, May 1996. [Online]. Available: http://link.aps.org/doi/10.1103/PhysRevB.53.11360

[22] A. Gali, M. Fyta, and E. Kaxiras, "Ab initio supercell calculations on nitrogen-vacancy center in diamond: Electronic structure and hyperfine tensors," *Phys. Rev. B*, vol. 77, p. 155206, Apr 2008. [Online]. Available: http://link.aps.org/doi/10.1103/PhysRevB.77.155206

[23] G. Davies and M. F. Hamer, "Optical studies of the 1.945 eV vibronic band in diamond," *Proceedings of the Royal Society of London. A. Mathematical and Physical Sciences*, vol. 348, no. 1653, pp. 285–298, 1976. [Online]. Available: http://rspa.royalsocietypublishing.org/content/348/1653/285.abstract

[24] A. Gruber, A. Drabenstedt, C. Tietz, L. Fleury, J. Wrachtrup, and C. v. Borczyskowski, "Scanning confocal optical microscopy and magnetic resonance on single defect centers," *Science*, vol. 276, no. 5321, pp. 2012–2014, 1997. [Online]. Available: http://www.sciencemag.org/content/276/5321/2012.abstract

[25] M. V. Hauf, B. Grotz, B. Naydenov, M. Dankerl, S. Pezzagna, J. Meijer, F. Jelezko, J. Wrachtrup, M. Stutzmann, F. Reinhard, and J. A. Garrido, "Chemical control of the charge state of nitrogen-vacancy centers in diamond," *Phys. Rev. B*, vol. 83, p. 081304, 2011.

[26] B. Grotz, M. V. Hauf, M. Dankerl, B. Naydenov, S. Pezzagna, J. Meijer, F. Jelezko, J. Wrachtrup, M. Stutzmann, F. Reinhard, and J. A. Garrido, "Charge state manipulation of qubits in diamond," *Nature Communications*, vol. 3, no. 729, 2011.

[27] V. Jacques, J. D. Murray, F. Marquier, D. Chauvat, F. Grosshans, F. Treussart, and J.-F. Roch, "Enhancing single-molecule photostability by optical feedback from quantum jump detection," *Applied Physics Letters*, vol. 93, no. 203307, 2008.

[28] Y.-R. Chang, H.-Y. Lee, K. Chen, C.-C. Chang, D.-S. Tsai, C.-C. Fu, T.-S. Lim, Y.-K. Tzeng, C.-Y. Fang, C.-C. Han, H.-C. Chang, and W. Fann, "Mass production and dynamic imaging of fluorescent nanodiamonds," *Nature Nanotechnology*, vol. 3, pp. 284 – 288, 2008. [Online]. Available: http://www.nature.com/nnano/journal/v3/n5/abs/nnano.2008.99.html

[29] D. A. Redman, S. Brown, R. H. Sands, and S. C. Rand, "Spin dynamics and electronic states of n-V centers in diamond by EPR and four-wave-mixing spectroscopy," *Phys. Rev. Lett.*, vol. 67, pp. 3420–3423, Dec 1991. [Online]. Available: http://link.aps.org/doi/10.1103/PhysRevLett.67.3420

[30] J. H. N. Loubser and J. A. van Wyk, "Electron spin resonance in the study of diamond," *Reports on Progress in Physics*, vol. 41, no. 8, p. 1201, 1978. [Online]. Available: http://stacks.iop.org/0034-4885/41/i=8/a=002

[31] V. M. Acosta, E. Bauch, M. P. Ledbetter, A. Waxman, L.-S. Bouchard, and D. Budker, "Temperature dependence of the nitrogen-vacancy magnetic resonance in diamond," *Phys. Rev. Lett.*, vol. 104, p. 070801, Feb 2010. [Online]. Available: http://link.aps.org/doi/10.1103/PhysRevLett.104.070801

[32] L. J. Rogers, R. L. McMurtrie, M. J. Sellars, and N. B. Manson, "Time-averaging within the excited state of the nitrogen-vacancy centre in diamond," *New Journal of Physics*, vol. 11, no. 6, p. 063007, 2009. [Online]. Available: http://stacks.iop.org/1367-2630/11/i=6/a=063007

[33] E. van Oort, B. van der Kamp, R. Sitter, and M. Glasbeek, "Microwave-induced line-narrowing of the n-v defect absorption in diamond," *Journal of Luminescence*, vol. 48–49, Part 2, no. 0, pp. 803–806, 1991. [Online]. Available: http://www.sciencedirect.com/science/article/pii/002223139190245Q

[34] G. D. Fuchs, V. V. Dobrovitski, R. Hanson, A. Batra, C. D. Weis, T. Schenkel, and D. D. Awschalom, "Excited-state spectroscopy using single spin manipulation in diamond," *Phys. Rev. Lett.*, vol. 101, p. 117601, Sep 2008. [Online]. Available: http://link.aps.org/doi/10.1103/PhysRevLett.101.117601

[35] P. Neumann, R. Kolesov, V. Jacques, J. Beck, J. Tisler, A. Batalov, L. Rogers, N. B. Manson, G. Balasubramanian, F. Jelezko, and J. Wrachtrup, "Excited-state spectroscopy of single nv defects in diamond using optically detected magnetic resonance," *New Journal of Physics*, vol. 11, no. 1, p. 013017, 2009. [Online]. Available: http://stacks.iop.org/1367-2630/11/i=1/a=013017

[36] T. v. d. S. Lucio Robledo, Hannes Bernien and R. Hanson, "Spin dynamics in the optical cycle of single nitrogen-vacancy centres in diamond," *New Journal of Physics*, vol. 13, p. 025013, 2011.

[37] D. Le Sage, D. R. Arai, K.and Glenn, L. M. DeVience, S. J.and Pham, L. Rahn-Lee, M. D. Lukin, A. Yacoby, K. A., and R. L. Walsworth, "Optical magnetic imaging of living cells," *Nature*, vol. 496, pp. 486–489, 2013. [Online]. Available: http://www.nature.com/nature/journal/v496/n7446/full/nature12072.html

[38] M. Chipaux, A. Tallaire, J. Achard, S. Pezzagna, J. Meijer, V. Jacques, J.-F. Roch, and T. Debuisschert, "Magnetic imaging with an ensemble of nitrogen vacancy centers in diamond," *arXiv:1410.0178v1*, 2014. [Online]. Available: http://arxiv.org/abs/1410.0178

[39] P. Maletinsky, S. Hong, M. S. Grinolds, B. Hausmann, M. D. Lukin, R. L. Walsworth, and M. L. A. Yacoby, "A robust scanning diamond sensor for nanoscale imaging with single nitrogen-vacancy centres," *Nature Nanotechnolog*, vol. 7, pp. 320–324, 13 March 2012. [Online]. Available: http://www.nature.com/nnano/journal/v7/n5/full/nnano.2012.50.html

[40] C. P. Slichter, *Principles of Magnetic Resonance*. Springer, 3rd edition enlarged and updated, 1996.

[41] D. P. DiVincenzo, "The physical implementation of quantum computation," *Fortschritte der Physik*, vol. 48, no. 9-11, pp. 771–783, 2000. [Online]. Available: http://dx.doi.org/10.1002/1521-3978(200009)48:9/11<771::AID-PROP771>3.0.CO;2-E

[42] N. Mizuochi, P. Neumann, F. Rempp, J. Beck, V. Jacques, P. Siyushev, K. Nakamura, D. J. Twitchen, H. Watanabe, S. Yamasaki, F. Jelezko, and J. Wrachtrup, "Coherence of single spins coupled to a nuclear spin bath of varying density," *Phys. Rev. B*, vol. 80, p. 041201, Jul 2009. [Online]. Available: http://link.aps.org/doi/10.1103/PhysRevB.80.041201

[43] R. Hanson, O. Gywat, and D. D. Awschalom, "Room-temperature manipulation and decoherence of a single spin in diamond," *Phys. Rev. B*, vol. 74, p. 161203, Oct 2006. [Online]. Available: http://link.aps.org/doi/10.1103/PhysRevB.74.161203

[44] F. P. Bundy, H. T. Hall, H. M. Strong, and R. H. Wentorf, "Man-made diamond," *Nature*, vol. 176, pp. 51–55, 1955.

[45] A. Tallaire, A. Collins, D. Charles, J. Achard, R. Sussmann, A. Gicquel, M. Newton, A. Edmonds, and R. Cruddace, "Characterisation of high-quality thick single-crystal diamond grown by CVD with a low nitrogen addition," *Diamond and Related Materials*, vol. 15, no. 10, pp. 1700 – 1707, 2006. [Online]. Available: http://www.sciencedirect.com/science/article/pii/S0925963506000823

[46] G. Balasubramanian, P. Neumann, D. Twitchen, M. Markham, R. Kolesov, N. Mizuochi, J. Isoya, J. Achard, J. Beck, J. Tissler, V. Jacques, P. R. Hem-

mer, F. Jelezko, and J. Wrachtrup, "Ultralong spin coherence time in isotopically engineered diamond," *Nature Materials*, no. 8, pp. 383–387, 2009.

[47] T. Ishikawa, K.-M. C. Fu, C. Santori, V. M. Acosta, R. G. Beausoleil, H. Watanabe, S. Shikata, and K. M. Itoh, "Optical and spin coherence properties of nitrogen-vacancy centers placed in a 100 nm thick isotopically purified diamond layer," *Nano Letters*, vol. 12, no. 4, pp. 2083–2087, 2012, pMID: 22404419. [Online]. Available: http://dx.doi.org/10.1021/nl300350r

[48] L. Viola, E. Knill, and S. Lloyd, "Dynamical decoupling of open quantum systems," *Phys. Rev. Lett.*, vol. 82, pp. 2417–2421, Mar 1999. [Online]. Available: http://link.aps.org/doi/10.1103/PhysRevLett.82.2417

[49] C. A. Ryan, J. S. Hodges, and D. G. Cory, "Robust decoupling techniques to extend quantum coherence in diamond," *Phys. Rev. Lett.*, vol. 105, p. 200402, Nov 2010. [Online]. Available: http://link.aps.org/doi/10.1103/PhysRevLett.105.200402

[50] F. Jelezko, T. Gaebel, I. Popa, A. Gruber, and J. Wrachtrup, "Observation of coherent oscillations in a single electron spin," *Phys. Rev. Lett.*, vol. 92, p. 076401, 2004.

[51] M. V. Gurudev Dutt, L. Childress, L. Jiang, E. Togan, J. Maze, F. Jelezko, A. S. Zibrov, P. R. Hemmer, and M. D. Lukin, "Quantum register based on individual electronic and nuclear spin qubits in diamond," *Science*, vol. 316, pp. 1312–1314, 2007.

[52] P. Neumann, N. Mizuochi, F. Rempp, P. Hemmer, H. Watanabe, S. Yamasaki, V. Jacques, T. Gaebel, F. Jelezko, and J. Wrachtrup, "Multipartite entanglement among single spins in diamond," *Science*, vol. 320, pp. 1326–1329, 2008.

[53] J. Meijer, B. Burchard, M. Domhan, C. Wittmann, T. Gaebel, I. Popa, F. Jelezko, and J. Wrachtrup, "Generation of single color centers by focused nitrogen implantation," *Applied Physics Letters*, vol. 87, no. 26, pp. –, 2005. [Online]. Available: http://scitation.aip.org/content/aip/journal/apl/87/26/10.1063/1.2103389

[54] B. K. Ofori-Okai, S. Pezzagna, K. Chang, M. Loretz, R. Schirhagl, Y. Tao, B. A. Moores, K. Groot-Berning, J. Meijer, and C. L. Degen, "Spin properties of very shallow nitrogen vacancy defects in diamond," *Phys. Rev. B*, vol. 86, p. 081406, Aug 2012. [Online]. Available: http://link.aps.org/doi/10.1103/PhysRevB.86.081406

[55] J. M. M. Loretz, S. Pezzagna and C. L. Degen, "Nanoscale nuclear magnetic resonance with a 1.9-nm-deep nitrogen-vacancy sensor," *Applied Physics Letters*, vol. 104, no. 033102, 2014.

[56] S. Pezzagna, B. Naydenov, F. Jelezko, J. Wrachtrup, and J. Meijer, "Creation efficiency of nitrogen-vacancy centres in diamond," *New Journal of Physics*, vol. 12, no. 6, p. 065017, 2010. [Online]. Available: http://stacks.iop.org/1367-2630/12/i=6/a=065017

[57] L. Rondin, G. Dantelle, A. Slablab, F. Grosshans, F. Treussart, P. Bergonzo, S. Perruchas, T. Gacoin, M. Chaigneau, H.-C. Chang, V. Jacques, and J.-F. Roch, "Surface-induced charge state conversion of nitrogen-vacancy defects in nanodiamonds," *Phys. Rev. B*, vol. 82, p. 115449, Sep 2010. [Online]. Available: http://link.aps.org/doi/10.1103/PhysRevB.82.115449

[58] C. Santori, P. E. Barclay, K.-M. C. Fu, and R. G. Beausoleil, "Vertical distribution of nitrogen-vacancy centers in diamond formed by ion implantation and annealing," *Phys. Rev. B*, vol. 79, p. 125313, Mar 2009. [Online]. Available: http://link.aps.org/doi/10.1103/PhysRevB.79.125313

[59] K.-M. C. Fu, C. Santori, P. E. Barclay, and R. G. Beausoleil, "Conversion of neutral nitrogen-vacancy centers to negatively charged nitrogen-vacancy centers through selective oxidation," *Applied Physics Letters*, vol. 96, no. 12, pp. –, 2010. [Online]. Available: http://scitation.aip.org/content/aip/journal/apl/96/12/10.1063/1.3364135

[60] H. Kato, M. Wolfer, C. Schreyvogel, M. Kunzer, W. Muller-Sebert, H. Obloh, S. Yamasaki, and C. Nebel, "Tunable light emission from nitrogen-vacancy centers in single crystal diamond pin diodes," *Applied Physics Letters*, vol. 102, no. 15, pp. 151 101–151 101–4, Apr 2013.

[61] P. Spinicelli, A. Dreau, L. Rondin, F. Silva, J. Achard, S. Xavier, S. Bansropun, T. Debuisschert, S. Pezzagna, J. Achard, J. Meijer, V. Jacques, and J.-F. Roch, "Engineered arrays of nitrogen-vacancy color centers in diamond based on implantation of CN-molecules through nanoapertures," *New Journal of Physics*, vol. 13, no. 2, p. 025014, 2011. [Online]. Available: http://stacks.iop.org/1367-2630/13/i=2/a=025014

[62] S. Pezzagna, D. Wildanger, P. Mazarov, A. D. Wieck, Y. Sarov, I. Rangelow, B. Naydenov, F. Jelezko, S. W. Hell, and J. Meijer, "Nanoscale engineering and optical addressing of single spins in diamond," *Small*, vol. 6, no. 19, pp. 2117–2121, 2010. [Online]. Available: http://dx.doi.org/10.1002/smll.201000902

[63] S. Pezzagna, D. Rogalla, H.-W. Becker, I. Jakobi, F. Dolde, B. Naydenov, J. Wrachtrup, F. Jelezko, C. Trautmann, and J. Meijer, "Creation of colour centres in diamond by collimated ion-implantation through nano-channels in mica," *physica status solidi (a)*, vol. 208, no. 9, pp. 2017–2022, 2011. [Online]. Available: http://dx.doi.org/10.1002/pssa.201100455

[64] W. Chen and H. Ahmed, "Fabrication of 5–7 nm wide etched lines in silicon using 100 kev electron–beam lithography and polymethylmethacrylate resist," *Applied Physics Letters*, 1993.

[65] D. M. Toyli, C. D. Weis, G. D. Fuchs, T. Schenkel, and D. D. Awschalom, "Chip-scale nanofabrication of single spins and spin arrays in diamond," *Nano Lett.*, vol. 10, pp. 3168–3172, 2010.

[66] S. Pezzagna, D. Rogalla, D. Wildanger, J. Meijer, and A. Zaitsev, "Creation and nature of optical centres in diamond for single-photon emission–overview and critical remarks," *New J. Phys.*, vol. 13, no. 035024, 29 March 2011. [Online]. Available: http://iopscience.iop.org/1367-2630/13/3/035024/fulltext/

[67] K. Beha, H. Fedder, M. Wolfer, M. C. Becker, P. Siyushev, M. Jamali, A. Batalov, C. Hinz, J. Hees, L. Kirste, H. Obloh, E. Gheeraert, B. Naydenov, I. Jakobi, F. Dolde, S. Pezzagna, D. Twittchen, M. Markham, D. Dregely, H. Giessen, J. Meijer, F. Jelezko, C. E. Nebel, R. Bratschitsch, A. Leitenstorfer, and J. Wrachtrup, "Diamond nanophotonics," *Diamond nanophotonics*, vol. 3, pp. 895–908, 21 December 2012. [Online]. Available: http://www.beilstein-journals.org/bjnano/single/articleFullText.htm?publicId=2190-4286-3-100

[68] T. Yamamoto, T. Umeda, K. Watanabe, S. Onoda, M. L. Markham, D. J. Twitchen, B. Naydenov, L. P. McGuinness, T. Teraji, S. Koizumi, F. Dolde, H. Fedder, J. Honert, J. Wrachtrup, T. Ohshima, F. Jelezko, and J. Isoya, "Extending spin coherence times of diamond qubits by high-temperature annealing," *Phys. Rev. B*, vol. 88, p. 075206, Aug 2013. [Online]. Available: http://link.aps.org/doi/10.1103/PhysRevB.88.075206

[69] T. Staudacher, F. Ziem, L. Haussler, R. Stohr, S. Steinert, F. Reinhard, J. Scharpf, A. Denisenko, and J. Wrachtrup, "Enhancing the spin properties of shallow implanted nitrogen vacancy centers in diamond by epitaxial overgrowth," *Applied Physics Letters*, vol. 101, no. 21, pp. 212 401–212 401–4, Nov 2012.

[70] F. Dolde, H. Fedder, M. W. Doherty, T. Nöbauer, F. Rempp, G. Balasubramanian, T. Wolf, F. Reinhard, L. C. L. Hollenberg, F. Jelezko, and J. Wrachtrup, "Electric-field sensing using single diamond spins," *Nature Physics*, vol. 7, no. -, pp. 459–463, 2011. [Online]. Available: http://www.nature.com/nphys/journal/v7/n6/full/nphys1969.html

[71] R. Schirhagl, K. Chang, M. Loretz, and C. L. Degen, "Nitrogen-vacancy centers in diamond: Nanoscale sensors for physics and biology," *Annual Review of Physical Chemistry*, vol. 65, no. 1, pp. 83–105, 2014, pMID: 24274702. [Online]. Available: http://dx.doi.org/10.1146/annurev-physchem-040513-103659

[72] L. Rondin, J.-P. Tetienne, T. Hingant, J.-F. Roch, P. Maletinsky, and V. Jacques, "Cheminform abstract: Magnetometry with nitrogen-vacancy defects in diamond," *ChemInform*, vol. 45, no. 42, p. no, 2014. [Online]. Available: http://dx.doi.org/10.1002/chin.201442289

[73] ——, "Magnetometry with nitrogen-vacancy defects in diamond," *Reports on Progress in Physics*, vol. 77, no. 5, p. 056503, 2014. [Online]. Available: http://stacks.iop.org/0034-4885/77/i=5/a=056503

[74] K. Ohno, F. Joseph Heremans, L. C. Bassett, B. A. Myers, D. M. Toyli, A. C. Bleszynski Jayich, C. J. Palmstrom, and D. D. Awschalom, "Engineering shallow spins in diamond with nitrogen delta-doping," *Applied Physics Letters*, vol. 101, no. 8, pp. –, 2012. [Online]. Available: http://scitation.aip.org/content/aip/journal/apl/101/8/10.1063/1.4748280

[75] K. Ohashi, T. Rosskopf, H. Watanabe, M. Loretz, Y. Tao, R. Hauert, S. Tomizawa, T. Ishikawa, J. Ishi-Hayase, S. Shikata, C. L. Degen, and K. M. Itoh, "Negatively charged nitrogen-vacancy centers in a 5 nm thin ^{12}C diamond film," *Nano Letters*, vol. 13, no. 10, pp. 4733–4738, 2013, pMID: 24020334. [Online]. Available: http://dx.doi.org/10.1021/nl402286v

[76] T. Teraji and T. Ito, "Homoepitaxial diamond growth by high-power microwave-plasma chemical vapor deposition," *Journal of Crystal Growth*, vol. 271, no. 3–4, pp. 409 – 419, 2004. [Online]. Available: http://www.sciencedirect.com/science/article/pii/S0022024804009327

[77] J. Achard, F. Silva, A. Tallaire, X. Bonnin, G. Lombardi, K. Hassouni, and A. Gicquel, "High quality mpacvd diamond single crystal growth: high microwave power density regime," *Journal of Physics D: Applied Physics*, vol. 40, no. 20, p. 6175, 2007. [Online]. Available: http://stacks.iop.org/0022-3727/40/i=20/a=S04

[78] A. M. Edmonds, U. F. S. D'Haenens-Johansson, R. J. Cruddace, M. E. Newton, K.-M. C. Fu, C. Santori, R. G. Beausoleil, D. J. Twitchen, and M. L. Markham, "Production of oriented nitrogen-vacancy color centers in synthetic diamond," *Phys. Rev. B*, vol. 86, p. 035201, Jul 2012. [Online]. Available: http://link.aps.org/doi/10.1103/PhysRevB.86.035201

[79] L. M. Pham, N. Bar-Gill, D. Le Sage, C. Belthangady, A. Stacey, M. Markham, D. J. Twitchen, M. D. Lukin, and R. L. Walsworth, "Enhanced metrology using preferential orientation of nitrogen-vacancy centers in diamond," *Phys. Rev. B*, vol. 86, p. 121202, Sep 2012. [Online]. Available: http://link.aps.org/doi/10.1103/PhysRevB.86.121202

[80] F. De Martini, G. Di Giuseppe, and M. Marrocco, "Single-mode generation of quantum photon states by excited single molecules in a microcavity

trap," *Phys. Rev. Lett.*, vol. 76, pp. 900–903, Feb 1996. [Online]. Available: http://link.aps.org/doi/10.1103/PhysRevLett.76.900

[81] R. Hanbury Brown and R. Q. Twiss, "Correlation between photons in two coherent beams of light," *Nature*, vol. 177, pp. 27–29, 1956. [Online]. Available: http://dx.doi.org/10.1038/177027a0

[82] A. Beveratos, "R ?ealisation exp ?erimentale d'une source de photons uniques par fluorescence de centres color ?es individuels dans le diamant: application à la cryptographie quantique," Ph.D. dissertation, L'UNIVERSITÈ PARIS XI ORSAY, 2002.

[83] R. J. Epstein, F. M. Mendoza, Y. K. Kato, and D. D. Awschalom, "Anisotropic interactions of a single spin and dark-spin spectroscopy in diamond," *Nat Phys*, vol. 1, no. 1745-2473, pp. 94–98, 2005. [Online]. Available: http://dx.doi.org/10.1038/nphys141

[84] E. Rittweger, D. Wildanger, and S. W. Hell, "Far-field fluorescence nanoscopy of diamond color centers by ground state depletion," *EPL (Europhysics Letters)*, vol. 86, no. 1, p. 14001, 2009. [Online]. Available: http://stacks.iop.org/0295-5075/86/i=1/a=14001

[85] S. Bretschneider, C. Eggeling, and S. W. Hell, "Breaking the diffraction barrier in fluorescence microscopy by optical shelving," *Phys. Rev. Lett.*, vol. 98, p. 218103, May 2007. [Online]. Available: http://link.aps.org/doi/10.1103/PhysRevLett.98.218103

[86] J. R. Rabeau, P. Reichart, G. Tamanyan, D. N. Jamieson, S. Prawer, F. Jelezko, T. Gaebel, I. Popa, M. Domhan, and J. Wrachtrup, "Implantation of labelled single nitrogen vacancy centers in diamond using ^{15}N," *Applied Physics Letters*, vol. 88, no. 2, pp. –, 2006. [Online]. Available: http://scitation.aip.org/content/aip/journal/apl/88/2/10.1063/1.2158700

[87] J. Meijer, S. Pezzagna, T. Vogel, B. Burchard, H. Bukow, I. Rangelow, Y. Sarov, H. Wiggers, I. Plumel, F. Jelezko, J. Wrachtrup, F. Schmidt-Kaler, W. Schnitzler, and K. Singer, "Towards the implanting of ions and positioning of nanoparticles with nm spatial resolution," *Applied Physics A*, vol. 91, no. 4, pp. 567–571, 2008. [Online]. Available: http://dx.doi.org/10.1007/s00339-008-4515-1

[88] J. Ziegler, *The stopping range of ions in matter, SRIM-2008*, online at http://srim.org Std., 2008.

[89] C. Bradac, T. Gaebel, N. Naidoo, M. Sellars, J. Twamley, L. Brown, A. Barnard, T. Platkhotnik, A. Zvyagin, and J. Rabeau, "Observation and control of blinking nitrogen-vacancy centres in discrete nanodiamonds,"

Nature Nanotechnology, vol. 5, pp. 345–349, 2010. [Online]. Available: http://www.nature.com/nnano/journal/v5/n5/pdf/nnano.2010.56.pdf

[90] Y. Doi, T. Makino, H. Kato, D. Takeuchi, M. Ogura, H. Okushi, H. Morishita, T. Tashima, S. Miwa, S. Yamasaki, P. Neumann, J. Wrachtrup, Y. Suzuki, and N. Mizuochi, "Deterministic electrical charge-state initialization of single nitrogen-vacancy center in diamond," *Phys. Rev. X*, vol. 4, p. 011057, Mar 2014. [Online]. Available: http://link.aps.org/doi/10.1103/PhysRevX.4.011057

[91] J. Isberg, J. Hammersberg, E. Johansson, T. Wikstrom, D. J. Twitchen, A. J. Whitehead, S. E. Coe, and G. A. Scarsbrook, "High carrier mobility in single-crystal plasma-deposited diamond," *Science*, vol. 297, no. 5587, pp. 1670–1672, 2002. [Online]. Available: http://www.sciencemag.org/content/297/5587/1670.abstract

[92] C. Schreyvogel, M. Wolfer, H. Kato, M. Schreck, and C. E. Nebel, "Tuned NV emission by in-plane Al-schottky junctions on hydrogen terminated diamond," *Scientific Reports*, vol. 4, no. 3634, 10 January 2014.

[93] F. Maier, J. Ristein, and L. Ley, "Electron affinity of plasma-hydrogenated and chemically oxidized diamond (100) surfaces," *Phys. Rev. B*, vol. 64, p. 165411, Oct 2001. [Online]. Available: http://link.aps.org/doi/10.1103/PhysRevB.64.165411

[94] V. Petrakova, A. Taylor, I. Kratochvilova, F. Fendrych, J. Vacik, J. Kucka, J. Stursa, P. Cigler, M. Ledvina, A. Fiserova, P. Kneppo, and M. Nesladek, "Luminescence of nanodiamond driven by atomic functionalization: Towards novel detection principles," *Advanced Functional Materials*, vol. 22, no. 4, pp. 812–819, 2012. [Online]. Available: http://dx.doi.org/10.1002/adfm.201101936

[95] N. Manson and J. Harrison, "Photo-ionization of the nitrogen-vacancy center in diamond," *Diamond and Related Materials*, vol. 14, no. 10, pp. 1705 – 1710, 2005. [Online]. Available: http://www.sciencedirect.com/science/article/pii/S0925963505002402

[96] A. Tallaire, J. Barjon, O. Brinza, J. Achard, F. Silva, V. Mille, R. Issaoui, A. Tardieu, and A. Gicquel, "Dislocations and impurities introduced from etch-pits at the epitaxial growth resumption of diamond," *Diamond and Related Materials*, vol. 20, no. 7, pp. 875 – 881, 2011. [Online]. Available: http://www.sciencedirect.com/science/article/pii/S0925963511001518

[97] R. Locher, C. Wild, N. Herres, D. Behr, and P. Koidl, "Nitrogen stabilized ⟨100⟩ texture in chemical vapor deposited diamond films," *Applied Physics Letters*, vol. 65, no. 1, pp. 34–36, 1994. [Online]. Available: http://scitation.aip.org/content/aip/journal/apl/65/1/10.1063/1.113064

[98] S. Jin and T. D. Moustakas, "Effect of nitrogen on the growth of diamond films," *Applied Physics Letters*, vol. 65, no. 4, pp. 403–405, 1994. [Online]. Available: http://scitation.aip.org/content/aip/journal/apl/65/4/10.1063/1.112315

[99] F. de Theije, J. Schermer, and W. van Enckevort, "Effects of nitrogen impurities on the {CVD} growth of diamond: step bunching in theory and experiment," *Diamond and Related Materials*, vol. 9, no. 8, pp. 1439 – 1449, 2000. [Online]. Available: http://www.sciencedirect.com/science/article/pii/S0925963500002612

[100] P. Martineau, M. Gaukroger, R. Khan, and D. Evans, "Effect of steps on dislocations in CVD diamond grown on {001} substrates," *physica status solidi (c)*, vol. 6, no. 8, pp. 1953–1957, 2009. [Online]. Available: http://dx.doi.org/10.1002/pssc.200881465

[101] T. Frauenheim, G. Jungnickel, P. Sitch, M. Kaukonen, F. Weich, J. Widany, and D. Porezag, "A molecular dynamics study of N-incorporation into carbon systems: Doping, diamond growth and nitride formation," *Diamond and Related Materials*, vol. 7, no. 2Ð5, pp. 348 – 355, 1998. [Online]. Available: http://www.sciencedirect.com/science/article/pii/S0925963597001866

[102] K. Hassouni, F. Silva, and A. Gicquel, "Modelling of diamond deposition microwave cavity generated plasmas," *Journal of Physics D: Applied Physics*, vol. 43, no. 15, p. 153001, 2010. [Online]. Available: http://stacks.iop.org/0022-3727/43/i=15/a=153001

[103] K. Ohno, F. Joseph Heremans, C. F. de las Casas, B. A. Myers, B. J. Aleman, A. C. Bleszynski Jayich, and D. D. Awschalom, "Three-dimensional localization of spins in diamond using ^{12}C implantation," *Applied Physics Letters*, vol. 105, no. 5, pp. –, 2014. [Online]. Available: http://scitation.aip.org/content/aip/journal/apl/105/5/10.1063/1.4890613

[104] J. Botsoa, T. Sauvage, M.-P. Adam, P. Desgardin, E. Leoni, B. Courtois, F. Treussart, and M.-F. Barthe, "Optimal conditions for NV^- center formation in type-1b diamond studied using photoluminescence and positron annihilation spectroscopies," *Phys. Rev. B*, vol. 84, p. 125209, Sep 2011. [Online]. Available: http://link.aps.org/doi/10.1103/PhysRevB.84.125209

[105] L. M. Pham, D. L. Sage, P. L. Stanwix, T. K. Yeung, D. Glenn, A. Trifonov, P. Cappellaro, P. R. Hemmer, M. D. Lukin, H. Park, A. Yacoby, and R. L. Walsworth, "Magnetic field imaging with nitrogen-vacancy ensembles," *New Journal of Physics*, vol. 13, no. 4, p. 045021, 2011. [Online]. Available: http://stacks.iop.org/1367-2630/13/i=4/a=045021

[106] L. Childress, M. V. Gurudev Dutt, J. M. Taylor, A. S. Zibrov, F. Jelezko, J. Wrachtrup, P. R. Hemmer, and M. D. Lukin, "Coherent

dynamics of coupled electron and nuclear spin qubits in diamond," *Science*, vol. 314, no. 5797, pp. 281–285, 2006. [Online]. Available: http://www.sciencemag.org/content/314/5797/281.abstract

[107] R. Samlenski, C. Haug, R. Brenn, C. Wild, R. Locher, and P. Koidl, "Incorporation of nitrogen in chemical vapor deposition diamond," *Applied Physics Letters*, vol. 67, no. 19, pp. 2798–2800, Nov 1995.

[108] N. B. Manson, J. P. Harrison, and M. J. Sellars, "Nitrogen-vacancy center in diamond: Model of the electronic structure and associated dynamics," *Phys. Rev. B*, vol. 74, p. 104303, Sep 2006. [Online]. Available: http://link.aps.org/doi/10.1103/PhysRevB.74.104303

[109] A. Dréau, J.-R. Maze, M. Lesik, J.-F. Roch, and V. Jacques, "High-resolution spectroscopy of single nv defects coupled with nearby ^{13}C nuclear spins in diamond," *Phys. Rev. B*, vol. 85, p. 134107, Apr 2012. [Online]. Available: http://link.aps.org/doi/10.1103/PhysRevB.85.134107

[110] T. P. M. Alegre, C. Santori, G. Medeiros-Ribeiro, and R. G. Beausoleil, "Polarization-selective excitation of nitrogen vacancy centers in diamond," *Phys. Rev. B*, vol. 76, p. 165205, Oct 2007. [Online]. Available: http://link.aps.org/doi/10.1103/PhysRevB.76.165205

[111] C. Battaile, D. Srolovitz, and J. Butler, "Morphologies of diamond films from atomic-scale simulations of chemical vapor deposition," *Diamond and Related Materials*, vol. 6, no. 9, pp. 1198 – 1206, 1997. [Online]. Available: http://www.sciencedirect.com/science/article/pii/S0925963597000460

[112] ——, "Atomic-scale simulations of chemical vapor deposition on flat and vicinal diamond substrates," *Journal of Crystal Growth*, vol. 194, no. 3–4, pp. 353–368, 1998. [Online]. Available: http://www.sciencedirect.com/science/article/pii/S002202489800685X

[113] M. K. Atumi, J. P. Goss, P. R. Briddon, and M. J. Rayson, "Atomistic modeling of the polarization of nitrogen centers in diamond due to growth surface orientation," *Phys. Rev. B*, vol. 88, p. 245301, Dec 2013. [Online]. Available: http://link.aps.org/doi/10.1103/PhysRevB.88.245301

[114] J. Michl, T. Teraji, S. Zaiser, I. Jakobi, G. Waldherr, F. Dolde, P. Neumann, M. W. Doherty, N. B. Manson, J. Isoya, and J. Wrachtrup, "Perfect alignment and preferential orientation of nitrogen-vacancy centers during chemical vapor deposition diamond growth on (111) surfaces," *Applied Physics Letters*, vol. 104, no. 10, pp. –, 2014. [Online]. Available: http://scitation.aip.org/content/aip/journal/apl/104/10/10.1063/1.4868128

[115] T. Fukui, Y. Doi, T. Miyazaki, Y. Miyamoto, H. Kato, T. Matsumoto, T. Makino, S. Yamasaki, R. Morimoto, N. Tokuda, M. Hatano, Y. Sakagawa, H. Morishita, T. Tashima, S. Miwa, Y. Suzuki, and N. Mizuochi, "Perfect selective alignment of nitrogen-vacancy centers in diamond," *Applied Physics Express*, vol. 7, no. 5, p. 055201, 2014. [Online]. Available: http://stacks.iop.org/1882-0786/7/i=5/a=055201

[116] R. Farrer, "On the substitutional nitrogen donor in diamond," *Solid State Communications*, vol. 7, no. 9, pp. 685 – 688, 1969. [Online]. Available: http://www.sciencedirect.com/science/article/pii/0038109869905936

[117] F. Kaiser, V. Jacques, A. Batalov, F. Siyushev, P.and Jelezko, and J. Wrachtrup, "Polarization properties of single photons emitted by nitrogen-vacancy defect in diamond at low temperature," *arXiv:0906.3426v1*, 2009. [Online]. Available: http://arxiv.org/abs/0906.3426

[118] S. Steinert, F. Dolde, P. Neumann, A. Aird, B. Naydenov, G. Balasubramanian, F. Jelezko, and J. Wrachtrup, "High sensitivity magnetic imaging using an array of spins in diamond," *Review of Scientific Instruments*, vol. 81, no. 4, pp. –, 2010. [Online]. Available: http://scitation.aip.org/content/aip/journal/rsi/81/4/10.1063/1.3385689

[119] V. M. Acosta, E. Bauch, M. P. Ledbetter, C. Santori, K.-M. C. Fu, P. E. Barclay, R. G. Beausoleil, H. Linget, J. F. Roch, F. Treussart, S. Chemerisov, W. Gawlik, and D. Budker, "Diamonds with a high density of nitrogen-vacancy centers for magnetometry applications," *Phys. Rev. B*, vol. 80, p. 115202, Sep 2009. [Online]. Available: http://link.aps.org/doi/10.1103/PhysRevB.80.115202

[120] Y. Dumeige, M. Chipaux, V. Jacques, F. Treussart, J.-F. Roch, T. Debuisschert, V. M. Acosta, A. Jarmola, K. Jensen, P. Kehayias, and D. Budker, "Magnetometry with nitrogen-vacancy ensembles in diamond based on infrared absorption in a doubly resonant optical cavity," *Phys. Rev. B*, vol. 87, p. 155202, Apr 2013. [Online]. Available: http://link.aps.org/doi/10.1103/PhysRevB.87.155202

[121] L. M. Pham, N. Bar-Gill, C. Belthangady, D. Le Sage, P. Cappellaro, M. D. Lukin, A. Yacoby, and R. L. Walsworth, "Enhanced solid-state multispin metrology using dynamical decoupling," *Phys. Rev. B*, vol. 86, p. 045214, Jul 2012. [Online]. Available: http://link.aps.org/doi/10.1103/PhysRevB.86.045214

[122] Y. Kubo, C. Grezes, A. Dewes, T. Umeda, J. Isoya, H. Sumiya, N. Morishita, H. Abe, S. Onoda, T. Ohshima, V. Jacques, A. Dréau, J.-F. Roch, I. Diniz, A. Auffeves, D. Vion, D. Esteve, and P. Bertet, "Hybrid quantum circuit with a superconducting qubit coupled to a spin

ensemble," *Phys. Rev. Lett.*, vol. 107, p. 220501, Nov 2011. [Online]. Available: http://link.aps.org/doi/10.1103/PhysRevLett.107.220501

[123] X. Zhu, S. Saito, A. Kemp, K. Kakuyanagi, S. Karimoto, H. Nakano, W. J. Munro, Y. Tokura, M. S. Everitt, K. Nemoto, M. Kasu, N. Mizuochi, and K. Semba, "Coherent coupling of a superconducting flux qubit to an electron spin ensemble in diamond," *Nature*, vol. 478, pp. 221–224, 2011. [Online]. Available: http://www.nature.com/nature/journal/v478/n7368/full/nature10462.html

[124] A. Faraon, P. E. Barclay, C. Santori, K.-M. C. Fu, and R. G. Beausoleil, "Resonant enhancement of the zero-phonon emission from a colour centre in a diamond cavity," *Nature Photonics*, vol. 5, pp. 301–305, 2011. [Online]. Available: http://www.nature.com/nphoton/journal/v5/n5/full/nphoton.2011.52.html

[125] E. Neu, P. Appel, M. Ganzhorn, J. Miguel-Sanchez, M. Lesik, V. Mille, V. Jacques, A. Tallaire, J. Achard, and P. Maletinsky, "Photonic nano-structures on (111)-oriented diamond," *Applied Physics Letters*, vol. 104, no. 15, pp. –, 2014. [Online]. Available: http://scitation.aip.org/content/aip/journal/apl/104/15/10.1063/1.4871580

[126] W. F. Koehl, B. B. Buckley, F. J. Heremans, G. Calusine, and D. D. Awschalom, "Room temperature coherent control of defect spin qubits in silicon carbide," *Nature*, vol. 479, pp. 84–87, 2011.

[127] N. Zhao, S.-W. Ho, and R.-B. Liu, "Decoherence and dynamical decoupling control of nitrogen vacancy center electron spins in nuclear spin baths," *Phys. Rev. B*, vol. 85, p. 115303, Mar 2012. [Online]. Available: http://link.aps.org/doi/10.1103/PhysRevB.85.115303

[128] E. L. Hahn, "Spin echoes," *Phys. Rev.*, vol. 80, pp. 580–594, Nov 1950. [Online]. Available: http://link.aps.org/doi/10.1103/PhysRev.80.580

[129] S. Meiboom and D. Gill, "Modified spin–echo method for measuring nuclear relaxation times," *Review of Scientific Instruments*, vol. 29, no. 8, pp. 688–691, 1958. [Online]. Available: http://scitation.aip.org/content/aip/journal/rsi/29/8/10.1063/1.1716296

[130] G. de Lange, Z. H. Wang, D. Ristè, V. V. Dobrovitski, and R. Hanson, "Universal dynamical decoupling of a single solid-state spin from a spin bath," *Science*, vol. 330, no. 6000, pp. 60–63, 2010. [Online]. Available: http://www.sciencemag.org/content/330/6000/60.abstract

[131] A. Laraoui, J. Hodges, and C. Meriles, "Nitrogen-vacancy-assisted magnetometry of paramagnetic centers in an individual diamond nanocrystal," *Nano Lett.*, vol. 12, no. 7, pp. 3477–3482, Jun 28. 2012.

[132] X.-F. He, N. B. Manson, and P. T. H. Fisk, "Paramagnetic resonance of photoexcited n- V defects in diamond. ii. hyperfine interaction with the ^{14}N nucleus," *Phys. Rev. B*, vol. 47, pp. 8816–8822, Apr 1993. [Online]. Available: http://link.aps.org/doi/10.1103/PhysRevB.47.8816

[133] S. Felton, A. M. Edmonds, M. E. Newton, P. M. Martineau, D. Fisher, D. J. Twitchen, and J. M. Baker, "Hyperfine interaction in the ground state of the negatively charged nitrogen vacancy center in diamond," *Phys. Rev. B*, vol. 79, p. 075203, Feb 2009. [Online]. Available: http://link.aps.org/doi/10.1103/PhysRevB.79.075203

[134] B. Smeltzer, J. McIntyre, and L. Childress, "Robust control of individual nuclear spins in diamond," *Phys. Rev. A*, vol. 80, p. 050302, Nov 2009. [Online]. Available: http://link.aps.org/doi/10.1103/PhysRevA.80.050302

[135] B. Smeltzer, L. Childress, and A. Gali, "13 c hyperfine interactions in the nitrogen-vacancy centre in diamond," *New Journal of Physics*, vol. 13, no. 2, p. 025021, 2011. [Online]. Available: http://stacks.iop.org/1367-2630/13/i=2/a=025021

[136] A. Dréau, M. Lesik, L. Rondin, P. Spinicelli, O. Arcizet, J.-F. Roch, and V. Jacques, "Avoiding power broadening in optically detected magnetic resonance of single nv defects for enhanced dc magnetic field sensitivity," *Phys. Rev. B*, vol. 84, p. 195204, Nov 2011. [Online]. Available: http://link.aps.org/doi/10.1103/PhysRevB.84.195204

[137] R. Brouri, A. Beveratos, J.-P. Poizat, and P. Grangier, "Photon antibunching in the fluorescence of individual color centers in diamond," *Optics Letters*, vol. 25, no. 17, pp. 1294–1296, 2000.

[138] K. Han, D. Wildanger, E. Rittweger, J. Meijer, S. Pezzagna, S. Hell, and C. Eggeling, "Dark state photophysics of nitrogen–vacancy centres in diamond," *New Journal of Physics*, vol. 14, no. 12, p. 123002, 2012.

[139] D. Zheng, "Study and manipulation of photoluminescent NV color center in diamond," Ph.D. dissertation, Ecole Normal Superieure de Cachan and East China Normal University, 2010. [Online]. Available: https://tel.archives-ouvertes.fr/tel-00595302/document

[140] P. R. Dolan, X. Li, J. Storteboom, and M. Gu, "Complete determination of the orientation of NV centers with radially polarized beams," *Opt. Express*, vol. 22, no. 4, pp. 4379–4387, Feb 2014. [Online]. Available: http://www.opticsexpress.org/abstract.cfm?URI=oe-22-4-4379

[141] R. C. Burns, A. I. Chumakov, S. H. Connell, D. Dube, H. P. Godfried, J. O. Hansen, J. Hartwig, J. Hoszowska, F. Masiello, L. Mkhonza, M. Rebak, A. Rommevaux, R. Setshedi, and P. Van Vaerenbergh, "Hpht growth and x-ray characterization of high-quality type iia diamond," *Journal of Physics: Condensed Matter*, vol. 21, no. 36, p. 364224, 2009. [Online]. Available: http://stacks.iop.org/0953-8984/21/i=36/a=364224

[142] J. E. Butler and I. Oleynik, "A mechanism for crystal twinning in the growth of diamond by chemical vapour deposition," *Philosophical Transactions of the Royal Society of London A: Mathematical, Physical and Engineering Sciences*, vol. 366, no. 1863, pp. 295–311, 2008.

[143] D. Shechtman, "Twin-determined growth of diamond films," *Materials Science and Engineering: A*, vol. 184, no. 2, pp. 113 – 118, 1994. [Online]. Available: http://www.sciencedirect.com/science/article/pii/0921509394910251

[144] A. Tallaire, J. Achard, A. Boussadi, O. Brinza, A. Gicquel, I. Kupriyanov, Y. Palyanov, G. Sakr, and J. Barjon, "High quality thick {CVD} diamond films homoepitaxially grown on (111)-oriented substrates," *Diamond and Related Materials*, vol. 41, no. 0, pp. 34 – 40, 2014. [Online]. Available: http://www.sciencedirect.com/science/article/pii/S0925963513002124

Publications

1. A. Dréau, **M. Lesik**, L. Rondin, P. Spinicelli, O. Arcizet, J.-F. Roch, and V. Jacques, "Avoiding power broadening in optically detected magnetic resonance of single NV defects for enhanced dc magnetic field sensitivity," Phys. Rev. B, vol. 84, p. 195204, (2011).

2. A. Dréau, J.-R. Maze, **M. Lesik**, J.-F. Roch, and V. Jacques, "High-resolution spectroscopy of single nv defects coupled with nearby ^{13}C nuclear spins in diamond," Phys. Rev. B, vol. 85, p. 134107, (2012).

3. **M. Lesik**, P. Spinicelli, S. Pezzagna, P. Happel, V. Jacques, O. Salord, B. Rasser, A. Delobbe, P. Sudraud, A. Tallaire, J. Meijer, and J.-F. Roch, "Maskless and targeted creation of arrays of colour centres in diamond using focused ion beam technology," physica status solidi (a), vol. 210, no. 10, pp. 2055–2059, (2013). [cf. §2]

4. **M. Lesik**, J.-P. Tetienne, A. Tallaire, J. Achard, V. Mille, A. Gicquel, J.-F. Roch, and V. Jacques, "Perfect preferential orientation of nitrogen-vacancy defects in a synthetic diamond sample," Applied Physics Letters, vol. 104, no. 11, pp. –, (2014). [cf. §5]

5. K. Groot-Berning, N. Raatz, I. Dobrinets, **M. Lesik**, P. Spinicelli, A. Tallaire, J. Achard, V. Jacques, J.-F. Roch, A. M. Zaitsev, J. Meijer, and S. Pezzagna, "Passive charge state control of nitrogen-vacancy centres in diamond using phosphorous and boron doping," physica status solidi (a), vol. 211, no. 10, pp. 2268–2273, (2014).

6. E. Neu, P. Appel, M. Ganzhorn, J. Miguel-Sanchez, **M. Lesik**, V. Mille, V. Jacques, A. Tallaire, J. Achard, and P. Maletinsky, "Photonic nano-structures on (111)-oriented diamond," Applied Physics Letters, vol. 104, no. 15, pp. –, (2014).

7. A. Tallaire, **M. Lesik**, V. Jacques, S. Pezzagna, V. Mille, O. Brinza, J. Meijer, B. Abel, J. Roch, A. Gicquel, and J. Achard, "Temperature dependent cre- ation of nitrogen-vacancy centers in single crystal {CVD} diamond layers," Diamond and Related Materials, vol. 51, no. 0, pp. 55 – 60, (2015). [cf. §4]

Abstract

The Nitrogen-Vacancy (NV) color center is a defect of diamond which behaves as an artificial atom hosted in a solid-state matrix. Due to its electron spin properties which can be read-out and manipulated as an elementary quantum system, the NV center has found a wide panel of applications as a qubit for quantum information and as a magnetic field sensor. However these applications require to control the properties of the NV centers and their localization. This doctoral thesis investigates methods allowing us to tailor the properties of NV centers by combining techniques for the implantation of nitrogen atoms and the plasma-assisted (CVD) synthesis of diamond.

The manuscript is divided into six chapters. The first chapter summarizes the properties of the NV center which will set our objectives for the NV engineering. The second chapter will describe how arrays of NV centers can be created using Focused Ion Beam implantation. The results open a wide range of applications for the targeted creation of NV centers in diamond structures such as photonic crystals and tips. However the low kinetic energy which is required for achieving implantation within a spot of 10-nm diameter leads to shallow defects which properties are strongly affected by the sample surface. The third chapter investigates how the overgrowth of a diamond layer over implanted NV centers can remove the detrimental influence of the surface. The fourth and fifth chapters describe effective methods for NV center fabrication through the control of the CVD growth conditions of the hosting crystal. Thin layers with high NV doping can be grown and almost perfect control of the orientation of the NV axis can be achieved. With the goal to optimize the spin coherence properties, the sixth chapter investigates how the electron spin of the NV center can be protected from decoherence effects induced by magnetic noise due to the unpolarized spins in the diamond lattice.

Résumé

Le centre coloré NV, constitué d'un atome d'azote et d'une lacune, est un défaut ponctuel du diamant qui se comporte comme un atome artificiel piégé dans cette matrice. Grâce aux propriétés de son spin électronique, qui peut être lu et manipulé comme un système quantique élémentaire, le centre NV as de nombreuses applications comme qubit pour l'information quantique ou comme sonde de champ magnétique. Cependant, ces applications nécessitent de contrôler les propriétés des centres NV ainsi que leur position dans le cristal. Cette thèse examine des méthodes pour atteindre ces objectifs en combinant des techniques d'implantation d'atomes et de croissance assistée par plasma (CVD) de diamant.

Le mémoire est divisé en six chapitres. Le premier chapitre résume les propriétés des centres NV, ce qui permet de définir les objectifs principaux dans la fabrication des centres NV. Le chapitre deux montre qu'il est possible de créer un réseau de centres NV par implantation au moyen d'une colonne d'ions focalisés. Cette technique est adaptée à la création de centres NV dans des nanostructures comme des cristaux photoniques ou des pointes de type AFM. Cependant la faible énergie cinétique des ions, nécessaire pour atteindre une résolution meilleure que 10 nm en diamètre de spot, conduit à une implantation proche de la surface ce qui affecte fortement les propriétés des centres NV. Le troisième chapitre examine comment la recroissance d'une couche de diamant sur des centres NV implantés permet de réduire l'impact négatif de la surface. Les quatrième et cinquième chapitres décrivent des méthodes pour la fabrication des centres NV en contrôlant les paramètres de la croissance CVD. Des couches minces fortement dopées avec les centres NV peuvent être créées, et un contrôle quasi parfait de l'orientation de l'axe du centre NV peut être obtenu. Dans l'objectif d'optimiser les propriétés du temps de cohérence du spin, le sixième chapitre étudie comment le spin électronique du centre NV peut être protégé contre les effets de décohérence induits par les spins non-polarisés dans la matrice du diamant.